MATEMATICKO-FYZIKÁLNÍ
FAKULTA
Univerzita Karlova

MASTER THESIS

Šárka Chlupová

Study of deposition of catalytic materials into fuel channels of micro-fuel cells on a chip

Department of the Surface and Plasma Science

Supervisor: Doc. Mgr. Iva Matolínová, Dr.

Study programme: Physics

Specialization: FPIP

Prague 2016

I would like to thank to my supervisor Doc. Iva Matolínová for supervising my diploma thesis and to all members of Department of Surface and Plasma Science for pleasant working environment. Many thanks belong to my colleague Mgr. Martin Dubau for all magnetron sputtering performed in my thesis and for all advices and support. At the end I would like to thank to my family for endless support and to my partner for everything.

I declare that I carried out this master thesis independently, and only with the cited sources, literature and other professional sources.

I understand that my work relates to the rights and obligations under the Act No. 121/2000 Coll., the Copyright Act, as amended, in particular the fact that the Charles University in Prague has the right to conclude a license agreement on the use of this work as a school work pursuant to Section 60 paragraph 1 of the Copyright Act.

In Prague 28. 07. 2016 Šárka Chlupová

Title: Study of deposition of catalytic materials into fuel channels of micro-fuel cells on a chip

Author: Šárka Chlupová

Department / Institute: Department of the Surface and Plasma Science

Supervisor of the master thesis: Doc. Mgr. Iva Matolínová, Dr.

Abstract:

This diploma thesis is interested in usage of Electron Beam lithography process as an instrument of transport of contacts and catalytic layers to micro-channels of the micro monolithic planar fuel cell. Experimental part includes optimization of the PMMA resist deposition method on the 3D topography – spray coating – is performed with alternative spar coating system. The optimal spin speed resist molecular weight and concentration is chosen during the optimization. Parameters of the exposition, developing and lift-off are also modified and three EBL processes are performed. The first ensures deposition of Au contacts to the channels; the second is for application of Pt layer to the cathode channel and the last aimed to cover the anode channel with CeO/CN_x layer. All layers are deposited by magnetron sputtering.

Keywords: Micro Fuel Cells, Electron Beam Lithography, Spraycoating

Contents

1. Introduction.....5
   1.1. Cell Unit.....6
   1.2. Fuel Cell Types.....8
      1.2.1. Direct Methanol Fuel Cell (DMFC).....9
      1.2.2. The Proton Exchange Membrane Fuel Cell (PEMFC).....10
   1.3. Micro Fuel Cells.....11
   1.4. Catalytic layers.....19
   1.5. Introduction to electron beam lithography (EBL).....20
      1.5.1. Process of electron beam lithography.....21
      1.5.2. Resist.....22
      1.5.3. Positive resists.....22
      1.5.4. Negative resists.....23
      1.5.5. Spin-coating.....23
      1.5.6. Spray-coating.....24
      1.5.7. Interaction of the resist material with electron beam.....25
      1.5.8. Proximity effect.....27
      1.5.9. Exposition.....28
      1.5.10. Developing.....29
      1.5.11. Resist sensitivity.....30
      1.1.1. Active layer deposition.....31
      1.1.2. FIB GIS.....33
      1.1.3. Lift-off.....33
   1.2. Experimental methods and equipment.....34
      1.2.1. Scanning electron microscopy (SEM).....34
      1.2.2. AFM.....36
2. Experiment.....38
   2.1. Optimization of sprayed resist layer on 3D topography.....38
   2.2. Test of EBL processes on the plain substrates.....56
   2.3. Additional modifications of parameters for EBL on structured substrate 59
   2.4. Deposition of contacts and catalytic layers into micro-channels.....60

2.5. Another approach to micro-channel fabrication 74
3. Conclusion 74
4. Bibliography 76

1. Introduction

Alternative ways of gaining energy belong to the most discussed and researched areas in modern society. The amount of energy demanded by population is still rising and resources of fossil fuel are decreasing. Scientists and researchers around the globe are looking for sustainable power source which would fulfil the demands and the expectations of modern world. Nowadays, the power gain is not the only indicator of a successful power source, but renewability and sensitivity to the environment are other qualities, which the power source should have.

A solution fulfilling both conditions seems to be found in very prospective power sources, fuel cells (FC). FCs bask in popularity and a deserved attention is paid to them during the last twenty years. However a principle of FC has been known for nearly two hundred years. The process of generating electricity from hydrogen and oxygen by reversing the electrolysis of water in FC was discovered by William Grove in 1839. This process has remained basically unchanged since then.

FCs are electrochemical devices that continuously and directly convert chemical energy confined in fuel into electrical energy (and some heat) for as long as fuel and oxidant are supplied. High efficiency and low environmental impact are promised by this process. FCs are considered to be similar to batteries due to the electrochemical nature of gaining electric energy and to combustion engines due to the continuous consumption of fuel. But the differences are what make the FC so interesting: No recharging is required for FCs, they operate quietly and effectively and when hydrogen is used as fuel the only products are electric energy, some heat and water. FC can be described as zero an emission combustion engine with no pollution. Other important advantage of FC in comparison with combustion engine is no thermodynamic limitation due to the efficiency of Carnot cycle.

Next to the promising usage of FC in transport industry, there is also a huge potential for usage in a medical care and in portable electronic industry which draw still larger amount of attention. This increase of attention is given by a rapid evolution of electronic devices such as cell phones, laptops, tablets. High expectations of portable electronic devices such as higher efficiency, larger amount of applications and multitasking lead to higher requirements on power sources used

in these devices. Rechargeable batteries do not seem to be sufficient enough. Micro-FCs appear to be the effective alternative.

The main aim of this diploma thesis is a modification of every step of the EBL process for 3D Si surface to enable a deposition of active layers to micro-channels of monolithic planar micro fuel cell.

1.1. Cell Unit

A scheme of a unit cell with flows of a fuel, oxidant gases, electrons and ions is shown in Fig.1. The basic physical block structure of the FC is common for all types of FC [1]. The FC unit consists of two electrodes (an anode and a cathode), to which lead the fuel and oxidant flows, and an electrolyte layer that mediates the ion transport between the electrodes. The electrons flow through a load.

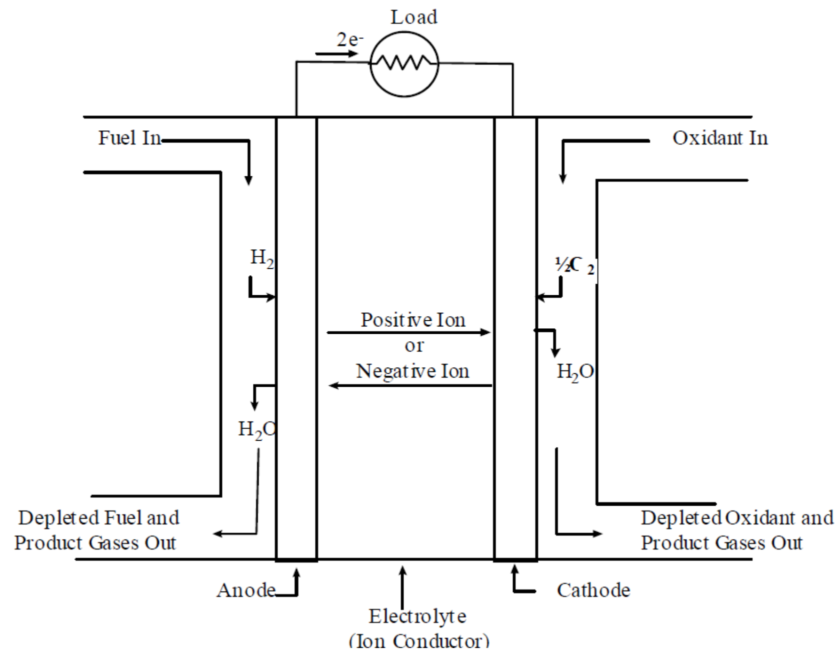

Fig. 1 – Scheme of an Individual Fuel Cell [2]

The fuel is continuously supplied to the anode and the oxidant is supplied to the cathode. The fuel and the oxidant gases are both dissociated on their corresponding electrodes and ions of the atoms of the dissociated gases are subsequently formed. One kind of the ions is then transported through the electrolyte from one electrode to the other. A product gas is formed on the latter as a result of electrochemical reactions and exits the fuel cell eventually.

It has been noted theoretically that every substance capable of chemical oxidization in fluid state is suitable to be a fuel supplement to the anode. Similarly the cathode supplement must be capable of chemical reduction in fluid state.

Nowadays the most widespread type of the fuel is gaseous hydrogen or its gas rich compounds. The main reason for this choice is that there are various ways of hydrogen production i.e. water electrolysis, chemical extraction from fossil fuels or from renewable fuels. Similar reason leads to a wide usage of gaseous oxygen as the oxidant.

Higher demanded voltage or magnitude of power output from FC requires multiple unit cells to be placed and connected in a modular fashion into a so called cell stack [2]. The most common fuel stack applied in FC research is a planar-bipolar arrangement shown in Figure 2. Unit cells are mutually connected via interconnect plates which also serve as separators that prevent mixing of fuel and oxidant of the adjacent cells. In some designs, in which fuel and oxidant flow channels are integrated on a plate, the interconnects operate as the fuel and the oxidant distributors. The interconnects are then called field flow plates.

Another type of the fuel stack is used particularly for FCs operating at high temperatures. This type is known as stack with tubular cells. Its advantages are better gas sealing and higher structural integrity of the cell.

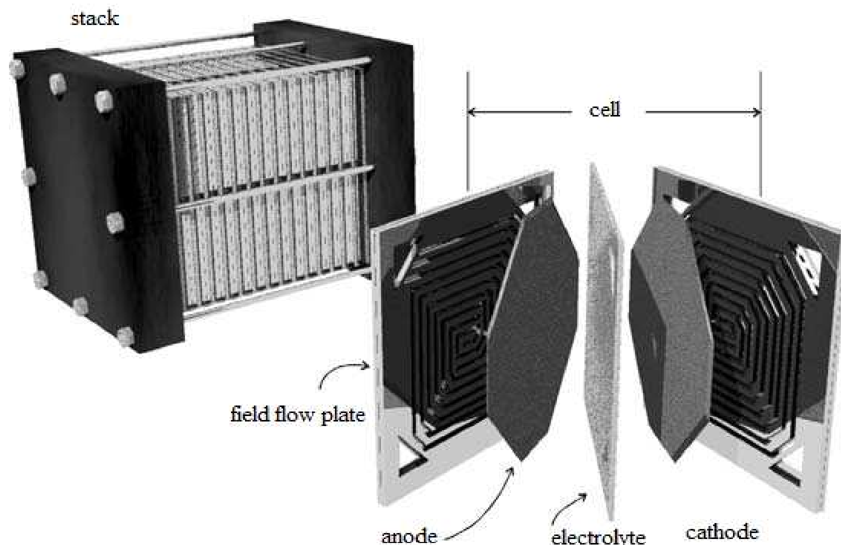

Fig. 2 – Fuel cell stack made up of bipolar plates [1]

1.2. Fuel Cell Types

The types of the FCs are most commonly sorted by the kind of electrolyte operating in the cell. This sorting includes 1) Solid Oxide Fuel Cell (SOFC), 2) Molten Carbonate Fuel Cell (MCFC), 3) Alkaline Fuel Cell (AFC), 4) The Direct Methanol Fuel Cell (DMFC), 5) The Phosphoric Acid Fuel Cell (PAFC) and 6) Polymer Electrolyte Fuel Cell (PEFC).

Required thermomechanical and physicomechanical characteristics of the component materials of the FCs are highly dependent on the combination of the electrolyte, the operating temperature and the useful life of the FC. For example a rapid degradation and high vapor pressure can be observed at higher temperatures for FCs with aqueous electrolyte. The operating temperature has also influence on the state of the supplemented fuel. Low-temperature fuel cells can be supplied only by pure hydrogen. The main FC groups are summarized in Table 1.

	PEFC	AFC	PAFC	MCFC	SOFC
Electrolyte	Hydrated Polymeric Ion Exchange Membranes	Mobilized or Immobilized Potassium Hydroxide in asbestos matrix	Immobilized Liquid Phosphoric Acid in SiC	Immobilized Liquid Molten Carbonate in $LiAlO_2$	Perovskites (Ceramics)
Electrodes	Carbon	Transition metals	Carbon	Nickel and Nickel Oxide	Perovskite and perovskite / metal cermet
Catalyst	Platinum	Platinum	Platinum	Electrode material	Electrode material
Interconnect	Carbon or metal	Metal	Graphite	Stainless steel or Nickel	Nickel, ceramic, or steel
Operating Temperature	40 – 80 °C	65°C – 220 °C	205 °C	650 °C	600-1000 °C
Charge Carrier	H^+	OH^-	H^+	$CO3^=$	$O^=$
External Reformer for hydrocarbon fuels	Yes	Yes	Yes	No, for some fuels	No, for some fuels and cell designs
External shift conversion of CO to hydrogen	Yes, plus purification to remove trace CO	Yes, plus purification to remove CO and CO_2	Yes	No	No
Prime Cell Components	Carbon-based	Carbon-based	Graphite-based	Stainless-based	Ceramic
Product Water Management	Evaporative	Evaporative	Evaporative	Gaseous Product	Gaseous Product
Product Heat Management	Process Gas + Liquid Cooling Medium	Process Gas + Electrolyte Circulation	Process Gas + Liquid cooling medium or steam generation	Internal Reforming + Process Gas	Internal Reforming + Process Gas

Tab. 1 – Summary of Major Difference of the Fuel Cell Types [2]

1.2.1. Direct Methanol Fuel Cell (DMFC)

The direct methanol fuel cell is often said to be the optimal fuel cell system because of the non-transformed form of the fuel they are operating with and the simplicity of the cell system.

In contrast with indirect fuel systems, which have to be fed by pure hydrogen, the direct cells such as DMFC can be fed directly by methanol or alcohol, which are organic fuels.

1.2.2. The Proton Exchange Membrane Fuel Cell (PEMFC)

Simplicity and high power density are the qualities of proton exchange membrane FC that make it the most promising FC for application in various fields such as portable power generators or stationary power generators. However its most promising application is expected to be in a transport industry [2].

PEMFC was given its name by special polymer membrane used as electrolyte. DuPont was the first inventor of the plastic membrane usable for FC (even though originally the membrane should have had different utilization). The final result of the DuPont's research is a compact unit cell consisting of the polymer membrane between the electrodes, called *membrane electrode assembly* (MEA) (see Figure 3). This assembly is usually few microns thick and it is the most important part of the PEMFC. The process of the electrochemical power generation is driven by the necessary electro catalysis which takes place in the inter-facial thin layers between each electrode and the membrane. Specific attribute of the membrane is its dependence on a liquid water presence. Water is vital for the effective conduction of protons, but on the other hand it limits the maximal operation temperature of the PEMFC.

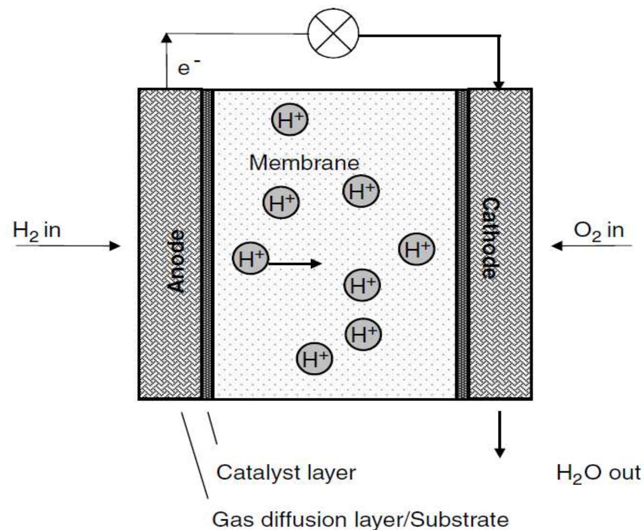

Fig. 3 – Membrane electrode assembly [2]

Figure 3 can be used to demonstrate the electrochemical reactions occurring on the anode and the cathode catalyst layer. The gas diffusion layer allows the hydrogen molecules and atoms to reach the active catalytic layer on the anode. After the

chemical reaction (Eq. 1.2.1), the protons pass through the ion conducting membrane to the cathode side and electrons travel through the substrate to the load.

$$H_2 \rightarrow 2H^+ + 2e^- \left(E_r = 0V\right) \quad (1.2.1)$$

For MEA to be even operative, the anode layer has to be gas-porous and electronically conductive. The porosity also serves as heat conducting feature for letting out the heat that is formed as side-effect of chemical reaction.

Situation on the cathode side can be characterized by Eq.1.2.2 where the product water is formed.

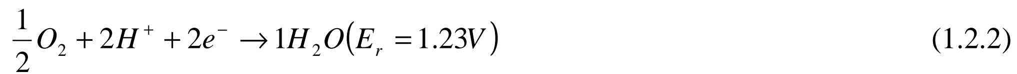

$$\frac{1}{2}O_2 + 2H^+ + 2e^- \rightarrow 1H_2O\left(E_r = 1.23V\right) \quad (1.2.2)$$

Water leaves the cathode in a liquid form. This could cause problems with water sealing the active porous structure and preventing the oxygen molecules from entering [2].

1.3. Micro Fuel Cells

All types of FCs mentioned in previous section have been intensively developed and investigated also in micro-scale during the last fifteen years [3]. Tendencies to miniaturize fuel cell systems require methods with satisfactorily preciseness. Microelectromechanical systems (MEMS), which are traditionally used in semiconductor industry, seem to be a promising procedure to fabricate the micro-FCs. Wide range of resources, financial as well as intellectual, had been spent on development of micro-DMFC and micro-PEMFC systems via MEMS, which resulted in publication of several works dealing with this topic. Potential mass production could be possible thanks to this technology which also gives a solution to critical problems in conventional stack technology: Improvement of power and current densities is provided by precise movement of fuel, air and water within the electrodes and MEMS allows for fabrication of transport-optimized micro-flow field plates of different dimensions. The extreme decrease of the size of the FC leads to

the need of change of the technological processes as well as to a complete change of the cell materials. For example conventional graphite must be replaced by silicon.

Silicon substrates open wide range of possibilities in MEA fabrication for FCs. Other materials such as silicon oxides, nitrides or carbides that are commonly used in semiconductor industry can also participate in the fabrication process.

Regardless of the assembly of the FCs, the common procedure of MEMS technology stays more or less the same. First step is patterning the silicon wafer with micro-flowing channels by Deep Reactive-Ion Etching (DRIE) where the negative photo resist serves as an etching mask. Wet chemical etching can be applied as well [4]. Next step is sputtering Au or Cu/Au layers on silicon wafer in order to create the current collectors (titanium/tungsten layer placed as an adhesive underneath the current collectors has been proven advantageous). Then the electrodes are either coated by active catalytic layer and the membrane is finally attached by pressing or the active catalytic layer is deposited by direct coating on the surface of a membrane. Last option of deposition is magnetron sputtering.

There are currently two types of arrangement for micro-fuel cells prepared with MEMS technology. The first one uses two silicon wafers with separated electrode on each wafer. This is a conventional assembly. The first micro-FC fabricated with this arrangement was interesting with its “flip-flop” design [5]. Many studies were interested in patterned micro-electrodes with more or less successful design alternations [6-11].

The second assembly is a monolithic FC on a single silicon wafer. This design of micro-DMFC was firstly brought up by Motokawa et al. [12] and its working principle is pictured in Figure 4. The working principle is still similar to the classic FC. A chemical solution $CH_3OH/H_2SO_4/H_2O$ is used as a fuel. The results of reduction reaction taking place on catalytic layer of anode side are protons, electrons and carbon dioxide. The electrons create useful electric current that can be made use of in the load before they are directed to the cathode and participate in oxidation reaction with fed oxidant solution (O_2-sat./H_2SO_4/H_2O) and with protons transported through ion-conductive membrane from the anode side. Final product of this process is water. The proportions of the contact between electrodes are given by thickness of the Nafion membrane, which is in this case 50 μm, and by width of cross section between micro-channels.

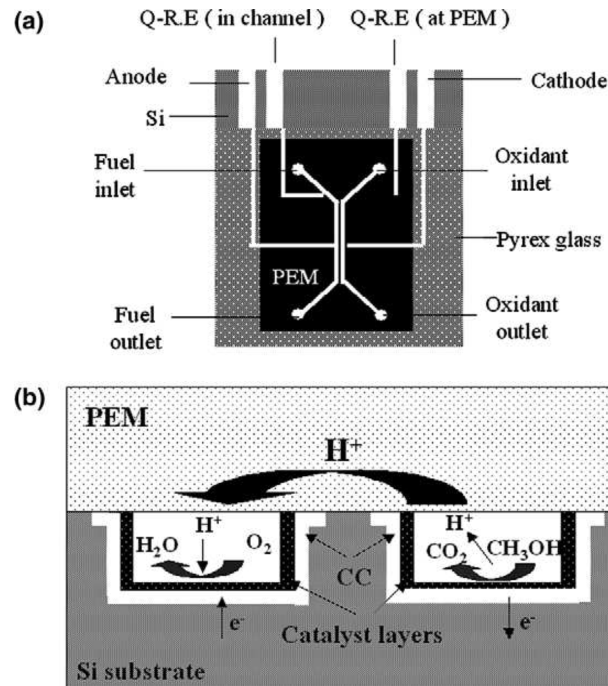

Fig. 4 – Schematic diagrams of planar micro-fuel cell: (a) top-view of design; (b) cross-sectional schematic with working principle.

The assembly described in Figure 4 presents many differences and various advantages from the system with two silicon wafers with separated electrode on each wafer [12]:

- It is of planar structure and essentially an unfolded fuel cell as shown in Figure 5, which integrates the anode and cathode onto a single Si surface.
- The fuel and oxidant are supplied to the cell in isolated, separate micro-channels. The fuel and the oxidant are both distributed throughout the wafer via micro-channels and they both possess exhausts. The isolation of fuel and oxidant precludes one from crossing the fuel and oxidants streams.
- The distance that the protons must travel from anode to cathode, i.e. *the characteristic length of the system*, is very short.
- This makes the system less sensitive to ohmic impedance effect.
- The efficiency of the current collectors is high, because the catalyst layers are supported on the metal directly. In addition the current collectors are directly deposited in micro-channels. The current does not need to be pulled out by relatively large metal lines.
- Catalyst electrodes are directly fabricated in the bottom and sidewalls of the micro-channels.

Achieving such an extremely small size of this FC system (active area = 0.018 cm^2) is possible thanks to the implementation of the cathodic and anodic micro-channels to a single silicon wafer. For this task, advanced MEMS steps are used (Figure 5) including photo-lithography, DRIE and electron beam deposition. The fabricated micro-channels are connected with conventional electrolyte membrane (Nafion by DuPont) and filled with catalysts, where Pt-Ru is deposited to anode and Pt to cathode. Electron beam lithography is used for an application of the Ti/Au current collectors. The fuel cell system generates 0.78 $mWcm^{-2}$ at 3.6 $mAcm^{-2}$. This low value of attainable power can be caused by imperfect non-high pressure bonding between substrate, membrane and glass layer.

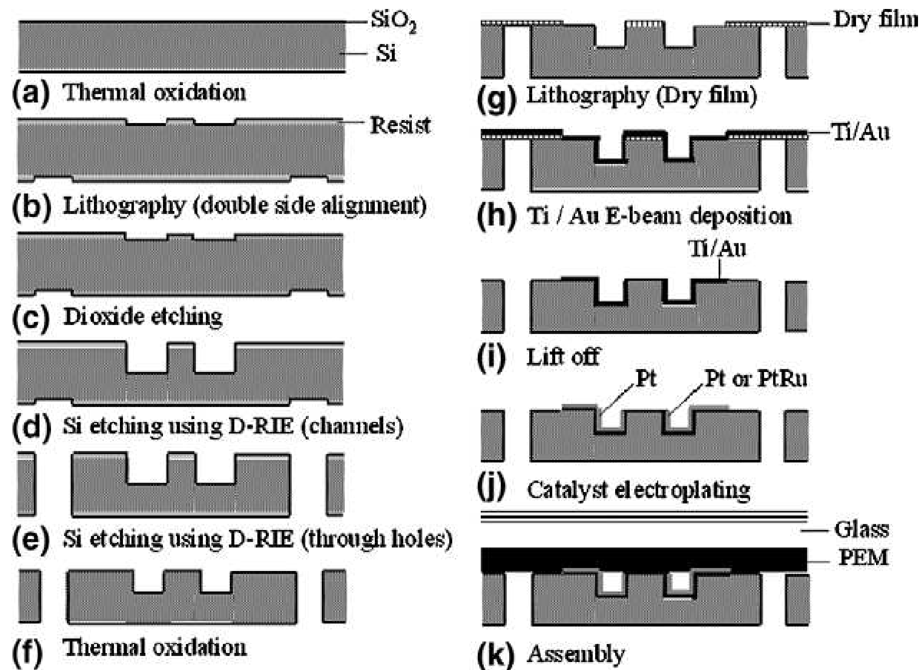

Fig. 5 – Schematic of the l-DMFC chip fabrication process.

Another preparation approach is proposed by Ishizuka et al. [13]. The dioxide etching is substituted by KOH chemical etching resulting in V-shaped micro-channels which are completely different from the previous ones. The photo-resist is deposited on 3D substrate by spray coating method and patterned by photo lithography. The wet etching method is chosen due to final V-shape of channels which improves access of irradiating beam to slanted sidewall from upper direction.

Next steps of MEMS technology remain unchanged. Pt-Ru is added to anode side and Pt to cathode side as catalytic layers. Nafion112 is used as PEM membrane connecting the electrodes. Final layers are clamped mechanically with low press sealing.

The electrodes are fed with the same fuel and oxidant as in the previous study, so (2M methanol / 0.5M sulfuric acid / H_2O) is used as the fuel and (O_2-sat / 0.5M sulfuric acid / H_2O) as the oxidant. The fuel flow rate is 5 ml/min, and the oxidant flow rate is 50 ml/min. The maximum power density and open circuit voltage obtained at room temperature with 2M methanol are 0.72 $mWcm^{-2}$ and 548 mV respectively.

Other alternatives of monolithic micro FCs were successfully developed. For example membrane-less micro-fuel cells [14-16] or completely different assembly [17].

Systems similar to the one that was proposed by Motokawa et al. are extensively studied. Investigation of fuel and oxidant transportation in FC system and its characteristics were explored by Chen et al. [18]. They also performed a numerical study of the FC system.

The system configuration is depicted in Figure 4 and the cross-sectional view is the same as in the Figure 6. Electrochemical reactions are assumed to take place only on deposited layers in the U-shaped micro-channels. Half-reaction of the methanol on the anode side is listed below.

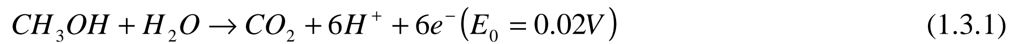

$$CH_3OH + H_2O \rightarrow CO_2 + 6H^+ + 6e^- \left(E_0 = 0.02V\right) \quad (1.3.1)$$

When protons trespass through the Nafion membrane and the electrons via an external circuit they reach the cathode. The oxygen contained in the flow added to cathodic side participates in a half-reaction with them as follows

$$2O_2 + 6H^+ + 6e^- \rightarrow 3H_2O\left(E_0 = 1.23V\right) \quad (1.3.2)$$

The combination of both aforementioned half-reactions covers the whole reaction that is usually associated with micro-DMFC:

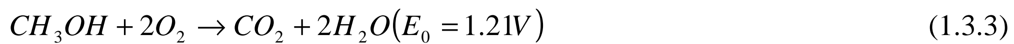

$$CH_3OH + 2O_2 \rightarrow CO_2 + 2H_2O\left(E_0 = 1.21V\right) \quad (1.3.3)$$

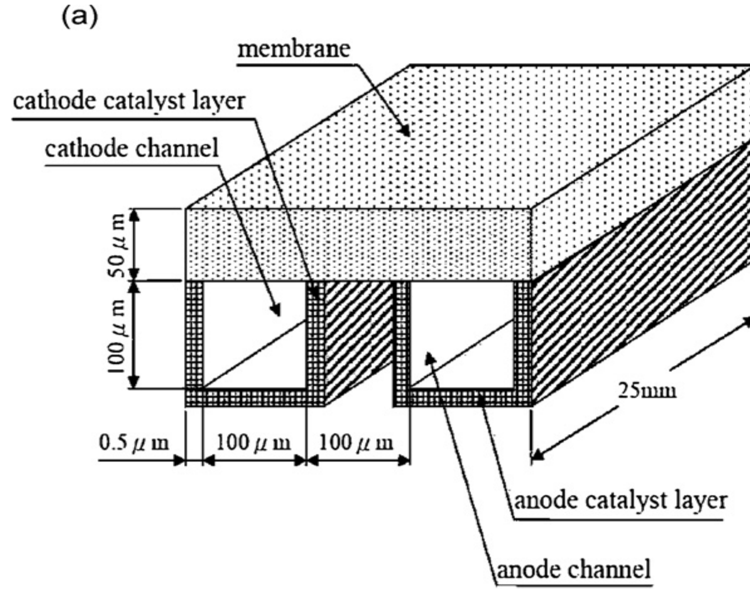

Fig. 6 – The diagram of system configuration [18]

In order to simplify the simulation of the FC operation, there are special conditions presumed: pressure is 1 atm, temperature is 25 °C and the flows are isothermal and incompressible. The leading phenomenon includes transport of the reactant, charge, mass and momentum in this concrete micro-DMFC. Movement of the liquid streams within the micro-channel can be described by the Navier–Stokes equation, continuity equation, and Fick's law as written below:

$$\nabla \cdot U = 0, \tag{1.3.4}$$

$$\rho\left[\frac{\partial U}{\partial t} + \nabla \cdot (UU)\right] = -\nabla p + \mu \nabla^2 U, \tag{1.3.5}$$

$$\rho\left[\frac{\partial}{\partial t} Y_i + \nabla \cdot (UY_i)\right] = \nabla \cdot J_i, \tag{1.3.6}$$

where ρ is the fluid density, *U* the flow velocity, *p* the pressure, μ the dynamic viscosity, *Yi* the mass fraction of i-th species, and *Ji* is the diffusion flux.

Events on the catalysts and the membrane can be expressed by equations:

$$\frac{\partial}{\partial t}(\varepsilon\rho) + \nabla \cdot (\varepsilon\rho U) = 0, \tag{1.3.7}$$

$$\frac{\partial}{\partial t}(\varepsilon\rho U) + \nabla \cdot (\varepsilon\rho UU) = -\varepsilon\nabla p + \nabla \cdot (\varepsilon\tau) - \frac{\varepsilon^2 \mu U}{\kappa} - \frac{\varepsilon^3 C_F \rho}{\sqrt{\kappa}}|U|U, \tag{1.3.8}$$

$$\frac{\partial}{\partial t}(\varepsilon\rho Y_i) + \nabla \cdot (\varepsilon\rho UY_i) = \nabla \cdot J_i + \dot{\omega}_i, \tag{1.3.9}$$

where ε is the porosity, τ the shear force tensor, κ the permeability, C_F the quadratic drag factor, and ωi is the production rate of the i-species. The last two parts at the end of the Eq.(1.3.6) represent the interaction between porous walls and stream in the pores. The consequence of these relations is a significant pressure drop across the porous structure caused by additional drag force. In special case of pure liquid when $\varepsilon \to 1$ and $\kappa \to \infty$, the Eq (1.3.5-7) become the same as Eq(1.3.2-4). Electrochemical reaction in the catalytic layer is expressed by the source term ωi in Eq. (1.3.7). This term should be zero in the area of the membrane.

Electric field takes the main part in characterization of the charge transport. In liquid stream it is defined by

$$\nabla \cdot i = 0\,, \tag{1.3.10}$$

where i is the vector of current density. This equation indicates continuous behavior and under certain circumstances it can be divided into two parts corresponding to different electric fields in membrane and in porous structure

$$\nabla \cdot i_F + \nabla \cdot i_S = 0\,, \tag{1.3.11}$$

where i_F is the current density in the polymer electrolyte (ionic phase), and i_S is the current density in the solid or electronic phase of the porous matrix.

Correlation below indicates settled location, where the electrochemical reaction takes place, which is only on the catalytic porous layer

$$-\nabla \cdot i_F = \nabla \cdot i_S = S\,, \tag{1.3.12}$$

where S is the reaction rate in terms of unit Am^{-3}. Furthermore, the Bulter–Volmer equation is used to estimate the loss of overvoltage and can be written in the general form:

$$S_i = aj_0\left(\frac{C_i}{C_i^0}\right)^{\beta_i}\left[\exp\left(\frac{\alpha_a nF}{RT}\eta\right)-\exp\left(-\frac{\alpha_c nF}{RT}\eta\right)\right], \tag{1.3.13}$$

where a is the density of the catalyzed active area on the electrode, j_0 is the exchange current density at the reference reactant concentration C_0, Ci is the concentration of

species i, βi is the reaction order, α_a and α_c are the charge transfer coefficients, respectively for the anode and cathode reactions, n is the number of electrons transferred in the reaction, R is the universal gas constant, T is the absolute temperature, and η is the overvoltage.

Performed simulation gave interesting results. It turned out that cell performance was strongly dependent on the material of the catalytic layer at the anode side. Catalytic layer of Pt-Ru was proved to be more efficient than pure Pt. All other results were thus obtained for Pt-Ru catalytic layer. Results showed independence of the cell performance on concentration of methanol on the anode side and zero penetration of methanol through the crossover between the electrodes. Moreover it was shown that the concentration of oxygen at the cathode side drops significantly on the way from the inlet to outlet. It causes strong resistance of mass transfer of reactant on the reaction side, which can be observed mainly near the outlet of micro-channel. Higher oxygen concentration (which is usually difficult to gain) would probably be the solution to achieving better cell performance.

Another solution would be increasing the volumetric flow rate. Higher volumetric flow rate causes faster movement of liquid stream and it compensates the changes of concentrations along the micro-channel. The volumetric flow rate, however, cannot be increased infinitely. At some point it reaches the critical value above which the current density becomes independent on it.

The porosity and thickness of the catalytic layer are other vital parameters for FC performance. For example higher porosity decreases the transport resistance because of easier access of oxidant and fuel into catalytic layer and it also expands the active surface.

The improvement can be also gained by adjustment of geometric measures of the micro-channels. It would seem that lengthening the micro-channels will result in larger active area and higher cell performance. However for given volumetric flow rate the oxygen concentration decreases along the channel with its increasing length. The possible way is to change the aspect ratio of the cross-section of micro-channel. Results of a simulation indicate that wider and lower channels slightly help to stop the decrease of oxygen concentration.

1.4. Catalytic layers

The model micro-DMFC shows that the porosity of catalytic layer plays a significant role for FC performance and research of this problematics could prove to be beneficial. One way to achieve more porous catalytic layer is to modify the silicon substrate itself. This modified silicon substrate can be used as gas diffusion layer, catalyst support or a membrane in many FC applications [4]. Another procedure to increase the porosity of catalytic layer is to modify its direct deposition.

During a development of new types of catalytic layers in research group of prof. Matolín, it was found out that not only have thin sputtered CeO layers containing Pt higher specific power than Pt-Ru in case of deposition on anode side of classic stack FC, but it also shows significantly higher porosity in case of deposition on various carbon supporting layers such as glassy carbon, carbon nanotubes, amorphous carbon (a-C) or nitrogenized amorphous carbon [19].

The reaction which leads to this porosity is explained in [19] as etching process of the carbon substrate by oxygen particles (radicals, ions etc.), which is happening simultaneously with deposition of cerium oxide.

Next study is interested in growth mechanism of cerium oxide layers on a-C and CN_x supporting layers with dependence on deposition parameters of magnetron sputtering [20], Figure 7. These parameters are for example deposition rate, deposition time or composition of working gas. Results show that increasing the concentration of the oxygen gas in the working gas leads to higher etching effect followed by higher porosity of either CN_x or CN_x-CeO system. There exists an optimum value of oxygen concentration for which the porosity is maximal. Further increase of oxygen concentration leads to decrease of the porosity of the layers. Similar dependence is observed for a-C layer. Thicker deposited layer of CeO resulted in significantly higher porosity of CN_x but did not have such significant effect on a-C.

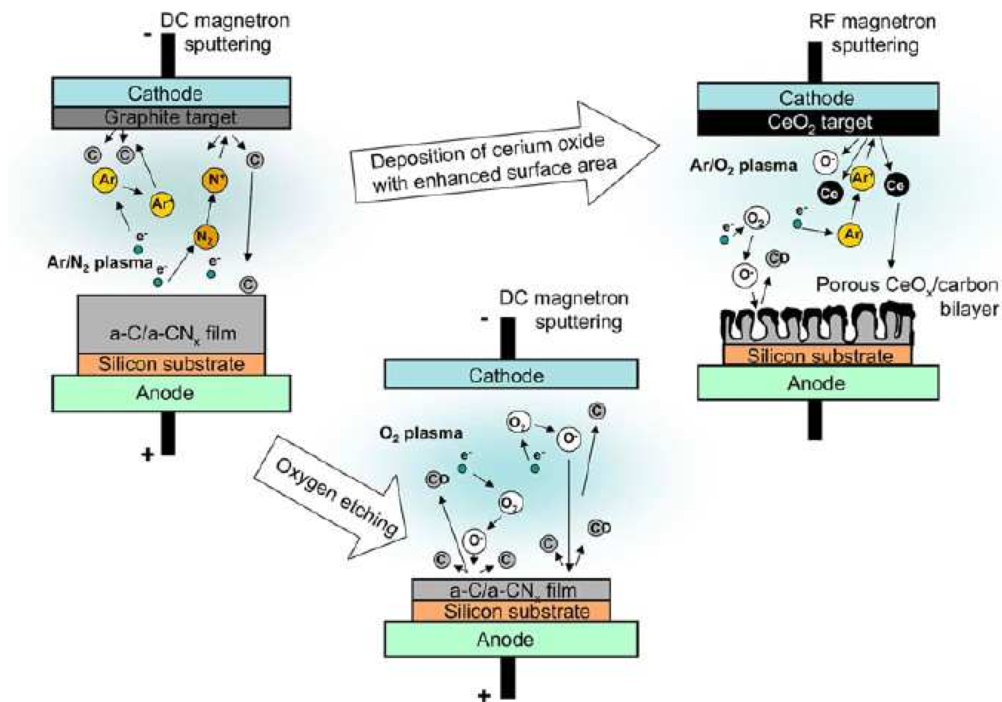

Fig. 7 – Growth mechanism of cerium oxide during magnetron sputtering [20]

1.5. Introduction to electron beam lithography (EBL)

In the last chapter the term e-beam lithography is mentioned and this chapter should summarize fundamentals of this method.

Lithography in general is a process of matrix replication to thin film or substrate through prepared polymer mask. Substance used for mask preparation is called resist. Many alternatives of lithographic methods have been developed in last sixty years. The usual classification depends on a type of a radiation that is applied to the photosensitive resist. The types of radiation used are photon beam, electron beam, focused ion beam, neutral atom beam and X-ray. Despite the different types of radiation and instrumental assemblies used for various lithographic methods the basic principles remain unchanged.

One of the most precise lithographic methods is electron beam lithography. This procedure is desired mainly in microelectronic industry for its capability of creating very fine micro- and nanostructures.

Modern electron beam lithography technic is inspired by old classes of scanning electron microscopes, where electron beam scans the surface. In case of lithography the electron beam exposes areas of resist layer according to required matrix.

1.5.1. Process of electron beam lithography

During the electron beam lithography process, the following procedure is usually executed: (a) the substrate is prepared and purified; (b) solution of solvent with polymer is applied on cleaned substrate and spread by spin-coating technique. The outcome is the photosensitive resist layer; (c) exposition of resists layer is performed especially in advanced electron microscope with lithographic tools. Irradiation takes place only at predefined positions. Chemical changes occur at the irradiated places and the nature of the chemical reaction depends on type of resist layer; (d1) in case of positive resist, the irradiated areas are removed by developer; (d2) in case of negative resists, these areas stand and the rest is removed. The result is a lithographic resist mask; (g, h) the active or functional layers are deposited over this resist mask during the deposition process; (I, j) final step is lift-off process during which the rest of the resist mask is detached and only the active layer remains in areas defined by prepared matrix.

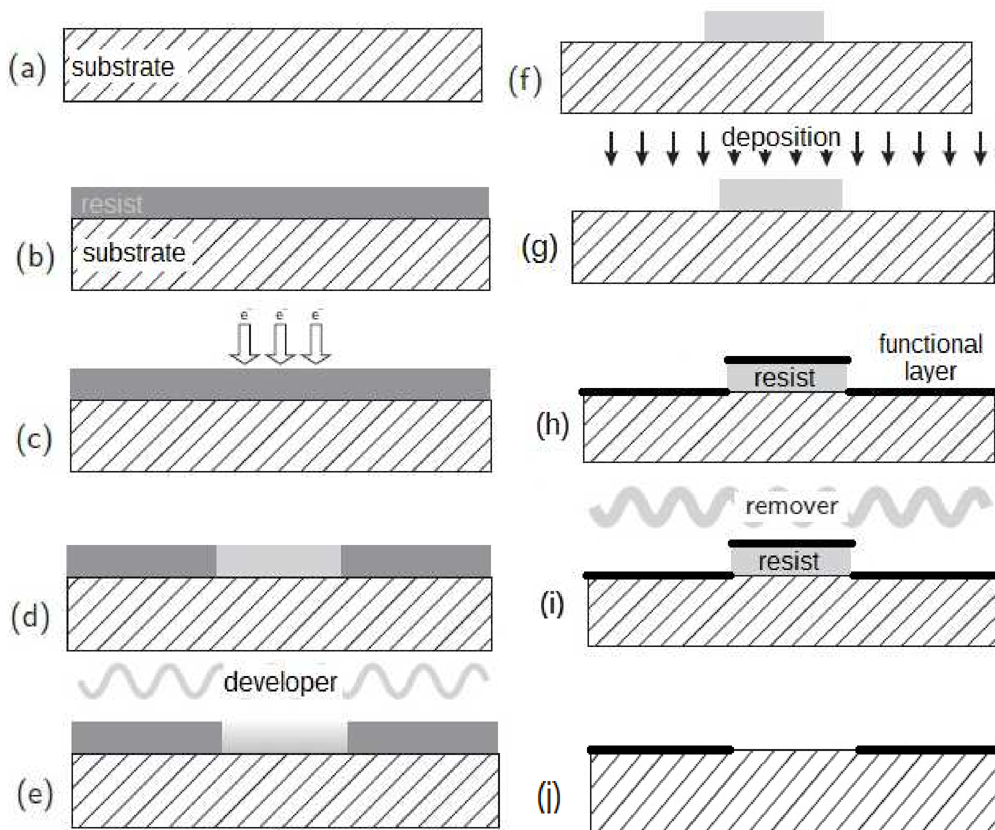

Fig. 8 – EBL process of negative lithography

1.5.2. Resist

Photosensitive resist is a recording and transporting medium for photo-lithography or electron beam lithography. It is a material on which a record can be written with photon or electron beam.

Resist materials are divided into two main groups: the negative resists and the positive resists. Positive resists dilutes preferably during the process of exposition. The negative resists behave exactly the opposite [21].

1.5.3. Positive resists

Positive resists are commonly used for electron beam lithography. These materials are usually subdivided into two subgroups – subclasses – according to the chemical process which occurs during irradiation. Resists of the first class consist of two compounds, the photoactive part and the resin. The photoactive part dissolves during exposition. This kind of material has been frequently used for photolithography, nowadays it is used for electron beam lithography too.

The second subclass is represented by resist materials which consist of long polymeric molecules. During irradiation a degradation of long bonds between monomers takes place (scissoring) and then the polymer strings are more soluble in developer.

Poly(methyl methacrylate) (PMMA) is the most wide spread and commonly used positive resist. The main advantages of its usage are a good resolution and indifference to the visible light. The main disadvantage is low sensitivity. PMMA is an insulator. Structural formula is shown in Figure 9:

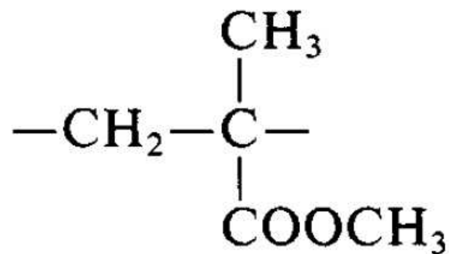

Fig. 9 – Structural formula of PMMA [21]

The chemical and physical properties of PMMA depend on molecular weight, in other words on the length of the polymer chain, and can be defined by [22]:

Mi – mass molar weight

Mv – average molar weight

d=Mi/Mv – dispersion of polymer

Other representatives of positive resist group are PBS (polybutylene succinate) or ZEP (copolymer clormethacrylate and methylstiren) [23].

1.5.4. Negative resists

Materials for negative resists also contain polymer molecules. However, scissoring is not the dominant reaction during exposition. The process which appears is cross-link. Cross-link is a process of multiplication of the bonds across the whole polymer string and these modified bonds create a “tangled web”. COP (copolymer glycidyl metacrylate and ethylacrylate) and SU-8 [23] are most common representatives of this group and also PMMA behaves as negative resist after extreme exposition dosage (>5000 $\mu C/cm^2$).

1.5.5. Spin-coating

Spin-coating is a very common method for production of thin and uniform polymer layer on a plain substrate.

The first step of the spin-coating is an application of a solution containing polymer and solvent over the flat, cleaned substrate. Then, the system is accelerated to desired spin velocity. The fluid is radially distributed by centrifugal forces. It is pushed to edges of the substrate where the surplus of the solution leaves the system. The forming resist film gets thinner and thinner till it reaches uniform thickness or till it is changed to solid due to increasing viscosity caused by solvent evaporation [25].

The process of the spin-coating implies a strong dependence of the resist thickness on the spin velocity, on the type of the solvent and the dissolved polymer, on the molar weight of the polymer and on the concentration of the solution [26]. The temperature and size of the substrate also play not negligible role.

Dependence of the resist thickness *t* on some of the mentioned parameters can be described by formula below [27]:

$$t = \frac{KC_0\left(\nu_0 D_0\right)^{\frac{1}{4}}}{\omega^{\frac{1}{2}}}, \qquad (1.5.1)$$

where K is a constant, C_0 is original solvent viscosity, v_0 is kinematic viscosity, D_0 is solubility of the polymer and ω is the spin velocity.

Unfortunately, the resist thickness is usually not uniform over the whole substrate. As was mentioned before, while the fluid is distributed to the edges it turns into solid before it reaches uniform thickness. This problem is described as [22]:

$$\Delta t = \sqrt{\frac{2\gamma}{s\omega^2 r}}, \tag{1.5.2}$$

where Δt is thickness increase on the edges, which is dependent on the surface tension γ, the subtrate radius r and the solution density s.

Resists thickness can be also predicted from the *spin-curves*. The *spin-curves* describe the dependence of the layer thickness on the spin speed. Each *spin-curve* is usually plotted for different concentrations of different molar weights of polymer.

When the spin-coating process is finished, the system of the substrate and the formed resist film must be thermally preserved. This can be performed by hot-plate method, when the sample is laid on the hot plate, or by baking, when the sample is placed into oven [28].

The preservation process is performed in order to initiate evaporation of the residual solvent in resist film and to improve the adhesion between the resist layer and the substrate. Temperatures used during this process are chosen to be over the glass transition temperature (approx. 105 °C). On the other hand they cannot be too high because this would lead to resist degradation.

1.5.6. Spray-coating

When electron beam or optical lithography is used on surfaces with coarse topography, the application of continuous polymer resist film by spin coating method is failing.

In these cases spray-coating is known to be more suitable method due to significantly better final coverage of the sample by resist layer than in case of commonly used spin-coating. Spray-coating is usually connected with UV lithography [13, 29], but an optimization of sprayed resist is made even for EBL [30].

The spraying is realized by ultrasonic atomizer, which generates an aerosol of small resist droplets. The aerosol is then carried by air flow of adjustable pressure through the spray nozzle to the substrate surface (see Figure 10).

The continuity of the resist or uniformity of its thickens can be optimized via several parameters such as the dispense rate of the nozzle, the scanning profile of the nozzle, the distance between the nozzle and the substrate, the solids content of the resist solution or dispensed volume per layer. A quick drying of the sample after spray coating is often mentioned to be of utter importance. If the sample is not dried quickly then the sprayed particles of resist solvent have time to coalescent after landing at the surface and to create large droplets. The large droplets then flow down the sloped micro-structure and collect at the cavities. The quick drying of the sample prevents such a behavior of the resist solvent, but it also enhances the roughness of the surface of the applied resist. Thus it is important to optimize the drying process and find a balance between those two mentioned effects.

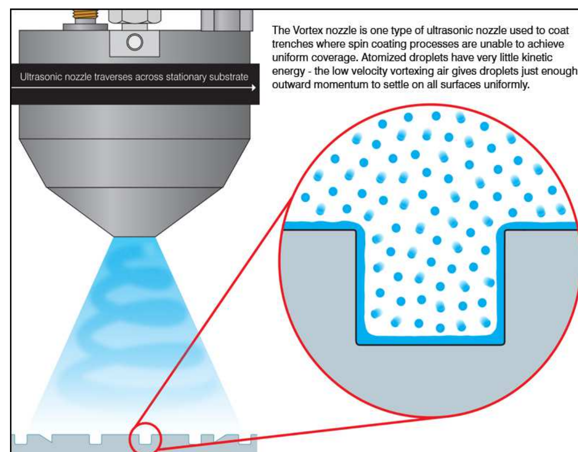

Fig. 10 – Ultrasonic nozzle *(http://www.sono-tek.com/photoresist-spray-equipment/)*

1.5.7. Interaction of the resist material with electron beam

Electron lithographs are capable of extremely fine, focused and stable electron beams. However, situation can get interesting, when the electrons from the beam reach the surface of the sample [23]. Electrons can undergo several scattering events, which can be divided as elastic and inelastic events.

First elastic scattering event, which the electron entering the sample surface can experience, is a *forward scattering* during which the direction of the electron is changed of small angle. These electrons cause the widening of the area originally

exposed by primary e-beam. Increase of this value can be described by empiric formula [23]:

$$d_f = 0{,}9\left(\frac{t}{V_b}\right)^{1{,}5} \qquad (1.5.3)$$

Where t is resist thickness in nanometers, d_f is an effective diameter of the electron beam and V_b is applied high voltage in kilovolts.

Other electrons, which penetrate through the resist layer, can participate in *backscattering* events, when the elastic interaction with significantly heavier atoms of substrate does not change the electrons' energy but changes the electrons' direction by large angle [31]. Electrons participating in these interactions are the cause of the proximity effect. It is a phenomenon when point of the exposed matrix is irradiated not only by electrons from primary beam but also by backscattered electrons, which were scattered by heavy substrate atoms during irradiation of previous matrix points.

The inelastic interactions of the primary electrons ensure transmission of a part or of a whole kinetic energy to electrons in an atom which leads to excitation or ionization of the atom. If the atom is part of resist macromolecule, the interaction can initiate chemical changes in polymer string and break it. Another product of this interaction is the cascade of electrons with low energy, called secondary electrons. Their energetic range is 2-50 eV. These electrons are truly responsible for the bulk of the exposition process, because they primarily cause chemical changes in polymer molecules which can end up by scissoring or cross-link. Secondary electrons also have influence on resolution of the exposition. They contribute maximally 10 nm to widening of exposure area which is given by their limited movement in material due to low energy.

Electron scattering in the system of resist layer on silicon substrate is simulated for two energies by Monte Carlo method in [23] and pictured in Figure 11.

Most of the energy of electrons is transformed to heat during the penetration of resist layer. Because of the thermal instability and bad thermal conductivity of resist material, thermal effects should be taken into consideration. The heating can cause local temperature differences up to tens of degrees of Celsius, which depends on the current density per square and on the type of the substrate [32]. Thermal power

increases with current density and can cause local overheating. Inconveniently chosen current can lead to thermal exposition in places, which do not even get to contact with electron beam.

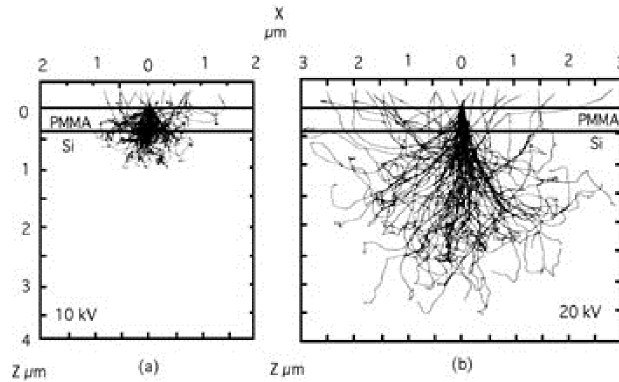

Fig. 11 – Simulation of electron scattering on Si substrate for high voltage a) 10 keV and b) 20 keV by Monte Carlo method [23]

1.5.8. Proximity effect

Proximity effect, as mentioned before, is mostly consequence of backscattered electrons, which are scattered on heavy atoms of substrate back to resist layer [33]. These electrons are the reason of the exposition of areas quite distant from places originally exposed. Amount of the backscattered electrons - in other words the intensity of *proximity effec*t - is dependent on applied high voltage and on consistence of substrate.

Algorithm for *proximity effect* correction requires precise knowledge of profile of energy density applied on exposed resist layer in one irradiated pixel. Generally, the profile is a function of system settings. Important properties of this profile are that its shape is independent on a dose of radiation and on position on a sample in case of plane homogenous substrate. This profile is usually approximated by sum of Gaussian distributions [31]:

$$f(r)=\frac{1}{1+\eta}\left(\frac{1}{\pi\alpha^2}\exp\left(\frac{-r^2}{\alpha^2}\right)+\frac{\eta}{\pi\beta^2}\exp\left(\frac{-r^2}{\beta^2}\right)\right), \tag{1.5.4}$$

where *n* is ratio of backscattered energy and forward scattered energy, α is a parameter of the forward scatter range and β is a parameter of backscattered range. Quantitative characterization of the *proximity effect* is conventionally performed by

the modulation transfer function. This function can be obtained by Fourier transforming and normalizing the energy density profile [31]:

$$MTF = \frac{1}{1+\eta}\left(\exp\left(-\frac{\pi^2\alpha^2}{p^2}\right)+\eta\exp\left(-\frac{\pi^2\beta^2}{p^2}\right)\right), \quad (1.5.5)$$

where p is the spatial period.

1.5.9. Exposition

Exposition usually takes place in aforementioned electron lithograph or in electron microscope if it is equipped with necessary tools for the exposition. One of these tools is beam blanker which enables a quick diversion of the electron beam from the exposed area. Exposition itself is process during which the e-beam scans the surface according to prepared matrix and is performed in single point mode, point after point [34], or vector-like.

The high precision of this method is ensured mainly by highly focused electron beam to diameter of few nanometers. Focusing is achieved with applied high voltage in order of tens of electronvolts.

Exposition parameters

The most important exposition parameter is a *dose* Q, which is specified as charge applied to one unit of exposed area. It is in nC/cm for linear objects and in $\mu C/cm^2$ for square objects.

Beam step size d_{bss} specifies the distance between the exposed points (pixels). Next parameter is *beam current* I, its value is predetermined by a type of resist material. There is a danger in application of high currents due to possible resist overheating. However, the current should not be too low because it would lead to prolonging exposition time t_{dwell} and to consecutive charging of the resist which would lead to defocusing. To be specific, t_{dwell} is a time interval during which e-beam stays on one pixel and can be defined as [35]:

$$t_{dwell} = \frac{Q \cdot d_{bss}^2}{0{,}1 \cdot I} \quad (1.5.6)$$

The device can also pose a limitation. In case of usage of high currents, t_{dwell} is so low that the scanning system is not able to shift the beam precisely and in time.

1.5.10. Developing

Resist layer exposition is followed by resist developing. This process is performed with assistance of developer whose suitability is declared by distributor of the used polymer [28]. Suitable developer for PMMA is isopropyl alcohol (IPA) in solution with water or methylisobutylketon (MIBK) [23, 35]. As was mentioned before, the exposed area is developed in case of positive resist and the unexposed are developed in case of negative resist

There are two ways of developing process. The first option is a dry way, when the exposed areas react with highly reactive gas. Etched particles are blown away by plasmatic discharge. This results in wanted profile [37].

Second option is a wet method. The developer is applied on resist layer, which is exposed in certain areas. Developers are mostly organic solvents, their mixtures or solutions with water [38]. Reaction of positive resists with developer is based on faster dissolution and cleaning of exposed areas, where the polymer strings were cut during exposition. The result of developing process is a more or less precise profile of original matrix. Precision of developing process strongly depends on dose and developing time.

The wet developing can be assisted by ultrasound. A beaker with sample and developer is placed to ultrasonic washer, which increases the developing speed and improves resolution and contrast of developed structure.

In case of special self-developed resists, the developing process takes place already during exposition when the reaction is initiated between single parts of polymer resist.

Dissolving speed R of polymer can be determined by formula [37]:

$$R = 1/M^{\alpha} \quad (1.5.6)$$

Where α is constant for given combination of resist and developer and M is a molar weight of polymer molecule.

1.5.11. Resist sensitivity

To determine resist sensitivity, the term relative resist thickness must be established. Relative resist thickness is primarily dependent on exposed dose, type of used developer and length of developing time.

Dependence of relative resist thickness on dose for positive resists can be described from Figure 12.

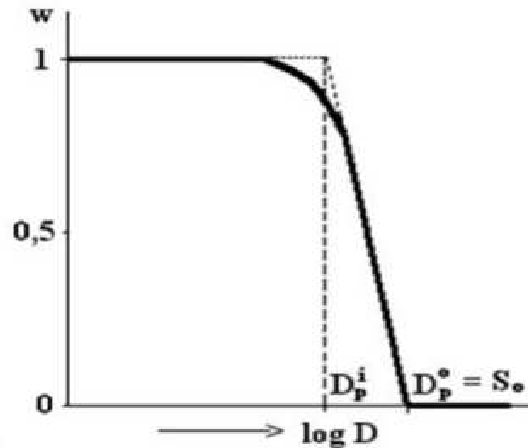

Fig. 12 – Dependence of the relative resist thickness on logarithm of exposition dose for positive resist [22]

The resist is completely inert to influence of the developer until exposition by minimal dose D_p^i. Then the relative resists thickness quickly decreases with increasing exposition dose till D_p^0, when the resist is completely developed. Resist sensitivity can be then concluded as minimal exposition dose, which is capable to initiate complete developing of resist layer in exposed area.

Completely opposite situation is during negative resist developing (see Figure 13). Resist layer is fully developed after exposition by minimum dose D_g^i and with rising dose the relative resist thickness rise as well until the maximum dose D_g^s after which the resist is not possible to developed. With the D_g^s the cross-link reaction takes place and the space net across polymer molecules is created. Point Dg is also called the point of gelation [22]. The median between D_g^i and D_g^0 is called the sensitivity of negative resist.

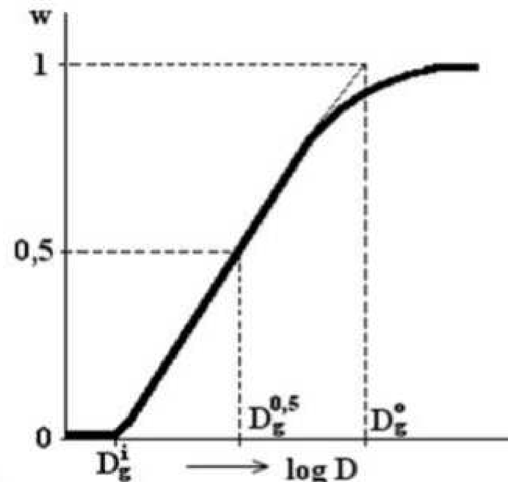

Fig. 13 – Dependence of relative resist thickness on logarithm of exposition dose for negative resist [22]

1.1.1. Active layer deposition

Next step of the EBL process is a deposition of thin active layer [34], which is the vital part, because without this step the prepared mask would lost its purpose.

Adhesion, layer thickness and inner tension of deposited material are the main parameters defining the deposited layer. Another important aspect is homogeneity and continuity of the layer over the polymer resist mask.

The most popular deposition methods are listed below.

Physical Vapor Deposition (PVD)

This method is based on transferring the deposited material in gaseous form to the surface of a sample. Adsorption of the gas takes place on the surface and the intended layer is formed. Sources of the atoms are usually the desired materials, which can be in form of a heated solid or in form of a melt placed in container called a crucible. The heating can be ensured for example by electron beam bombardment or by passing electric current through the material. The system assembly is dependent on the desired parameters of the deposition such as deposition rate, direction of deposited gas flow etc. In case of evaporation, the heated crucible is usually placed at the bottom of a vacuumed chamber and wafers are placed on the ceiling of the chamber.

PVD is primarily used for deposition of conductive materials but insulating materials are also possible to deposit by this method.

If the material is deposited on the surface under particular angle, the effect called shadowing occurs (see Figure 14).

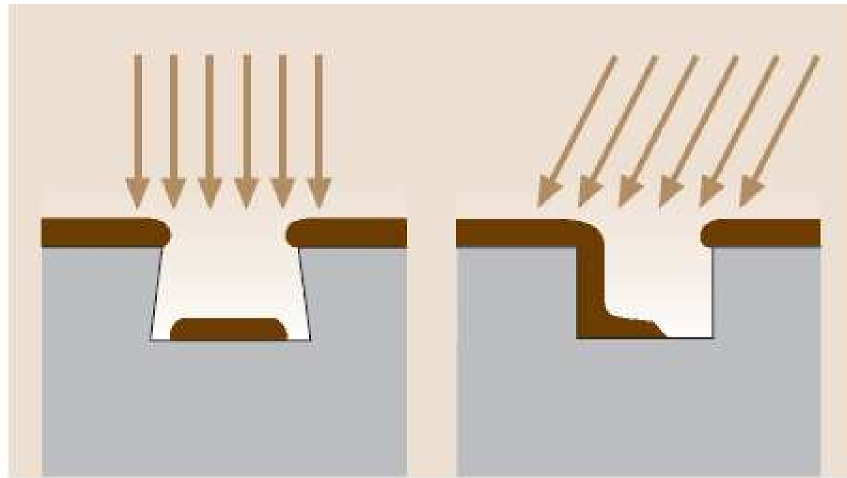

Fig. 14 – Shadowing effect

Chemical vapor deposition (CVD)

CVD is a deposition method which also transfers material in gaseous chemical mixture to the surface of the sample. But in this case a chemical reaction is needed to form an active layer. Undesirable products of the chemical reaction are fumes, which have to be drained from the deposition chamber to maintain very low pressure in the chamber. Very high operating temperatures (550 – 900°C) and low pressure (10-100 Pa) are conditions specific for this method.

Location of areas with deposited layer can be influenced by controlled distribution of catalyst over the surface.

Magnetron Sputtering

During magnetron sputtering, the deposited active layer is formed by atoms and clusters spurted from a target, which is made of wanted material. Particles are spurted by high energy ions which are created by ionization of atoms in work gas (usually inert gas as Ar). Ionization of working gas is ensured by RF or DC plasma. DC is the simplest assembly, when the target is a cathode in diode wiring. RF plasma is ensured by high frequency discharge which is placed under the target and hold by magnetic field. Spurted atoms or clusters travel to the sample surface. The whole process takes place in a high vacuum (units of Pa and less) but coarser than in case of PVD.

This method has no limitations on deposited material so even insulating materials can be deposited. When oxygen is used as working gas, it is possible to perform reactive sputtering during which atoms from the target creates oxide layer on the surface. Simultaneous deposition of different materials from two or more targets is also possible.

1.1.2. FIB GIS

Etching of wafer materials and deposition of active layers can be generally called Focused Ion Beam Lithography (FIBL). Focused ion beam microscope works on the same principle as the SEM but the surface is scanned by beam of heavy ions (usually Ga^{+}) instead of electron beam. The ion beam is also used for etching of material on sample surface with high precision. Theory of interaction of ion beam with sample material and detail description of the etching process are in [43 ,44]
The deposition of active layers is performed by the Gas Injection System (GIS). The deposited material is delivered in the form of precursor to the sample surface through the injection pipes. The precursor is carrying compound and it is fragmented by high energetic beam such as ion beam or e-beam. Closer view can be also taken in [43 ,44]

1.1.3. Lift-off

The final step of e-beam lithography - called lift-off - is a removal of resist mask remaining under the deposited layer. The result is a thin layer of active material deposited in a pattern, which is identical with the intended matrix. This process is also called stripping.

There are two types of lift-off, dry or wet. Which type should be applied is usually determined by resist distributor.

During the wet lift-off, the sample with resists' mask and deposited layer is soaked in remover. Each resist material has list of suitable solvents [22, 23, 35]. Mixtures of these solvents are cold removers, which are substances capable of dissolving and removing the whole resist mask. Lift-off can take place in time intervals from few seconds long to few hours long. To accelerate the lift-off process, an ultrasonic washer is possible to use [23].

Acetone and methyl chloride are some of the suitable removers for PMMA [23, 35].

Dry stripping is mostly used for negative resists. In this case, the sample is put into oxygen plasma, which disintegrates even the cross-linked polymer bonds. These fractured polymer strings of the resist are then removed away by the plasma [22, 24].

1.2. Experimental methods and equipment

1.2.1. Scanning electron microscopy (SEM)

Highly focused electron beam scanning over the sample surface is the basic principle of the scanning electron microscopy [34]. There are three types of electron sources developed. The first one is thermo emission cathode, which is tungsten wire heated on temperatures of 2700 K, when the thermo emission of electrons from tungsten occurs. The second is the Schottky cathode, where the tungsten wire is covered with ZrO to decrease the work function and high voltage filed is applied to initiate Schottky effect. The source is heated only to 1800 K. The last source type is field emission cathode, where the high-voltage field is also applied and the electrons are emitted via tunneling effect.

Emitted electrons are then accelerated to the required energy. This electron beam is focused by system of electromagnetic lenses and apertures. To the most important lenses belong intermodal lens and objective. The scanning movement is secured by scanning coils, as is also shown in Figure 15.

The scanning electron beam interacts with the sample's surface which leads to the emission of various types of particles. Primary electrons of electron beam have energy in range of ones to tens of keV. Interactions of primary electrons with the material leads to ionization or excitation of atoms in the sample, which can cause for example emission of Auger electrons from surface layer few nanometers thick. Their detection requires ultra-high vacuum. Other particles emitted as consequence of aforementioned interactions are secondary electrons (SE). These electrons travel from surface layer about 10 nm thick and their energy is in range of ones to tens of eV. Detection of SE is secured by scintillator detector. Other primary electrons are electrons backscattered on heavy nuclei (BSE). These interactions are elastic so BSE suffer minimal energetic loss. Detection of these electrons also takes place on scintillator detector but with negative potential on the first grid, which serves as shielding feature for SE with low energy. Last source of information from the sample is characteristic X-ray, which is formed during deexcitations of excited atoms and it

is detected by the semiconductor (SiLi) detectors designated for energy-dispersive X-ray spectroscopy EDX.

Resolution is problematic issue for insulating materials because of the charging of the surface. For conducting samples this is not an issue and resolution depends only on the diameter of the beam.

Contrast from SE detection is primarily morphologic but can be even material. Better material contrast is from BSE detection because of larger sensitivity of BSE to nucleus number.

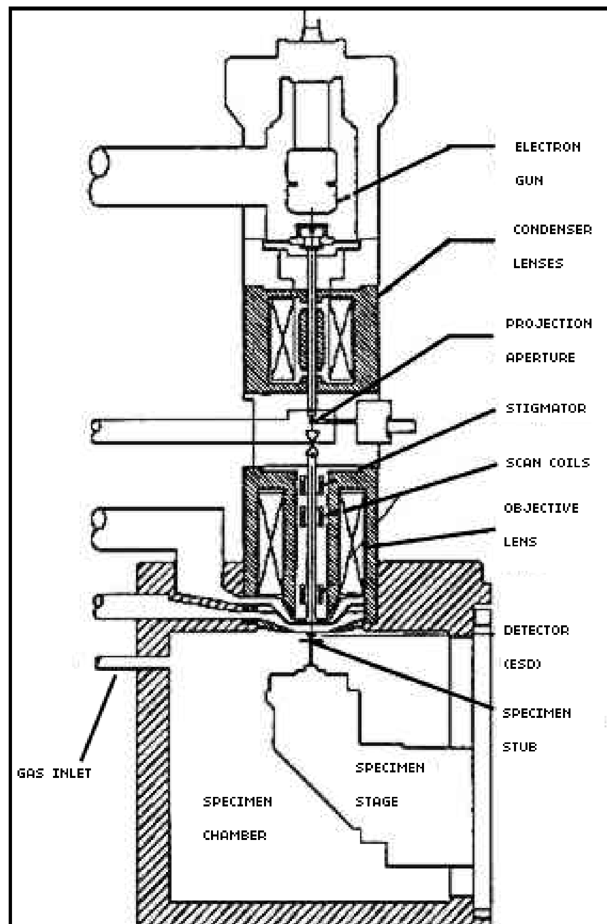

Fig. 15 – Assembly of Scanning electron microscope

SEM used in this work is type MIRA III from Tescan. Schottky cathode is used as electron source. EDX detector AXS Xflash detector 4010 from Bruker is also part of the assembly. This SEM can also be used as lithograph due to the added beam blanker and software extension of DrawBeam, the lithographic modul.

1.2.2. AFM

Principle of Atomic Force Microscopy is based on a tip scanning the surface of the sample [41,42]. The tip is usually few micrometers long and 10nm thick and it is placed on the lose end of a cantilever, which is 100 – 200 um long. The tip is deflected in dependence on the type and magnitude of the forces acting between atoms on the tip and atoms at the surface (see Figure 16). The first type of interaction is attractive force, which is usually Van der Waals force and which acts when the tip is approaching the surface. At some point of the approach the potential in Figure16 reach the minimum and the repulsive forces start to act. These forces are based on the Pauli's exclusion principle when the orbital from tip's atom overlay the orbital of surface atom. The tip's deviations are tracked during the scanning by laser beam, which lands on the cantilever and it is reflected to photodetector. This photodetector is divided to two or four segments and position of the beam is determined by potential difference between segments. Measured values enable the computer to generate the surface map. The AFM can measure all types of materials, conductors, semi-conductors and insulators.

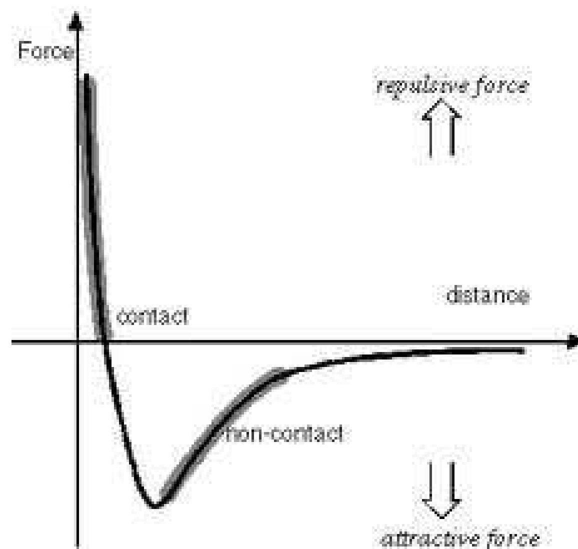

Fig. 16 – Interaction between tip and sample

There are two types of measuring modes depicted in the Figure 16. The first is called contact mode or repulsive mode because the forces acting at this mode are mainly repulsive. The tip has light physical contact with the surface. The tip is placed on cantilever with low stiffness. The forces force the tip accommodate on the profile

of the surface during soft scanning of the tip over the sample. Scanning is performed in mode of constant height or constant force.

The second mode is non-contact mode, when the system is exciting the cantilever to frequency near to its resonant frequency with amplitude even few tents of nanometers. The changes in the frequency or in the amplitude are detected as consequence of the force interaction.

The last measuring mode is the semi-contact or tapping mode. This mode is very similar to non-contact mode. The main difference is in a distance of the tip from the sample. In this case the tip is significantly closer to the surface and is 'hitting' it. The changes in frequency are also tracked and the signal is digitaly transformed to surface relief.

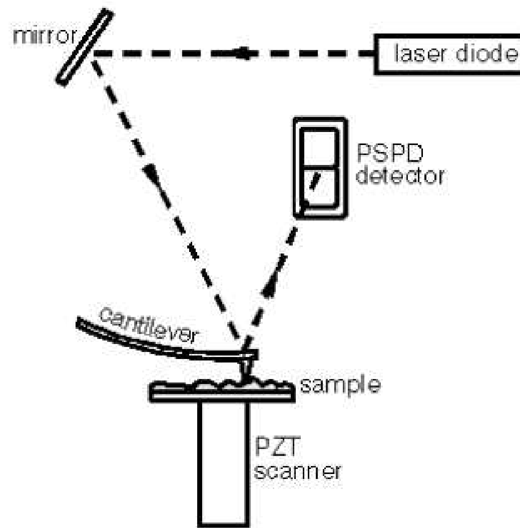

Fig. 17 – The assembly of Atomic Force Misroscopy

The type of used AFM is Veeco Multimode V with scanner JV. Pictures are taken in tapping mode with FESP tips from Bruker. The tips resonance frequency is in range 50 – 100 kHz. Error of height measurement is listed as 10%.

2. Experiment

Chips with 3D topography were fabricated commercially. Micro-channels were prepared as micro-channels of micro-DMFC in Figure 5. The DRIE etching was processed through a lithographic mask after a photolithography procedure. The final profile is shown in Figure 18. Optimization of PMMA resist layer deposition was performed and for resist layer of chosen parameters the EBL process was tested on plain wafer. Parameters chosen on the basis of testing on the plain wafer were then applied for the EBL process on structured surface. With additional modifications three following EBL processes were performed. The aim of the first process was the deposition of Au contacts, the aim of the second process was application of Pt catalytic layer to the cathode channel and the aim of the third was to ensure deposition CN_x/CeO_x layer into the anode channel.

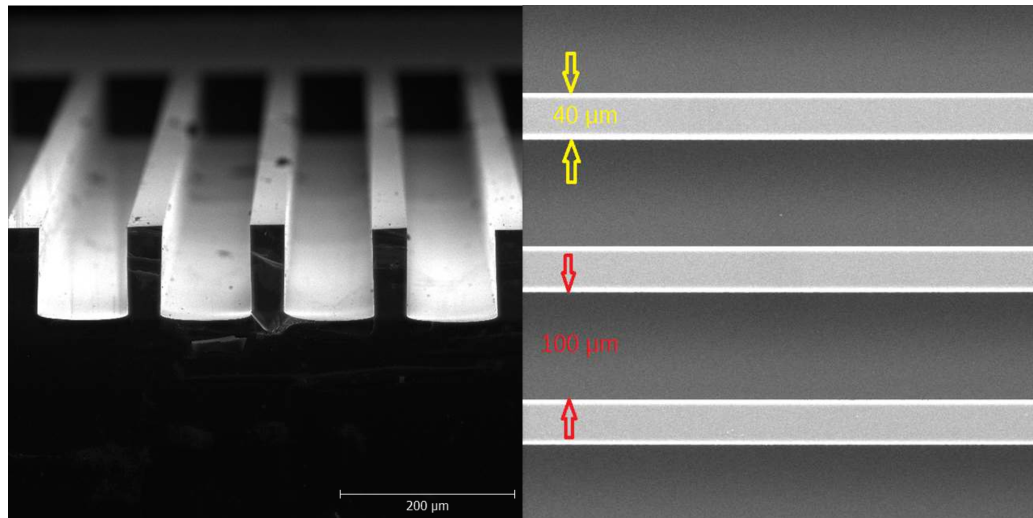

Fig. 18 – Fabricated channels, cross-section on the left side, top view on the right side

2.1. Optimization of sprayed resist layer on 3D topography

To find the optimal parameters for sprayed resist layer, six resist solutions were prepared, which included 1%, 3%, 5% mass concertation solutions of 120 000 g/mol (120K) PMMA with anisole and the same three concentrations of 996 000 g/mol (996K) PMMA with anisole. Preparation of the solutions consisted of blending the mixtures of polymers and anisole for 60 minutes at 60°C.

Optimization process continued with distribution of resist solutions over structured substrate by spray coating system of our own design (see Figure 19). This assembly contained Double Action Airbrush Fengda BD-132 with nozzle diameter 0.2 mm and classic spin coater. The sprayed aerosol current was carried by nitrogen flow under pressure of 1 bar and the spraying rate was controlled by movement of 0.2 mm thick needle in the nozzle. The airbrush was fixed six centimeters over the sample. This distance was established to optimize the diameter of sprayed area.

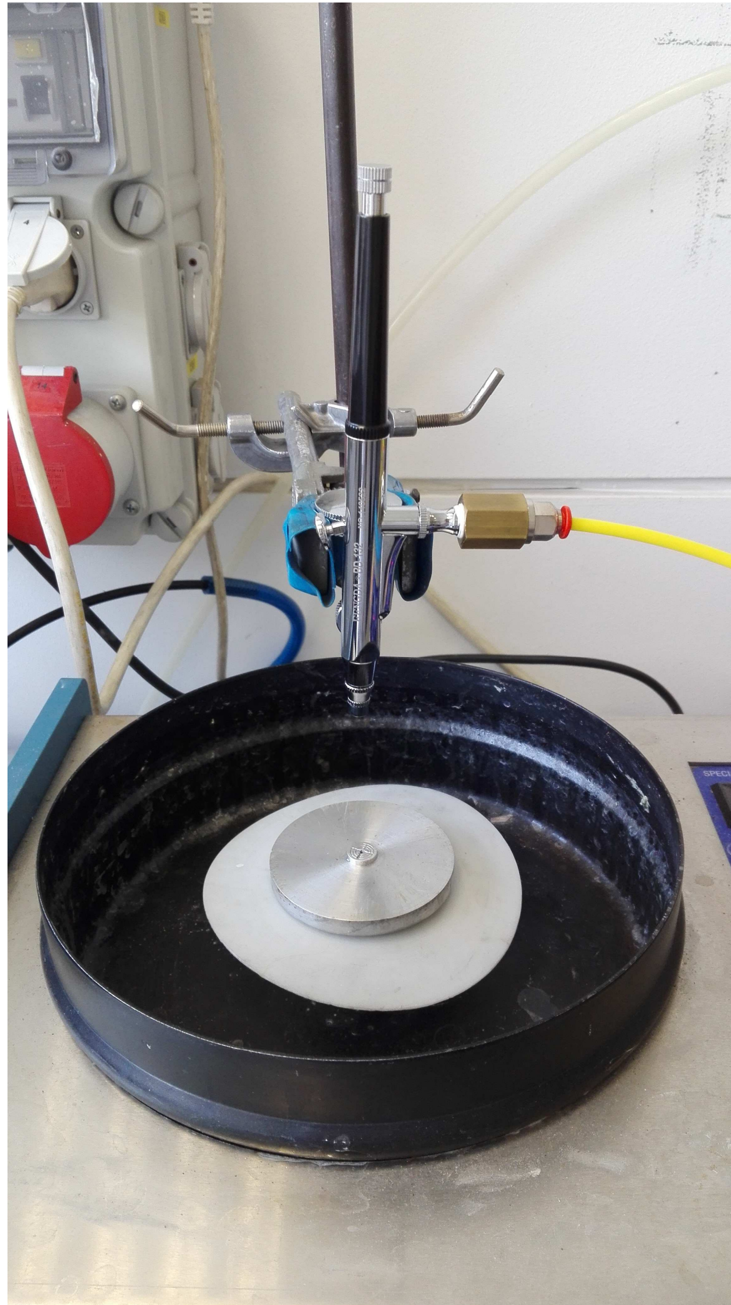

Fig.19 – Spray coater of our own design

Resists were sprayed on heated structured wafers which were cleaned before the deposition by nitrogen blow for 15 seconds. Spraying ran for 60 seconds after which the sample was still rotating for 30 s to ensure better accommodation of the resist layer on the Si surface. Exact spraying rate was unfortunately unknown, but maximum effort was paid to keep the rate constant for all samples. Middle current setting was used for all depositions. Spraying of each resist solution was performed for sample spinning speeds: 100, 300, 500 and 700 rotations per minute (rpm).

The AFM was the method used to determine the resist thickness during my previous studies. In this work, however, it was impossible to measure resist thickness on the walls of the channels with AFM. The resist thickness was thus established from SEM pictures. Results of the measured resist layers for all combinations of solutions of and sample spinning speed during the spray coating are in the Figures 20-43.

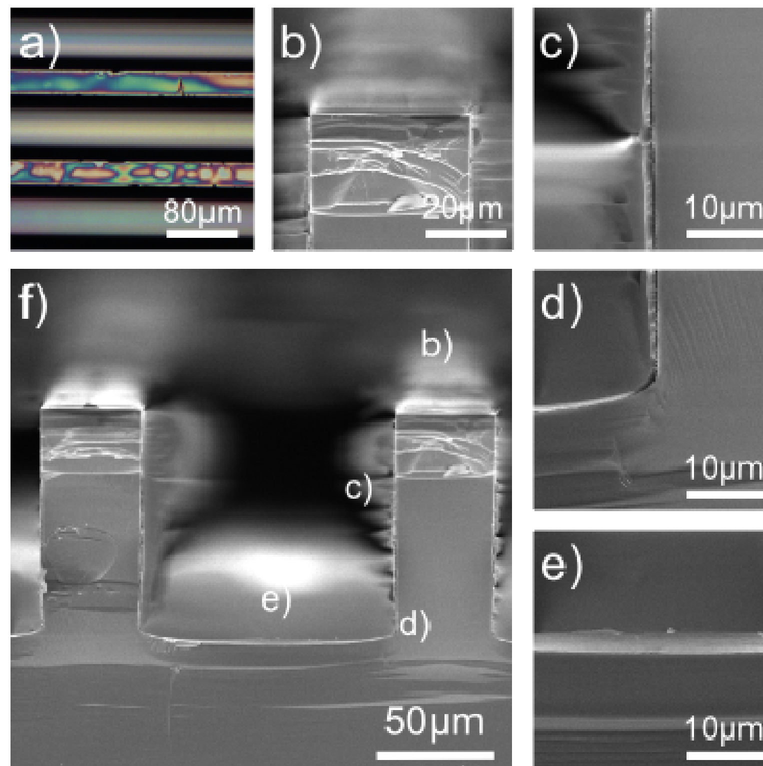

Fig. 20 – Resist layer 996 K 1%, Anisole, 700 rpm, picture a) is a top-view from optical microscope; b), c), d), e) are details the of picture f)

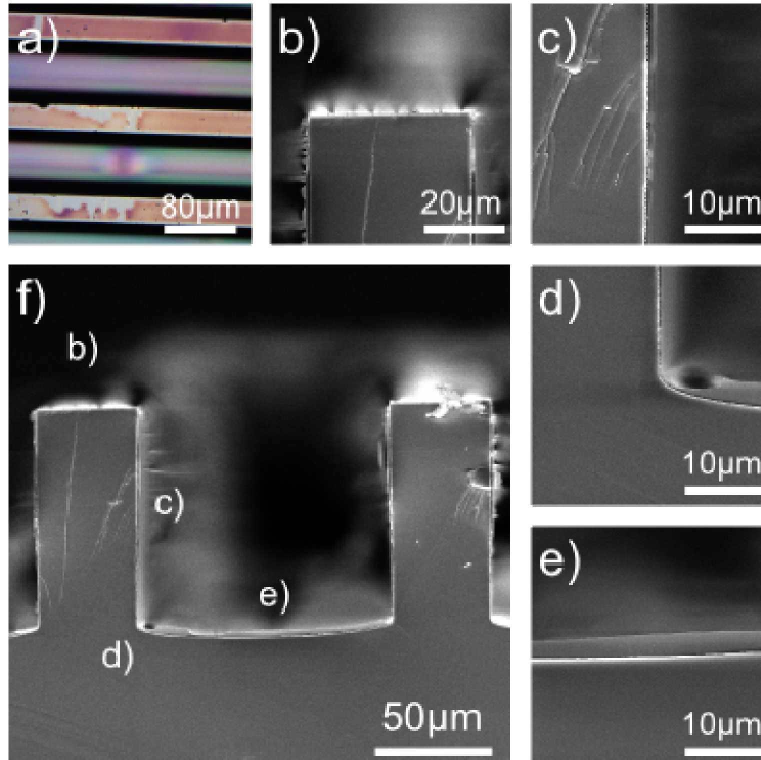

Fig. 21 – Resist layer 996 K 1%, Anisole, 500 rpm, picture a) is a top-view from optical microscope; b), c), d), e) are details of the picture f)

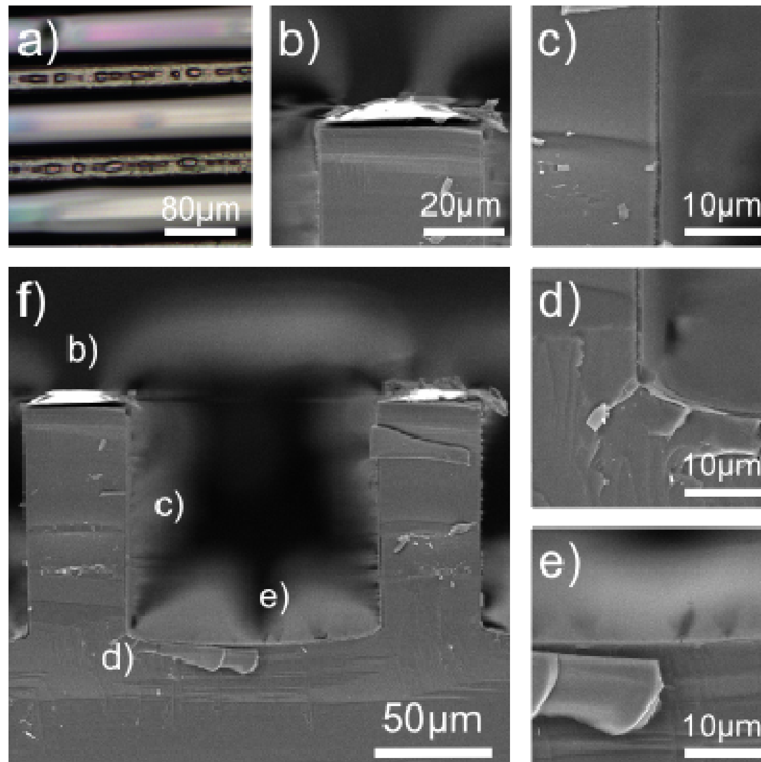

Fig. 22 – Resist layer 996 K 1%, Anisole, 300 rpm, picture a) is a top-view from optical microscope; b), c), d), e) are details of the picture f)

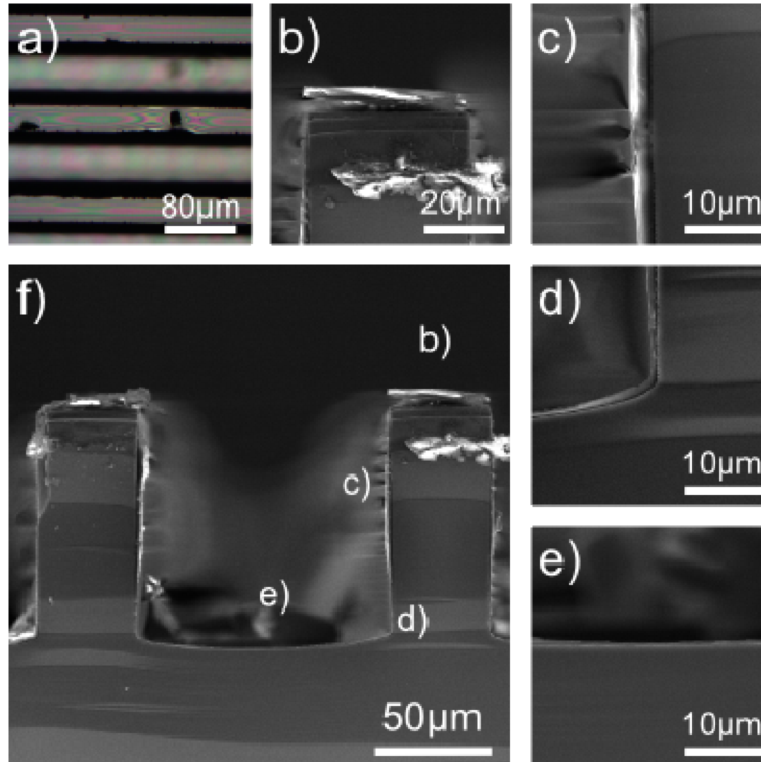

Fig. 23 – Resist layer 996 K 1%, Anisole, 100 rpm, picture a) is a top-view from optical microscope; b), c), d), e) are details of the picture f)

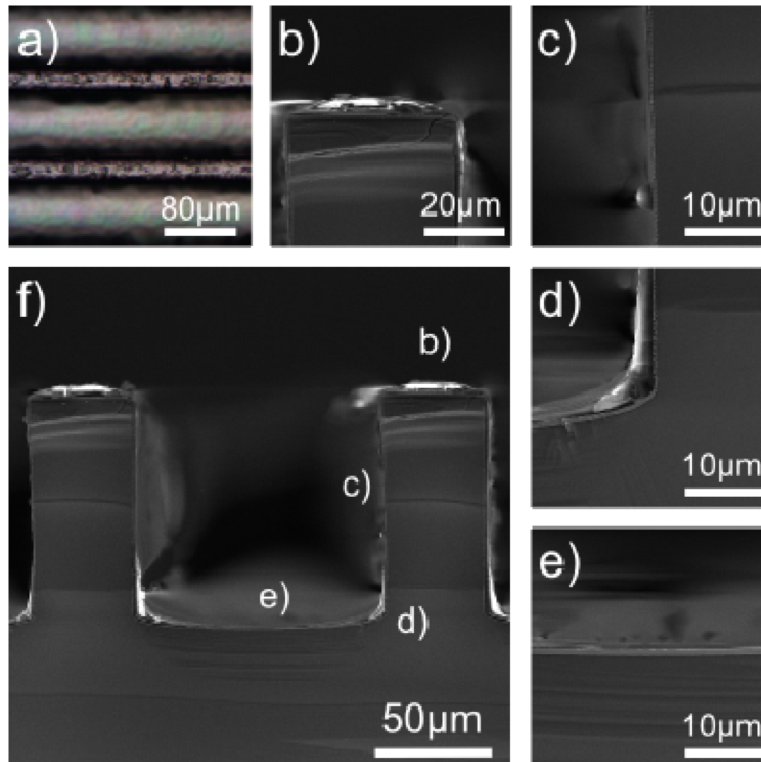

Fig. 24 – Resist layer 996 K 3%, Anisole, 700 rpm, picture a) is a top-view from optical microscope; b), c), d), e) are details of the picture f)

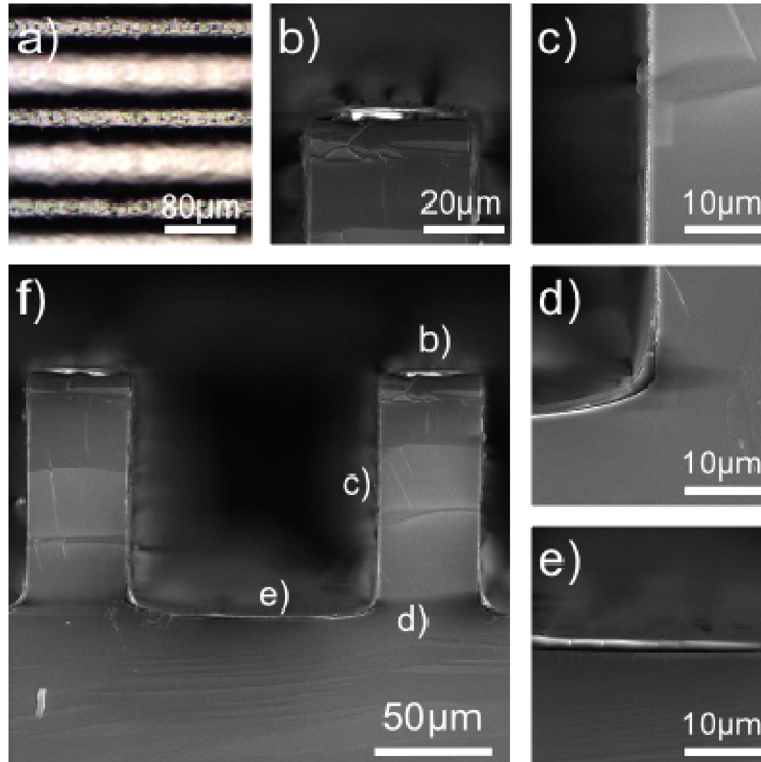

Fig. 25 – Resist layer 996 K 3%, Anisole, 500 rpm, picture a) is a top-view from optical microscope; b), c), d), e) are details of the picture f)

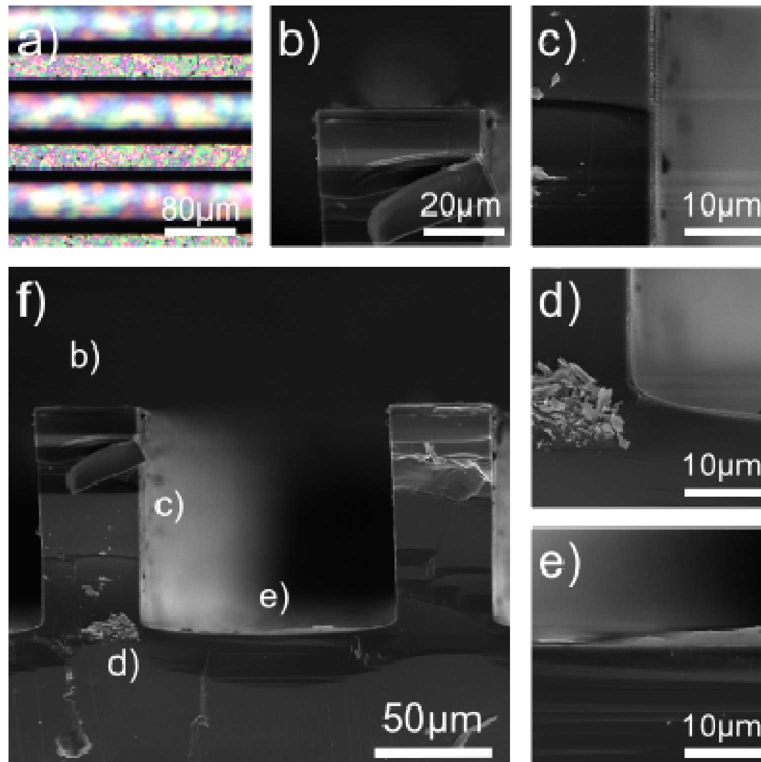

Fig. 26 – Resist layer 996 K 3%, Anisole, 300 rpm, picture a) is a top-view from optical microscope; b), c), d), e) are details of the picture f)

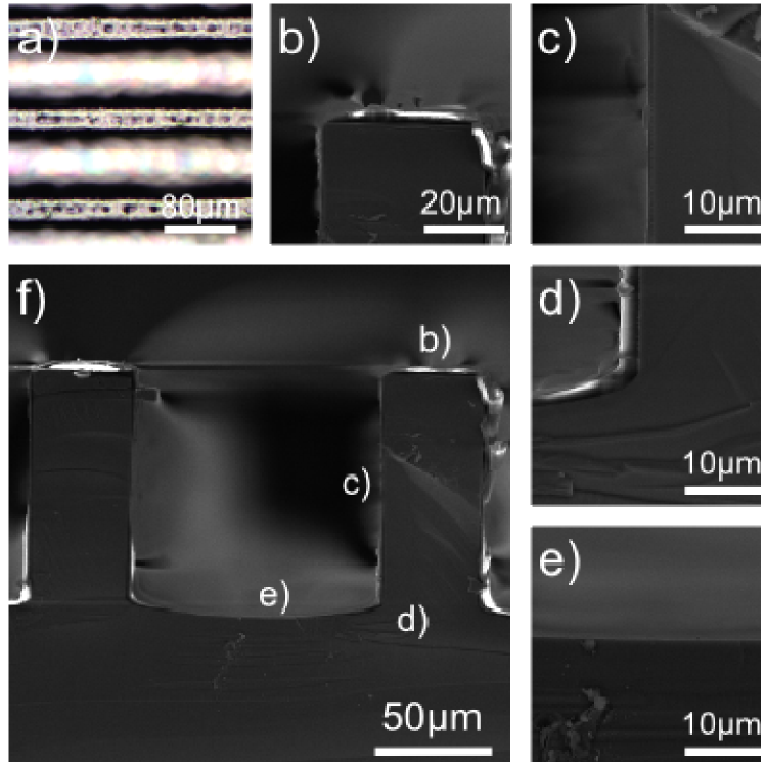

Fig. 27 – Resist layer 996 K 3%, Anisole, 100 rpm, picture a) is a top-view from optical microscope; b), c), d), e) are details of the picture f)

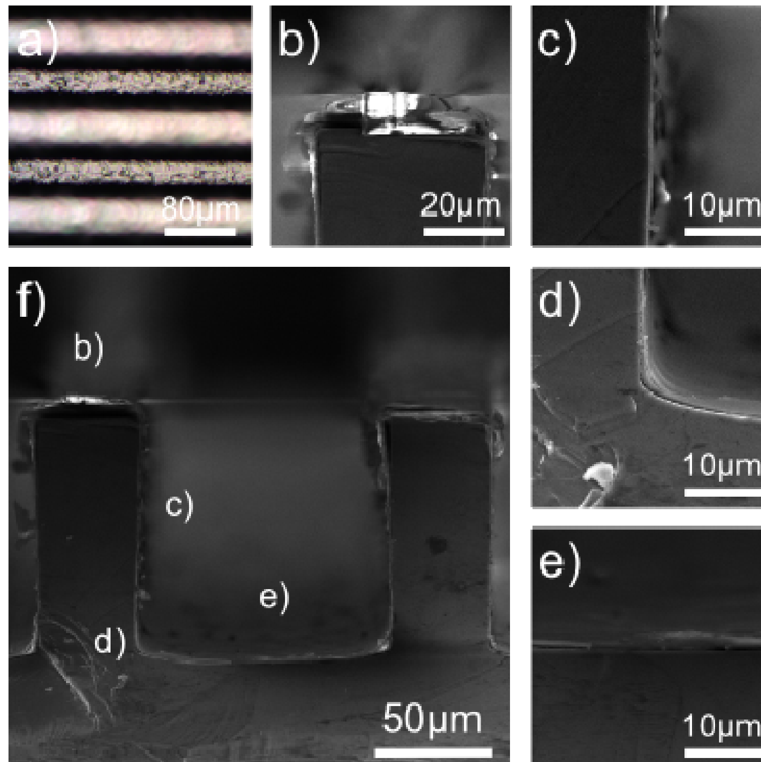

Fig. 28– Resist layer 996 K 5%, Anisole, 700 rpm, picture a) is a top-view from optical microscope; b), c), d), e) are details of the picture f)

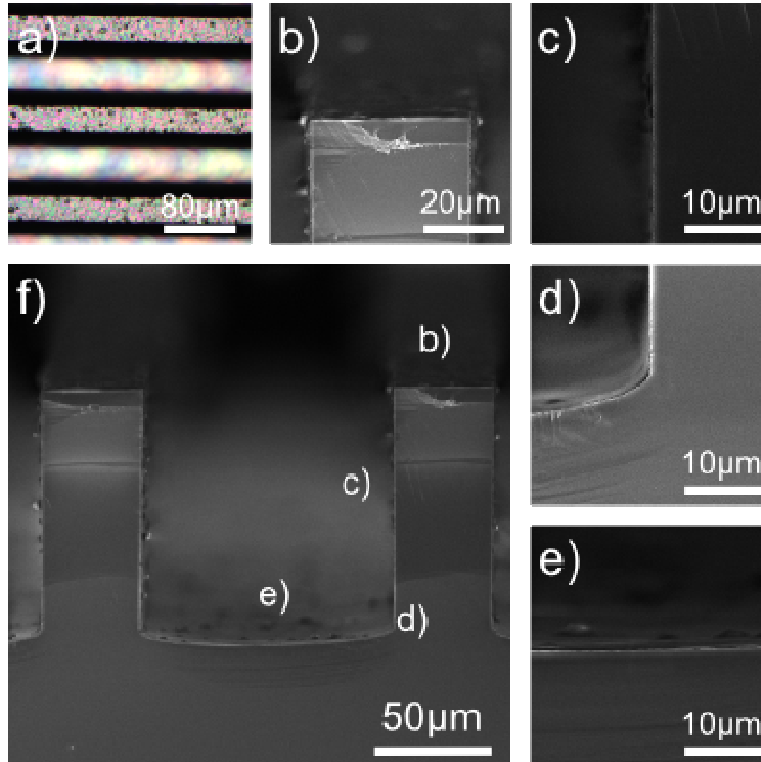

Fig. 29 – Resist layer 996 K 5%, Anisole, 500 rpm, picture a) is a top-view from optical microscope; b), c), d), e) are details of the picture f)

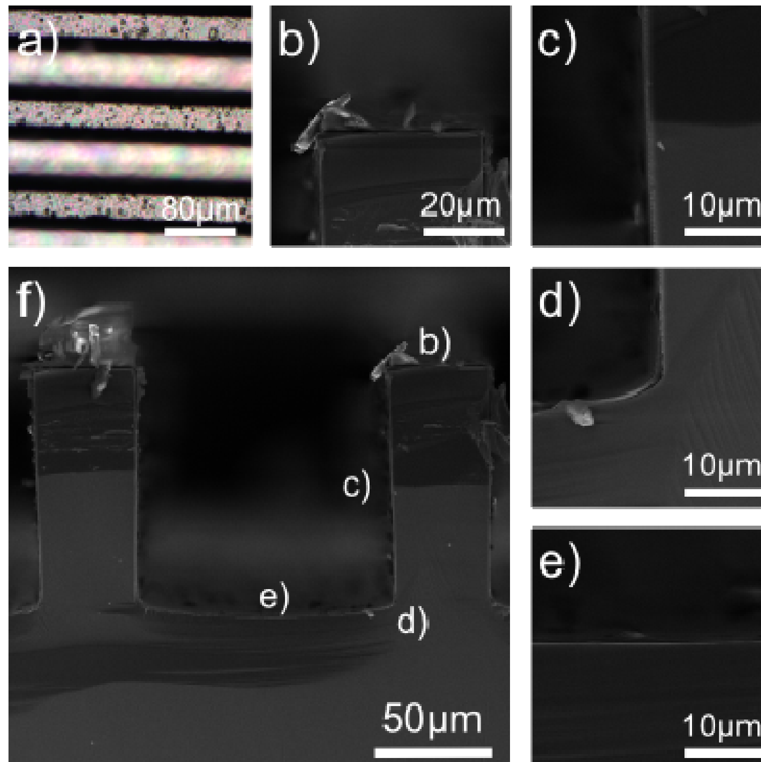

Fig. 30 – Resist layer 996 K 5%, Anisole, 300 rpm, picture a) is a top-view from optical microscope; b), c), d), e) are details of the picture f)

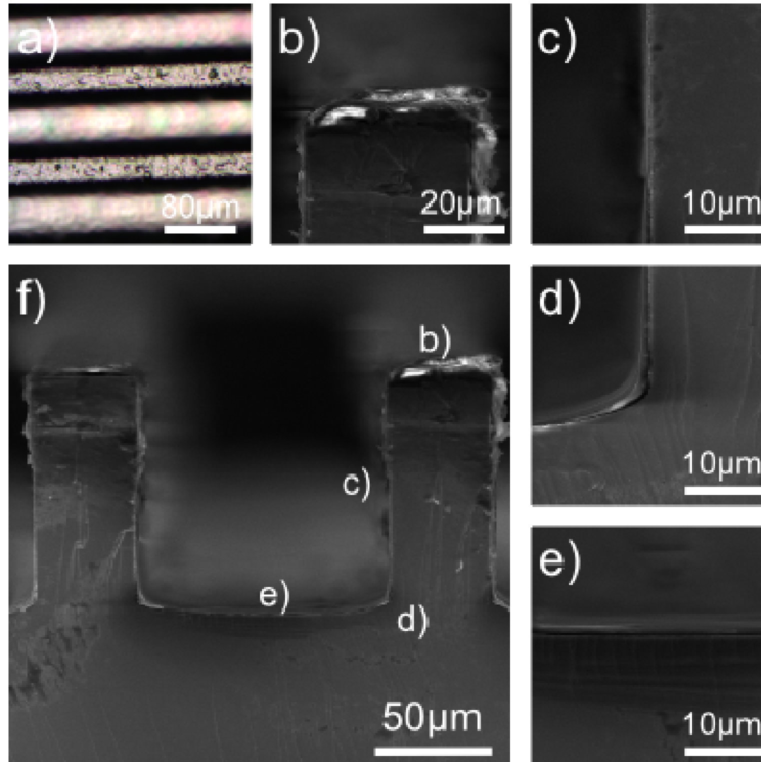

Fig. 31 – Resist layer 996 K 5%, Anisole, 100 rpm, picture a) is a top-view from optical microscope; b), c), d), e) are details of the picture f)

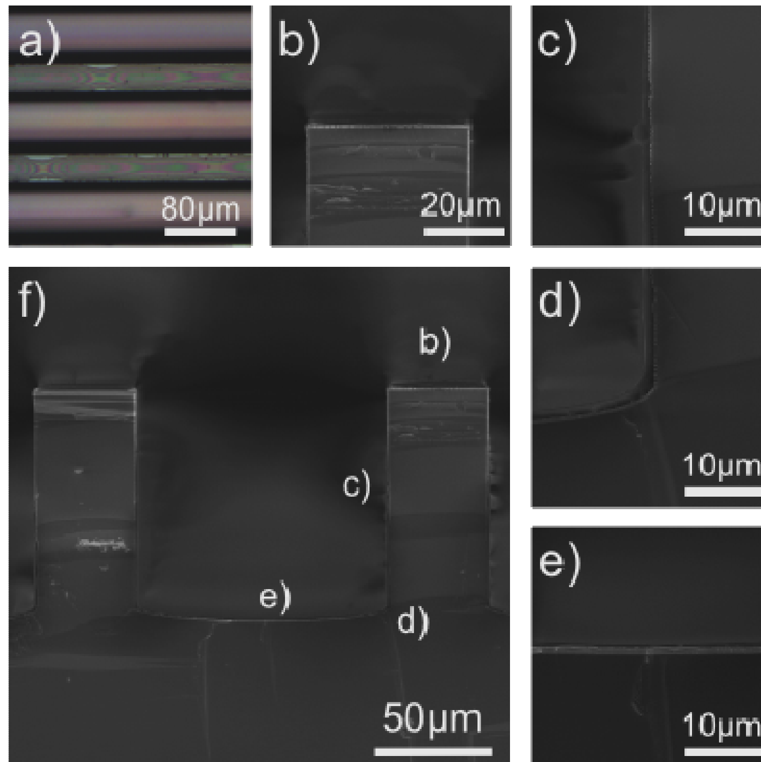

Fig. 32 – Resist layer 120 K 1%, Anisole, 700 rpm, picture a) is a top-view from optical microscope; b), c), d), e) are details of the picture f)

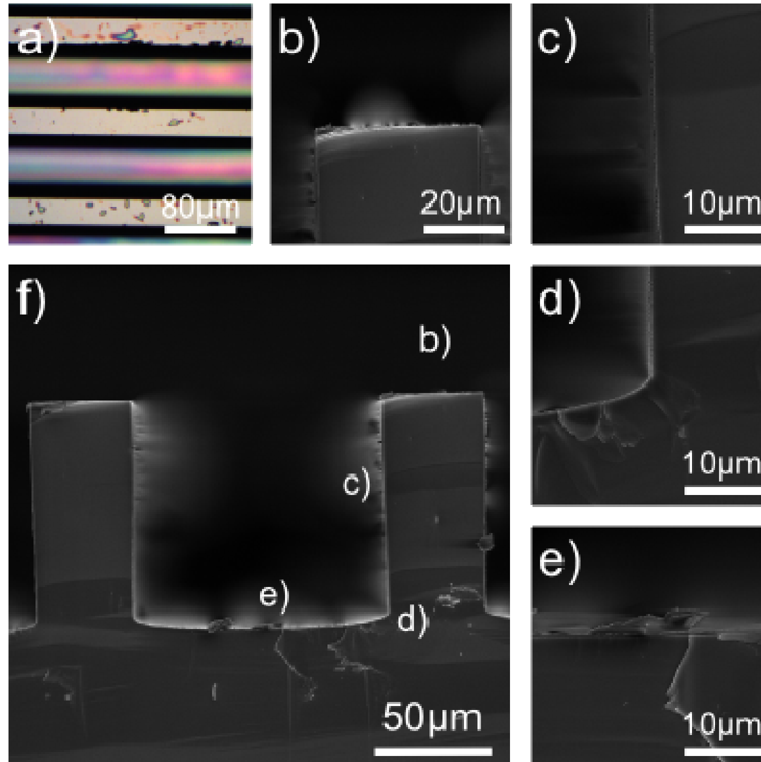

Fig. 33 – Resist layer 120 K 1%, Anisole, 500 rpm, picture a) is a top-view from optical microscope; b), c), d), e) are details of the picture f)

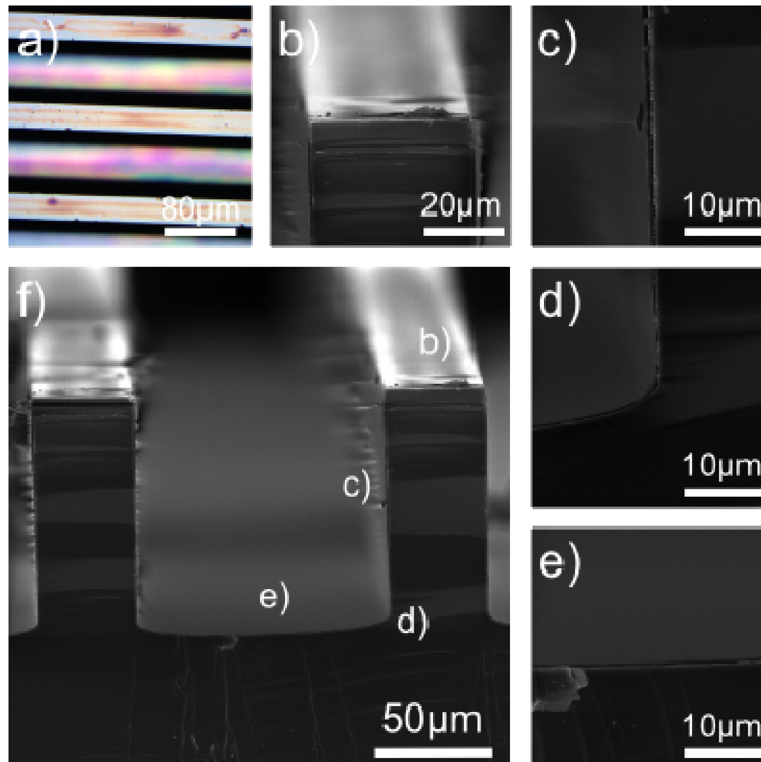

Fig. 34 – Resist layer 120 K 1%, Anisole, 300 rpm, picture a) is a top-view from optical microscope; b), c), d), e) are details of the picture f)

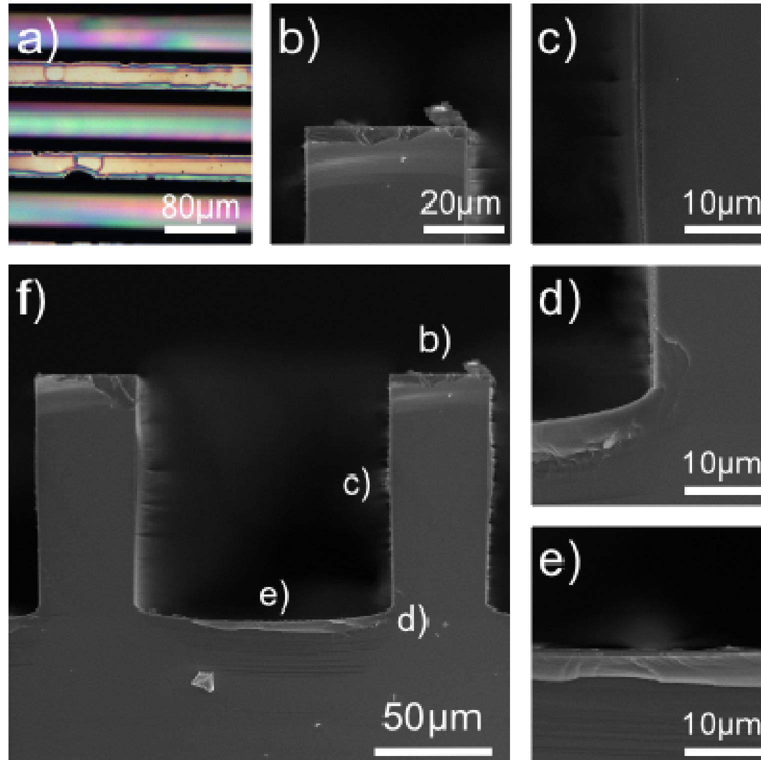

Fig. 35 – Resist layer 120 K 1%, Anisole, 100 rpm, picture a) is a top-view from optical microscope; b), c), d), e) are details of the picture f)

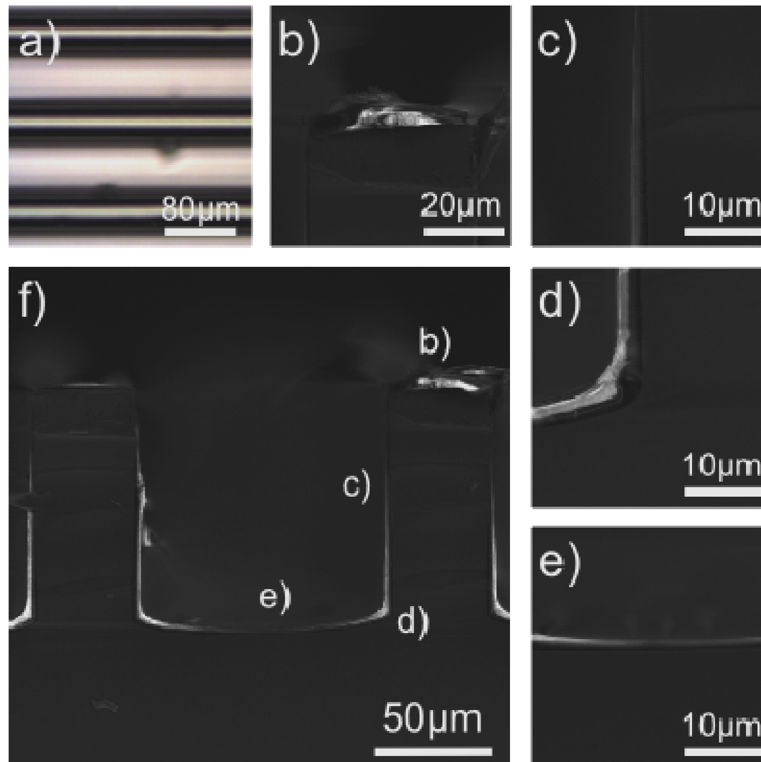

Fig. 36 – Resist layer 120 K 3%, Anisole, 700 rpm, picture a) is a top-view from optical microscope; b), c), d), e) are details of the picture f)

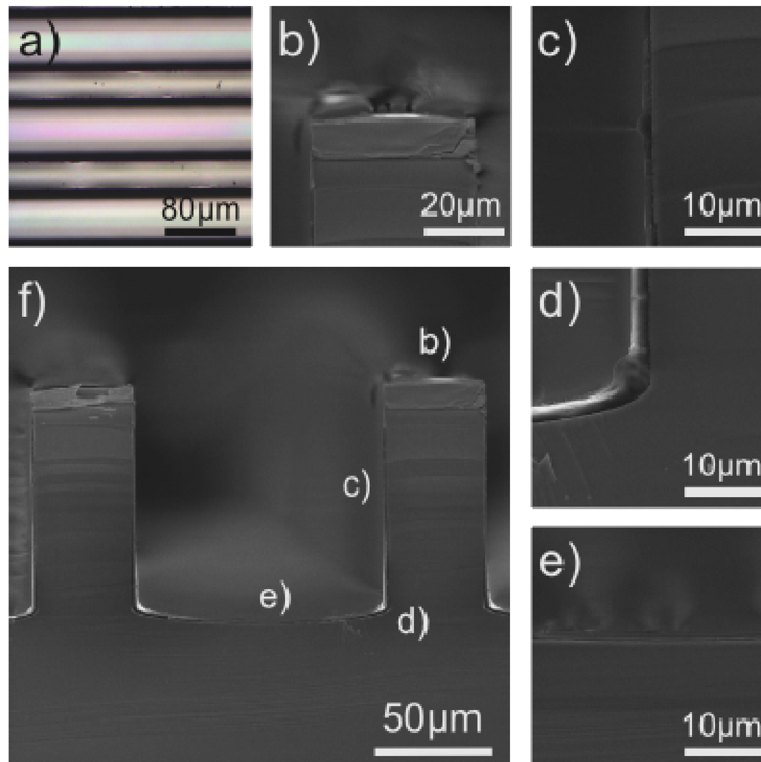

Fig. 37 – Resist layer 120 K 3%, Anisole, 500 rpm, picture a) is a top-view from optical microscope; b), c), d), e) are details of the picture f)

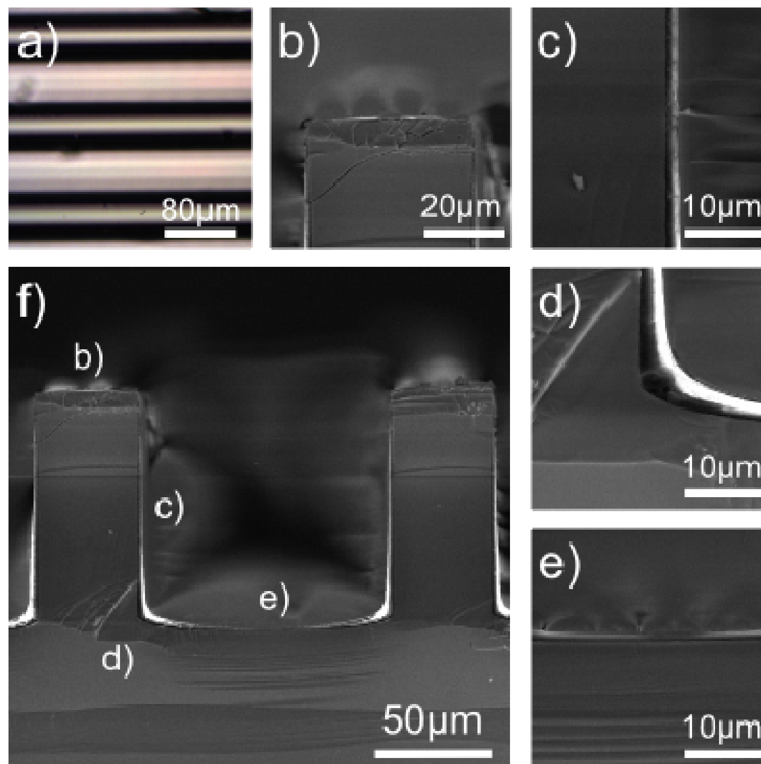

Fig. 38 – Resist layer 120 K 3%, Anisole, 300 rpm, picture a) is a top-view from optical microscope; b), c), d), e) are details of the picture f)

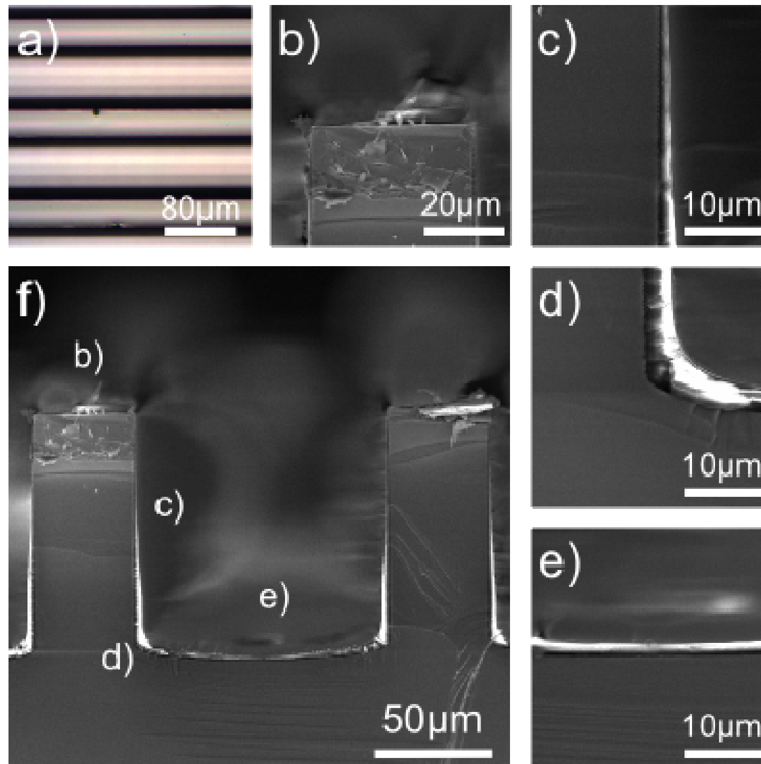

Fig. 39 – Resist layer 120 K 3%, Anisole, 100 rpm, picture a) is a top-view from optical microscope; b), c), d), e) are details of the picture f)

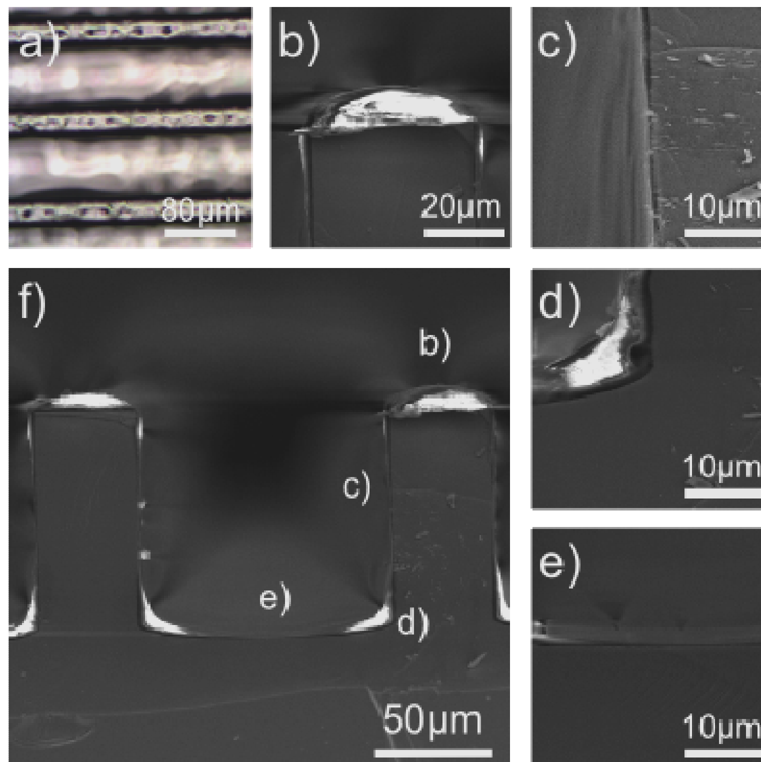

Fig. 40 – Resist layer 120 K 5%, Anisole, 700 rpm, picture a) is a top-view from optical microscope; b), c), d), e) are details of the picture f)

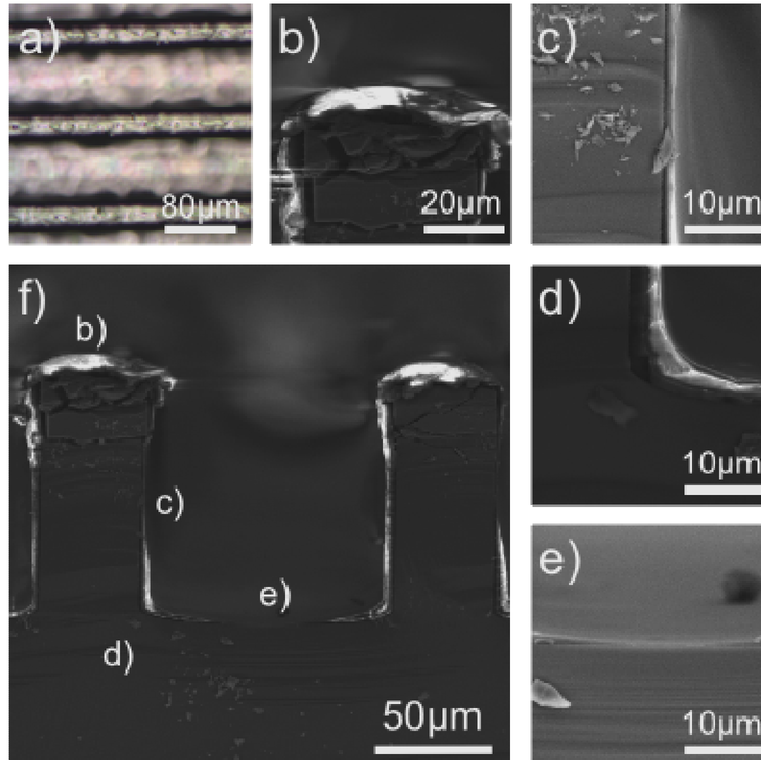

Fig. 41 – Resist layer 120 K 5%, Anisole, 500 rpm, picture a) is a top-view from optical microscope; b), c), d), e) are details of the picture f)

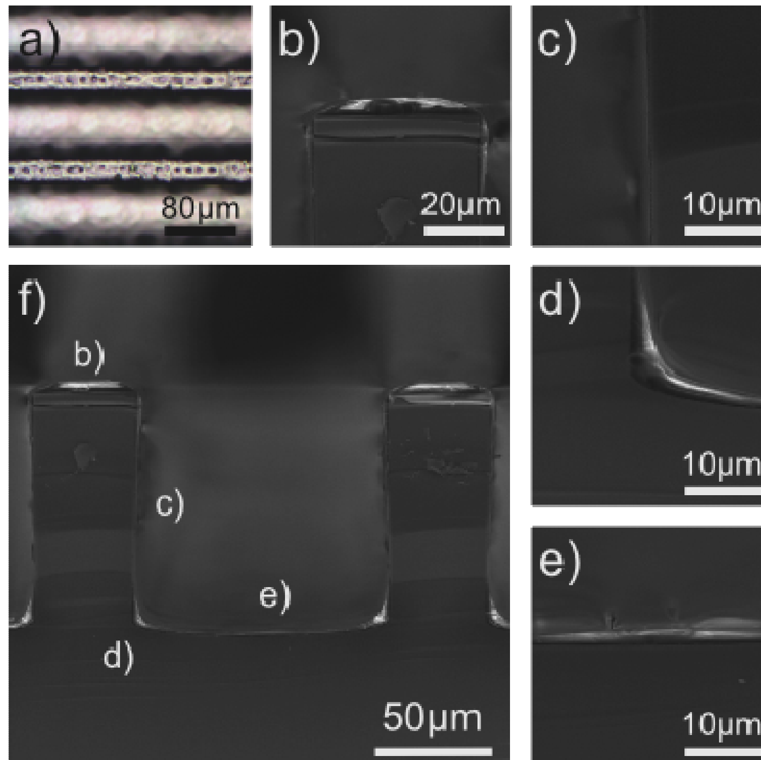

Fig. 42 – Resist layer 120 K 5%, Anisole, 300 rpm, picture a) is a top-view from optical microscope; b), c), d), e) are details of the picture f)

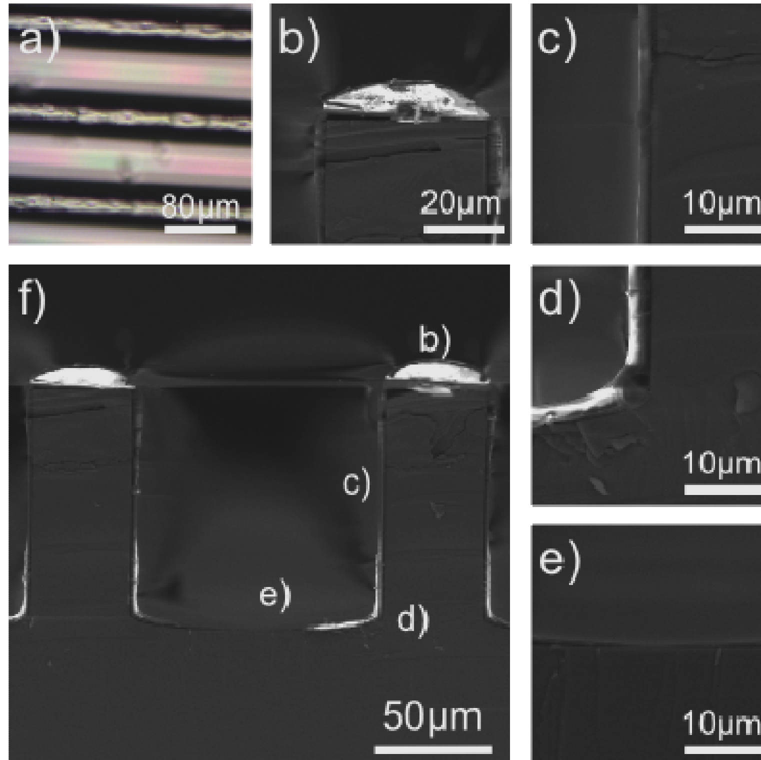

Fig. 43 – Resist layer 120 K 5%, Anisole, 100 rpm, picture a) is a top-view from optical microscope; b), c), d), e) are details of the picture f)

The behavior of the resist material on 3D topography during spin-coating is influenced by centrifugal forces, which together with the gravity force press the resist to flow to the edges, where it is pushed away when the surface tension forces are exceeded. This effect should be increasing with increasing spin speed in case of constant concentration and molecular weight of the resist solution. This effect should be less prominent for resists of higher concentration, in other words with higher viscosity. We expect similar behavior of the resist layers applied by our alternative spray coating method.

We can divide the results into two main groups according to molar weight of used polymer materials. First we will discuss the results obtained for (996 g/mol) PMMA.

Resist layers in Figures 20-23 were of the same concentration - 1% of 996K - and were sprayed at 4 different sample spin speeds. They follow the expected behavior that with higher spin speed the resist's thickness decreases on top of the channel and increases at the bottom and in the corners of the channel.

Situation is however quite different for layers of constant concentration of 3% 996K (see Figures 24-27). Resist layers are of comparable quality for all sample spin

speeds so the spin speed dependence is not noticeable at all. Moreover the resist layer sprayed at 300 rpm seems to fail completely as no resist material seems to be spread on the sample at all.

Similar behavior is observable in case of 5% 996K in pictures 28-30. All resist layers are similar and no dependence of the thickness of the resist layer on the sample spin speed is noticeable.

The results also show the following dependency of the resist layer quality on concentration of the resist solution for constant spin speed: For the sample spin speed 700 rpm the expected dependency is observable on top layers. The lower the concentration of the resist is the thinner the resist layer gets.

Layers sprayed at 500 rpm spin speed fulfill the expected behavior only for concentrations of 1% and 3%.

Resist layers deposited at the 300 rpm spin speed do not seem to show any dependence of the thickness of the resist layer on the concentration. It should be noted again that for this spin speed the experiment executed for 3% failed.

The spray coating at 100 rpm has the same impact on layers as at 500 rpm.

On the basis of these results we came to a general conclusion that the 5% 996 K layers do not obey the expected behavior of the resist layers due to high viscosity of the solution of the resist material.

An observation of the second group of molar weight of polymer starts with comments on 120K 1% resist layer.

The resist layers in Fig. 31-34 are getting thinner with the faster spinning except for the resist coated at 700 rpm.

The 120 K 3% resist pictured in Fig. 35-39 is basically following the expected pattern of behavior except the bit thicker 700 rpm layer. In case of 120 K 5% the layer is coated as expected, Fig 40-43.

All resist layers of 120 K for all resist concentrations perfectly follows expected behavior for increasing spin speed.

Despite the maximum effort invested to keep the spraying rate constant, deviations in the rate could have occur which could lead to lack of deposited material or its excess. That could possibly explain the situation when the layers were thinner or thicker than expected. Another possible explanation is that the temperature of the structured substrate during the spray-coating was different for different samples. The

time interval between heating the sample on the hot plate and resist application was possibly not equally long for all samples.

Differences in homogeneity and continuity between 996 K and 120 K resists are probably consequence of different molecular weight. Dissolving rate for polymers with higher molecular weight is lower according to formula $1/M^{\alpha}$ [22], where alpha is equal for both polymers. This fact is probably the reason for the presence of the longer polymer strings in 996 K resist than in 120K, which leads to forming of larger droplets during spraying of 996 K and leads to higher roughness of the resist layer.

Due to requirements on the sufficient continuity of the resist layer, the 996 K was considered unsuitable for EBL process for application in this work. Another required property of resist layer is the maximal uniformity of resist thickness as possible and satisfying coverage of right angled edges. The reasons for those requirements are the significant problems during exposition of resist layer with inhomogeneous thickness. Another special requirement is on the thickness of the resist layer. For the lift-off to be successful, the resist layer has to be at least double the size of the deposited layer.

The uniformity is established from measured thicknesses of resist in three channels (1, 2 and 3) on every sample coated with 120K (Table. 2) according to formula [30]:

$$Uniformity = \frac{\sigma}{d} \cdot 100\% \, , \qquad (2.1.1)$$

where d is the average thickness of the layer and σ is the standard deviation of the average value.

It is also observable from the table 2, that with higher spin speed, the resist material vanishes from the walls, upper edges and bottoms and stays on tops or is pushed to bottom corners as the stronger centrifugal force engages.

Concentration	1%				3%				5%			
Spin speed[krpm]	0,1	0,3	0,5	0,7	0,1	0,3	0,5	0,7	0,1	0,3	0,5	0,7
Top1[μm]	0,0	0,0	0,0	0,6	1,0	0,7	1,7	4,5	7,5	3,3	9,2	9,6
Top2[μm]	0,0	0,0	-	-	0,9	1,4	1,7	3,7	7,3	6,0	10,9	5,9
Top3[μm]	0,0	0,0	-	-	0,9	2,3	2,0	3,2	6,9	4,0	9,7	8,7
Upperedge1[μm]	0,0	0,0	0,0	0,1	0,0	0,0	0,0	0,5	2,5	2,7	1,2	1,2
Upperedge2[μm]	0,0	0,0	-	-	0,0	0,0	0,0	0,5	2,6	1,0	1,4	0,5

Upperedge3[µm]	0,0	0,0	-	-	0,0	0,0	0,0	0,0	2,1	0,6	5,1	2,7
Wall1[µm]	0,7	0,8	0,2	1,0	1,5	1,2	0,9	1,6	1,6	0,8	2,7	0,8
Wall2[µm]	0,6	0,6	-	-	1,6	1,6	0,5	1,6	0,8	0,3	1,4	0,6
Wall3[µm]	0,4	-	-	-	1,6	2,7	0,7	1,0	1,5	0,4	1,2	0,3
Downcorner1[µm]	0,0	0,4	0,0	1,7	5,4	4,9	3,1	4,7	3,9	6,9	7,3	7,3
Downcorner2[µm]	1,3	-	-		3,5	6,9	3,9	5,7	3,9	6,1	4,6	7,6
Downcorner3[µm]	-	-	-		5,2	-	3,9	5,2	4,2	6,0	5,7	6,6
Bottom1[µm]	0,2	0,4	0,3	0,5	1,5	1,5	0,6	1,0	0,5	1,7	0,3	0,5
Bottom2[µm]	0,2	0,3	-	-	1,7	1,0	0,3	1,3	0,6	1,6	0,3	0,6
Bottom3[µm]	0,1	-	-	-	1,5	1,7	0,5	1,1	0,4	2,0	0,4	0,6
Average[µm]	0,3	0,2	0,1	0,8	1,8	1,7	1,3	2,4	3,1	2,9	4,1	3,6
Uniformity	147,9	121,7	126,5	69,5	92,8	108,2	99,6	78,3	77,5	78,4	87,8	96,4

Tab. 2 – Measured resist thickness of 120K

With all the requirements considered, the 120 K, 5%, 100 rpm layer has the best uniformity and sufficient thickness for successful lift-off so it was chosen Figure 44, 45.

This layer could not compete in continuity or homogeneity with resist layers prepared with commercial spray-coaters. It was partly due to cleanness conditions during preparation of our layers, but mainly due to inability of Airbrush to create as small droplets as ultrasonic atomizer. The final resolution was incomparable. But, for following experiments, the chosen layer was sufficient.

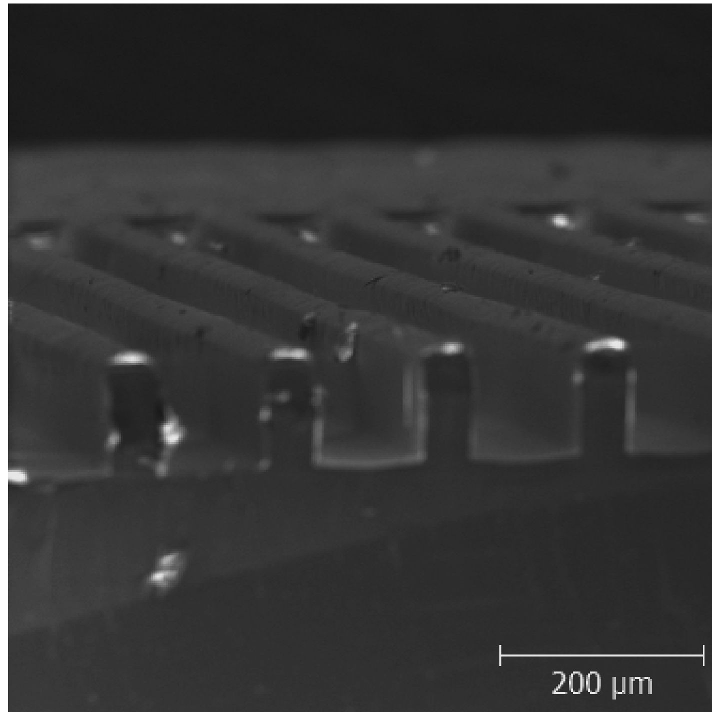

Fig. 44 – Resist layer PMMA 120 K 5%, anisole, 100 rpm

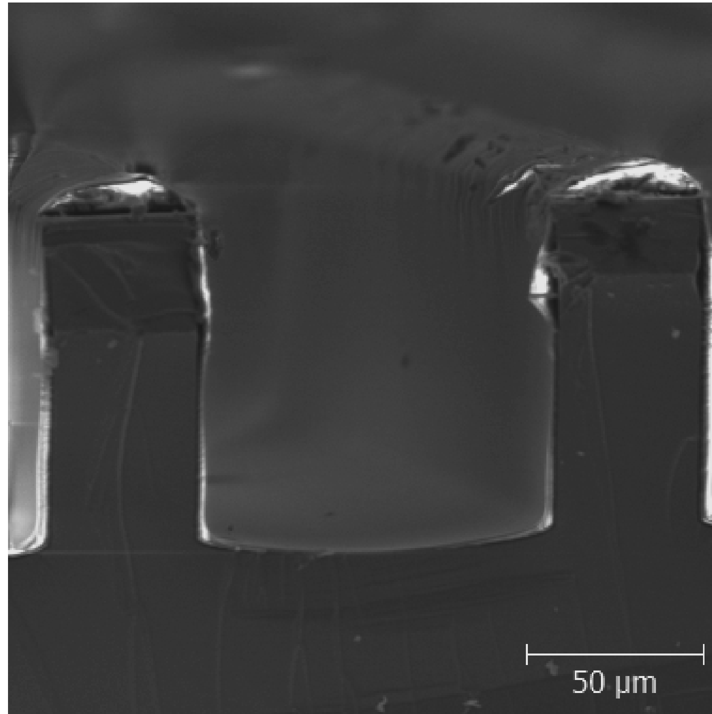

Fig. 45 – Resist layer PMMA 120 K 5%, anisole, 100 rpm

2.2. Test of EBL processes on the plain substrates

Four resists layers were prepared by spray coating of the 120 K, 5%, with 100 rpm on plain substrates 1x1 cm^2. Optimization of dose and developing time was performed on four lines 1 mm long and 10 um wide that were exposed in 2 prepared resist layers by four different doses. Then, two different developing times were applied for the two exposed resist layers. 500, 1000, 2000, 4000, uC/cm^2 were doses used for exposition. Beam size was 61 nm for beam intensity 19. 40 s in IPA:Water (3:1) and 60 s IPA:Water (3:1) were the developing times. The chosen dose was then used for exposition of two resist layers to form masks for 4 gold contacts on every sample. 50 nm thin Au layer was deposited by DC magnetron sputtering in magnetron of type BAL-TEC (MED 020) with argon as a working gas. The pressure was 0.8 Pa and the current was 30 mA. Distance between the target and the sample was 90 mm and deposition rate was 0.25 nm/s. Thickness of Au layer was assumed to be optimal for deposition on clean Si without supporting adhesive layer of Ti or Cr. Lift-off was performed by soaking the samples in warm acetone for 2 hours. Then one of them was put with acetone to ultrasonic washer for 30s and both were dried by nitrogen blow.

Afterwards, the second EBL process had aim to deposit 200nm CN_x/20nmCeO over golden contacts and to test CN_x/CeO_x adhesion on golden contact by performing ultrasound assisted lift-off. Thickness of CN_x/CeO_x was determined by [20]. Deposition parameters of magnetron sputtering of CN_x were: DC magnetron sputtering, current 21mA, pressure 4 Pa (N_2 as a working gas), distance between target-sample is 50 mm, deposition rate was 30nm/min. CeO_x was deposited under these conditions: RF magnetron sputtering, performance was 18 W, pressure 0.4 Pa ($Ar+O_2$) with 1mPa O_2, the distance between target and sample was 90 mm, deposition rate was 0.2 nm/min.

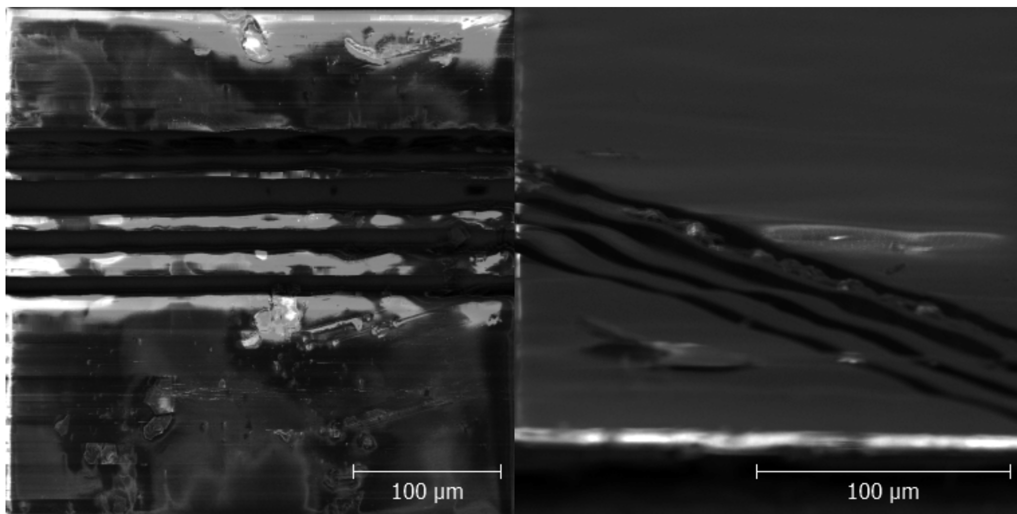

Fig. 46 – Developed lines after 40s of the developing, top view on the left, cross-section view on the right

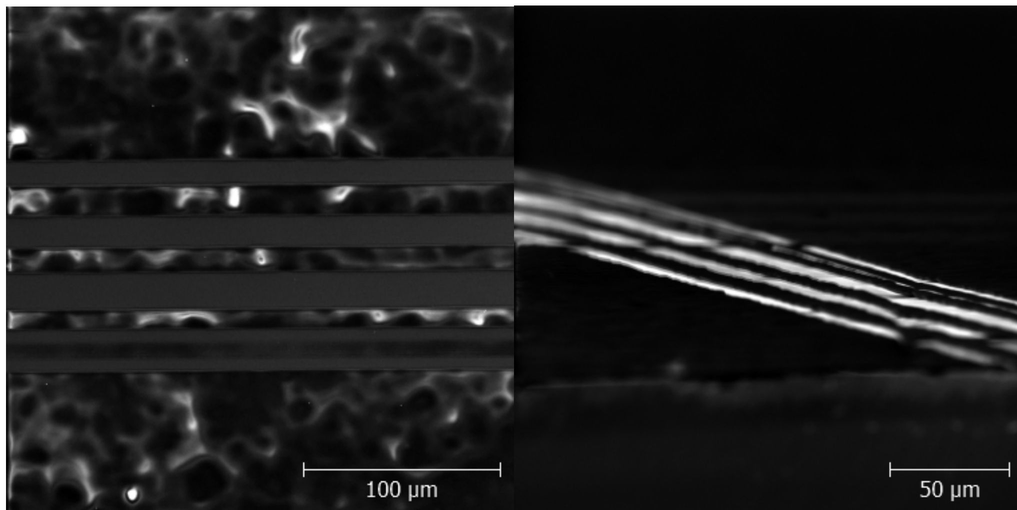

Fig. 47 – Developed lines after 60s of the developing, top view on the left, cross-section view on the right

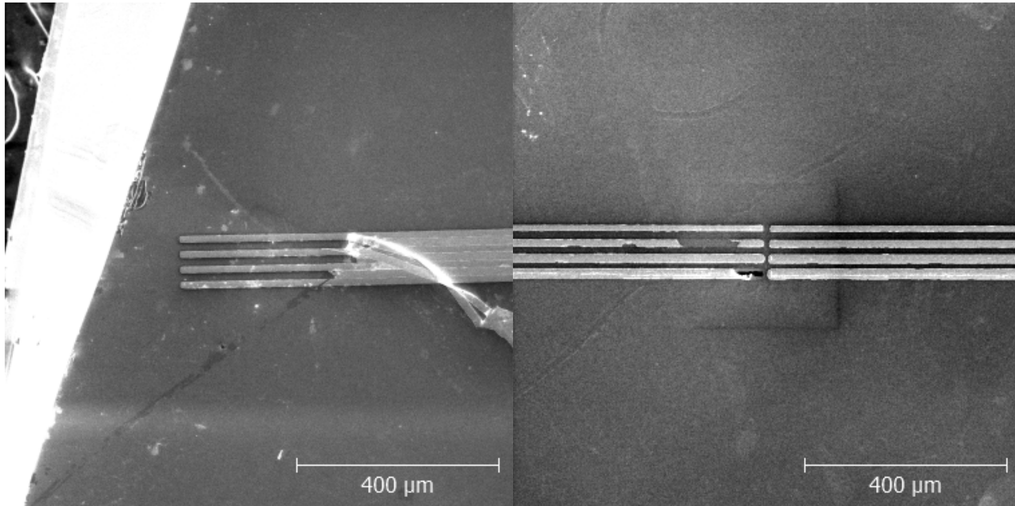

Fig. 48 – Au contacts after lift-off, without ultrasound assisted on the left, with ultrasound assisted on the right

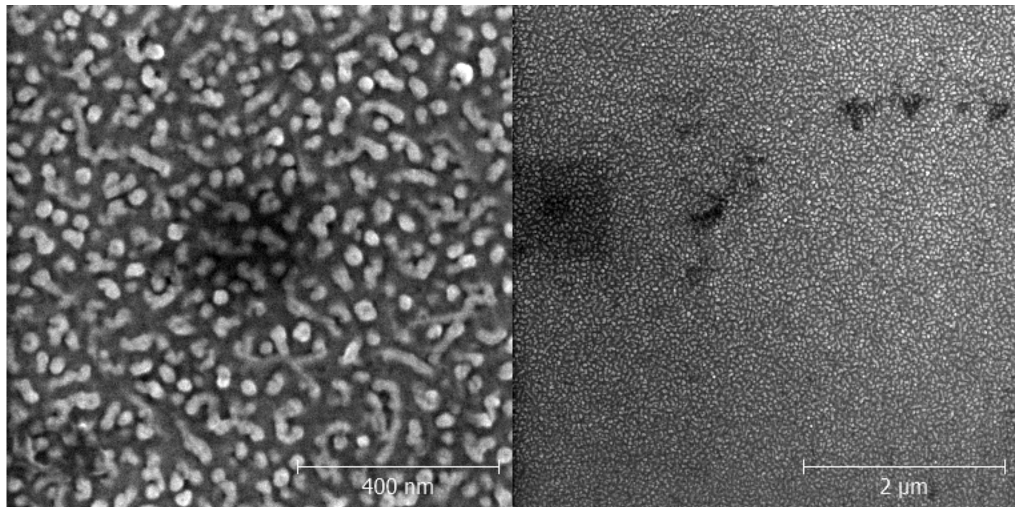

Fig. 49 – CNx/CeO layer on Au contact after ultrasound assisted lift-off

Results show that the suitable dose was 500 uC/cm^2, which matches to the uppermost line in Figure 47. The other lines seem to be overdosed and at 4000 uC/cm^2 the cross-link and negative lithography already took place as can be seen in Fig. 46, 47. The extensive development could be also caused by overheating of the resist due to very high beam intensity. The better developing time was 60s and can be determined by comparison of Figures 46, 47. Lift-off was successful only if the sample was treated with ultrasonic bath, but 30 s proved to be more than adhesive forces of Au on Si could take so time of ultrasonic bath should have been shorter. And finally, the CN_x/CeO on Au layer does not seem to be damaged by final step of the second EBL process, the porous structure after the lift-off is visible in Fig.49 and

it is similar to structures from [20]. And also with adhesion CN_x/CeO on Au layer should not be a problem.

2.3. Additional modifications of parameters for EBL on structured substrate

There were other four samples spray-coated. This time the resist was applied on structured substrates. Goal of this experiment was to modify exposition and developing conditions to achieve fully developed channel with no residual resist in the exposed areas. The exposition doses were same for all the samples. The dose into the channel was 1000 uC/cm^2 and 500 uC/cm^2 was the dose for the contacts on the tops of channels as had been established during testing of EBL on the plain substrates. The first couple of samples were exposed from perpendicular direction and one of the samples was developed by soaking it in developer for 60 s and then drying by nitrogen blow. The other one was soaked in developer for 40 s and then put with developer to ultrasonic washer for 20 s. Drying was performed by nitrogen blow again. The second couple was treated equally during the developing as the first couple in case of applied dosage, but exposition was performed under tilt of -30° and 30°. Results are shown in Figures 50-51.

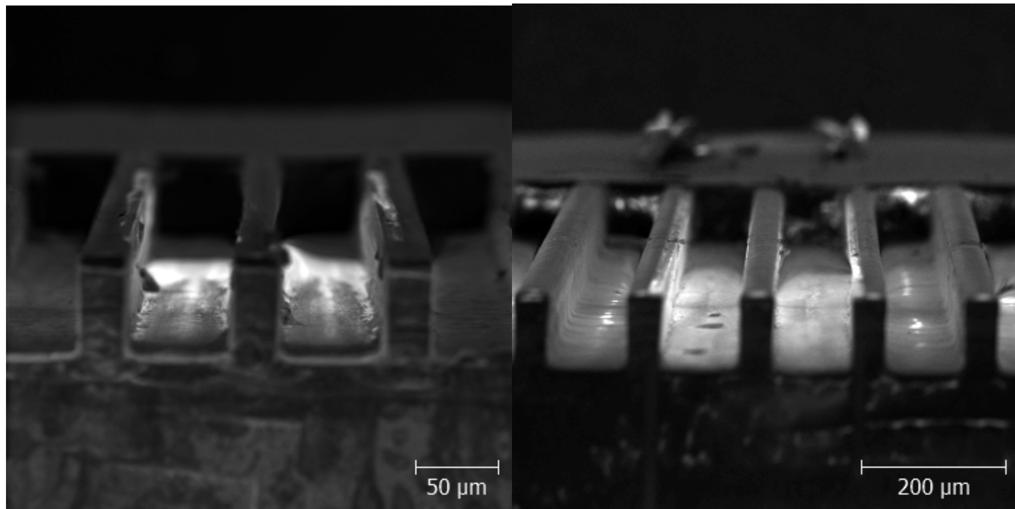

Fig. 50 – Developing of the resist layer without ultrasound assistance, perpendicular exposition on the left, exposition under tilt on the right

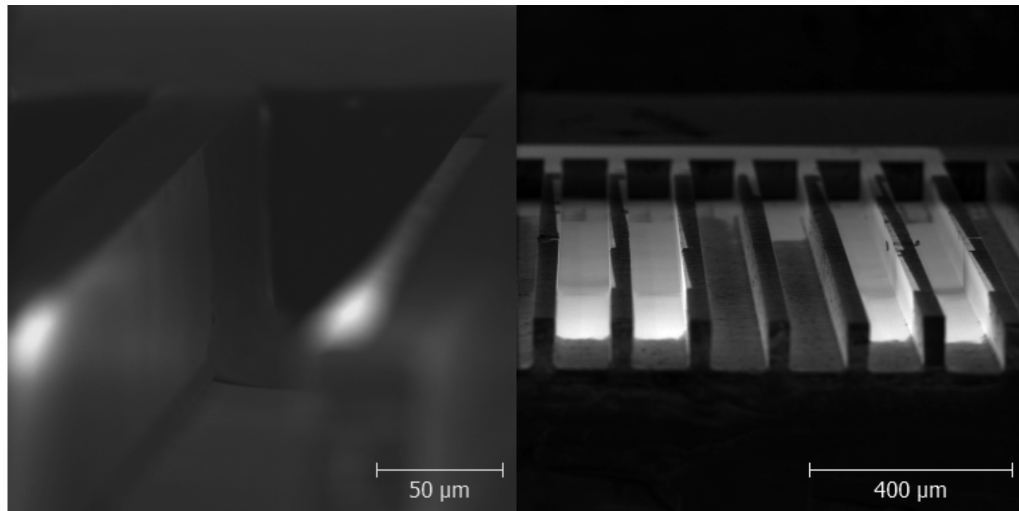

Fig. 51 – Ultrasound assisted developing of the resist layer, perpendicular exposition on the left, exposition under tilt on the right

The results show that the best way to proceed was to perform exposition under tilt to ensure sufficient dose for resist layer at the corners and to assist part of the developing by ultrasound to decrease amount of the residual resist in developed areas to minimum. The high amount of residual resist in developed areas was probably caused by high porosity of structured Si surface caused by its fabrication (Figure). This porosity improves adhesion of resist layer, which in this case, is unfavorable effect.

2.4. Deposition of contacts and catalytic layers into micro-channels

All established parameters and modifications were gathered and applied on three following EBL processes. A purpose of the first EBL process was deposition of golden contacts to the micro channels. The second EBL process ensured the deposition of the catalytic Pt layer into the cathode and finally the third EBL process resulted into a deposited CN_x/ CeO_x layer into anode side. The CN_x and CN_x/ CeO_x were also deposited on clean structured Si wafers as referential samples. The deposition parameters were unchanged.

50 nm thin Au layer and Pt were deposited by DC magnetron sputtering in magnetron of type BAL-TEC (MED 020) with argon as a working gas. Pressure was 0.8, current is 30 mA. Distance between target and sample was 90 mm. Deposition rate of Au was 0.25 nm/s and of Pt was 0.15 nm/s. Deposition parameters of

magnetron sputtering of CN_x were: DC magnetron sputtering, current 21mA, pressure 4 Pa (N2 as a working gas), distance between target-sample was 50 mm, deposition rate was 30nm/min. CeO_x was deposited by RF magnetron sputtering under these conditions: performance was 18 W, pressure 0.4 Pa ($Ar+O_2$) with 1mPa O_2 distance between target-sample was 90 mm, deposition rate was 0.2 nm/min. Every step was captured and the whole process was regularly controlled by EDX.

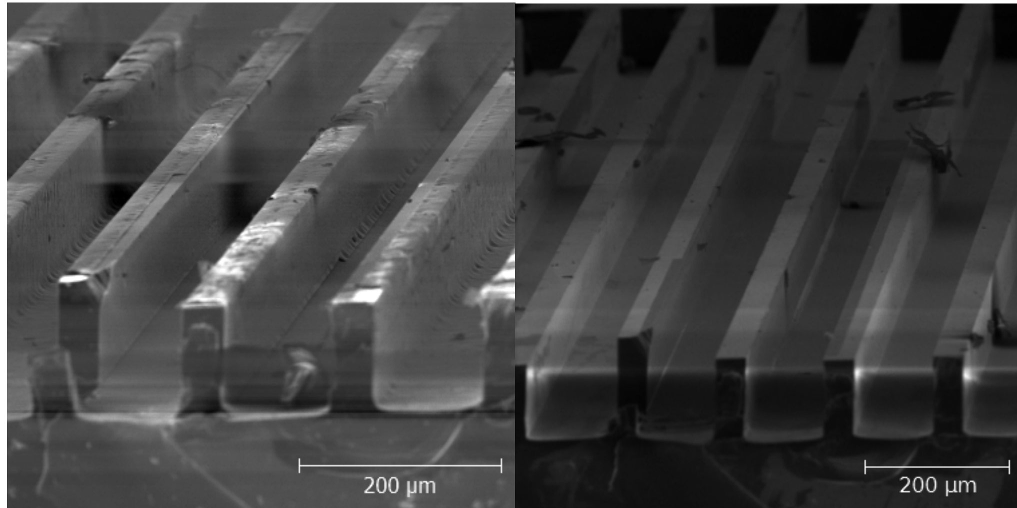

Fig. 52 – Au contacts before lift-off on the left, after lift-off on right

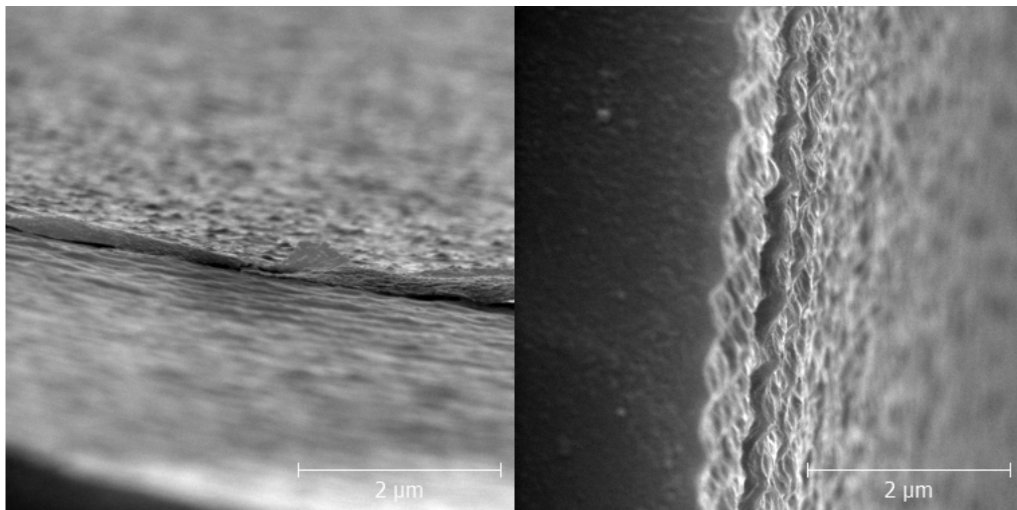

Fig. 53 – Cross-section view on detail of Au layer edge on Si, the bottom on the left, the wall on the right

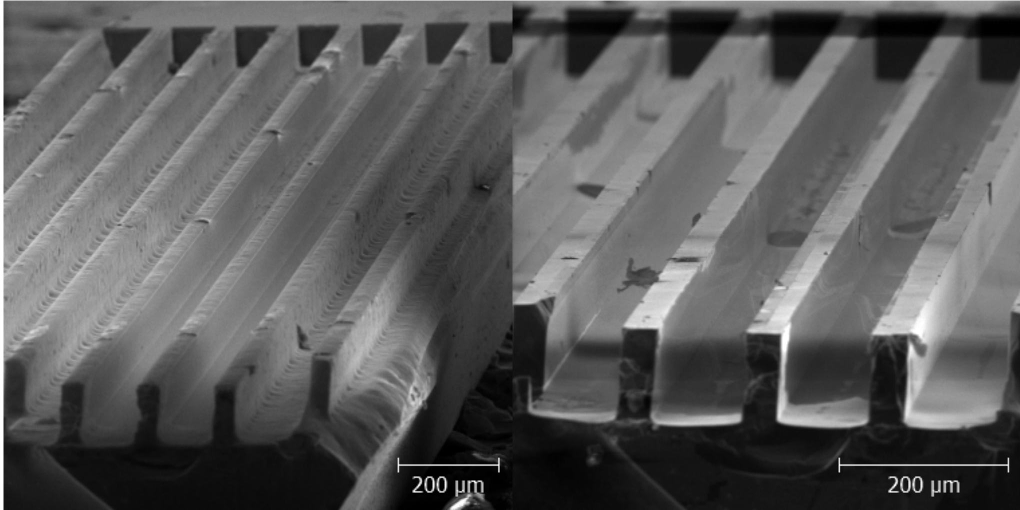

Fig. 54 – Pt layer on Au contact (the second channel from the left) and on Si (the second channel from the right), before lift-off on the left figure, after lift-off on right figure

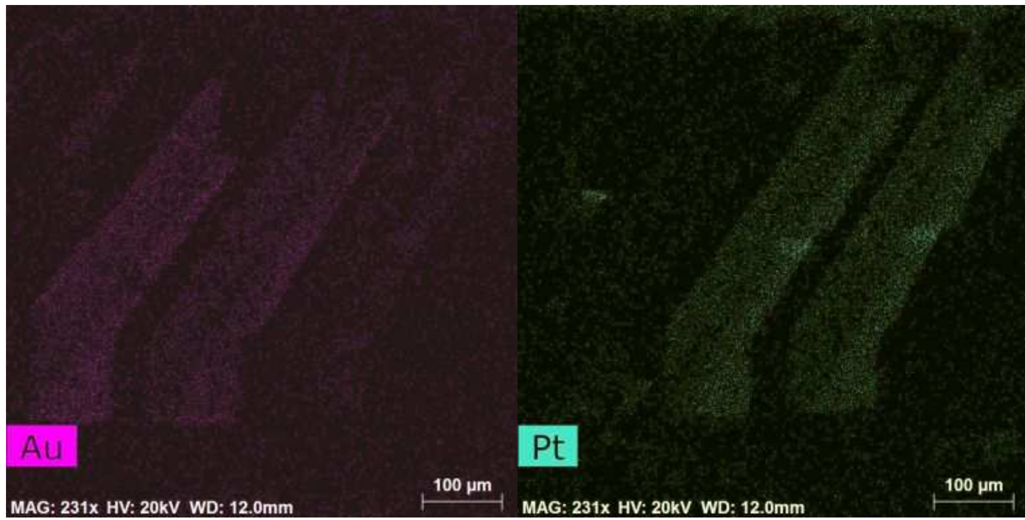

Fig. 55 – EDX – Pt layer on Au contact after lift-off (matches to Fig.54 on the right)

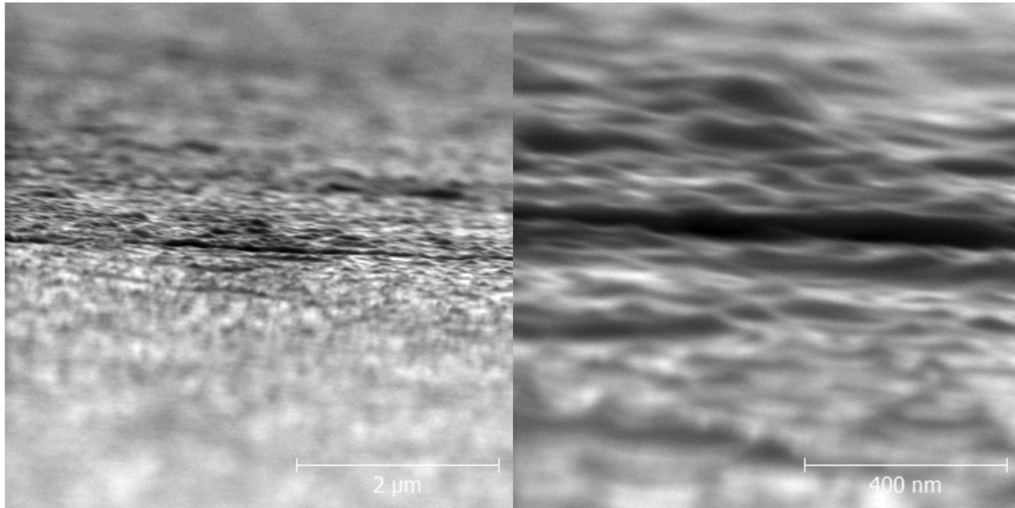

Fig. 56 – Edge of Pt layer on Au contact at the bottom of the micro-channel (cross-section view)

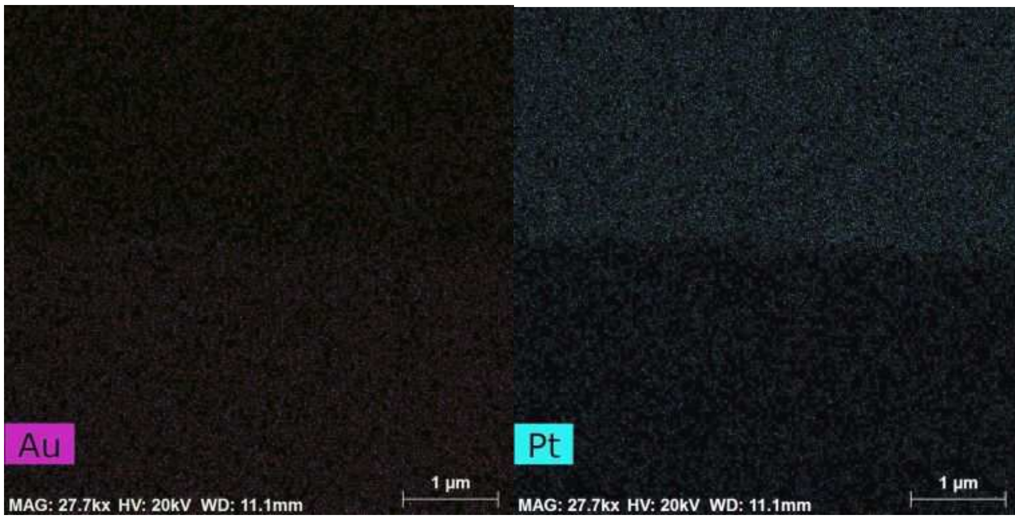

Fig. 57 – EDX – Edge of Pt layer on Au contact (cross-section view, matches Fig. 56 on the left)

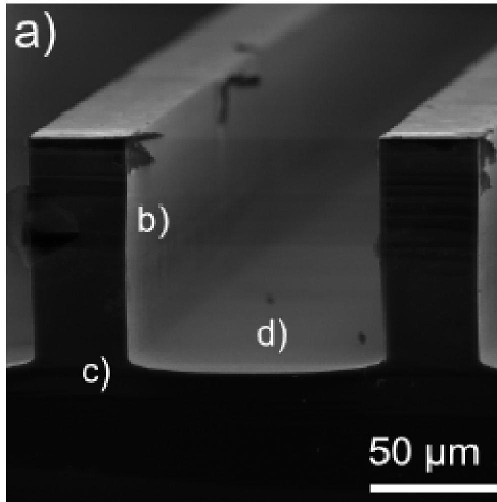

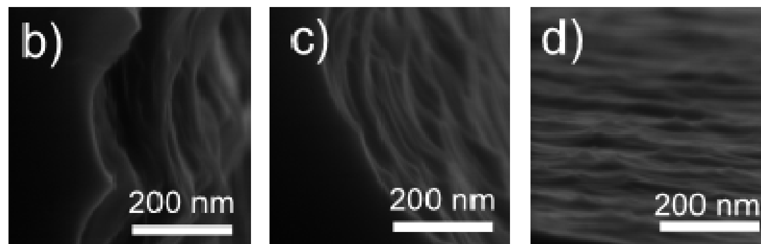

Fig. 58 – Si channel; b), c), d) are details of the Fig. a); b) corner at the bottom; c) wall; d) bottom

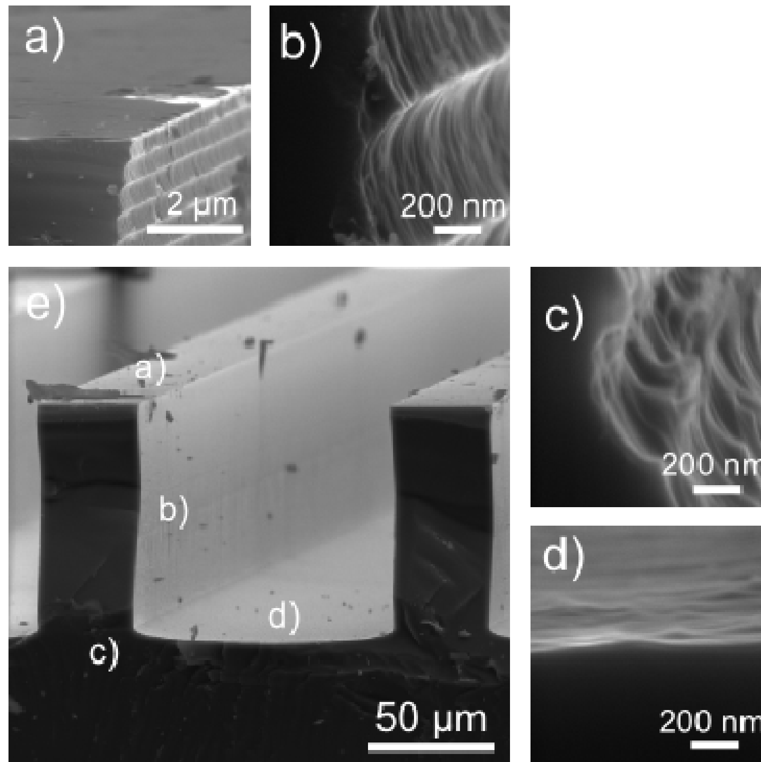

Fig. 59 – Si channel with CNx layer; a) b), c), d) are details of the Fig. e); a) top of the channel b) wall; c) corner at the bottom; d) bottom

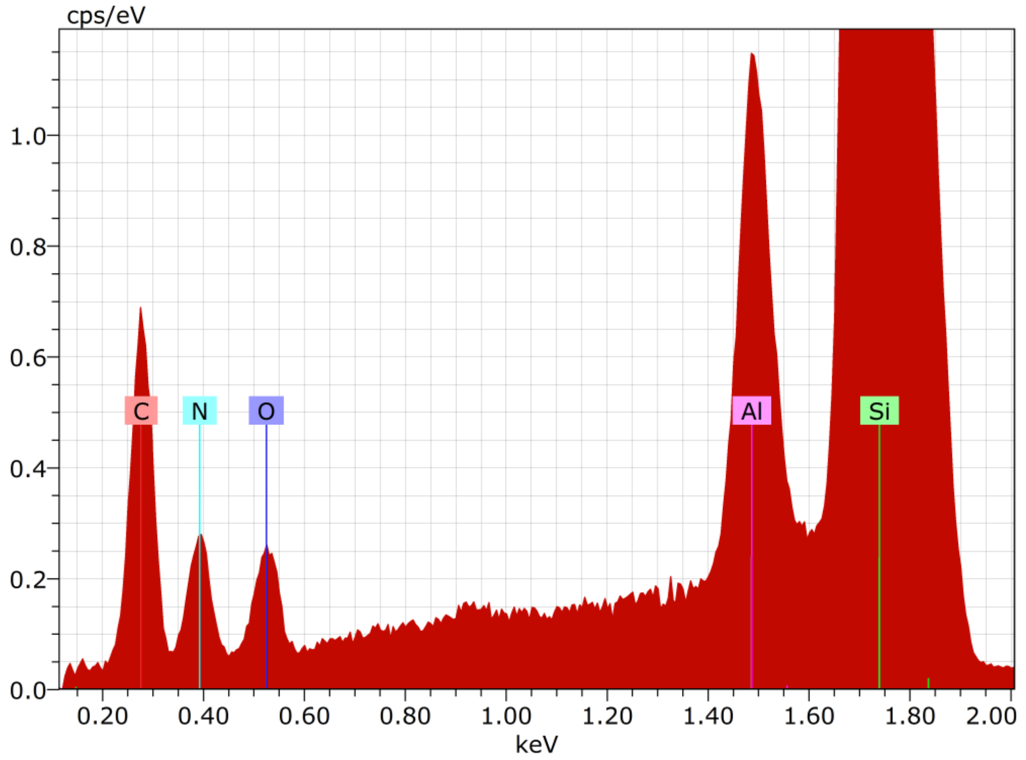

Fig. 60 – EDX of the Si channel with CNx layer

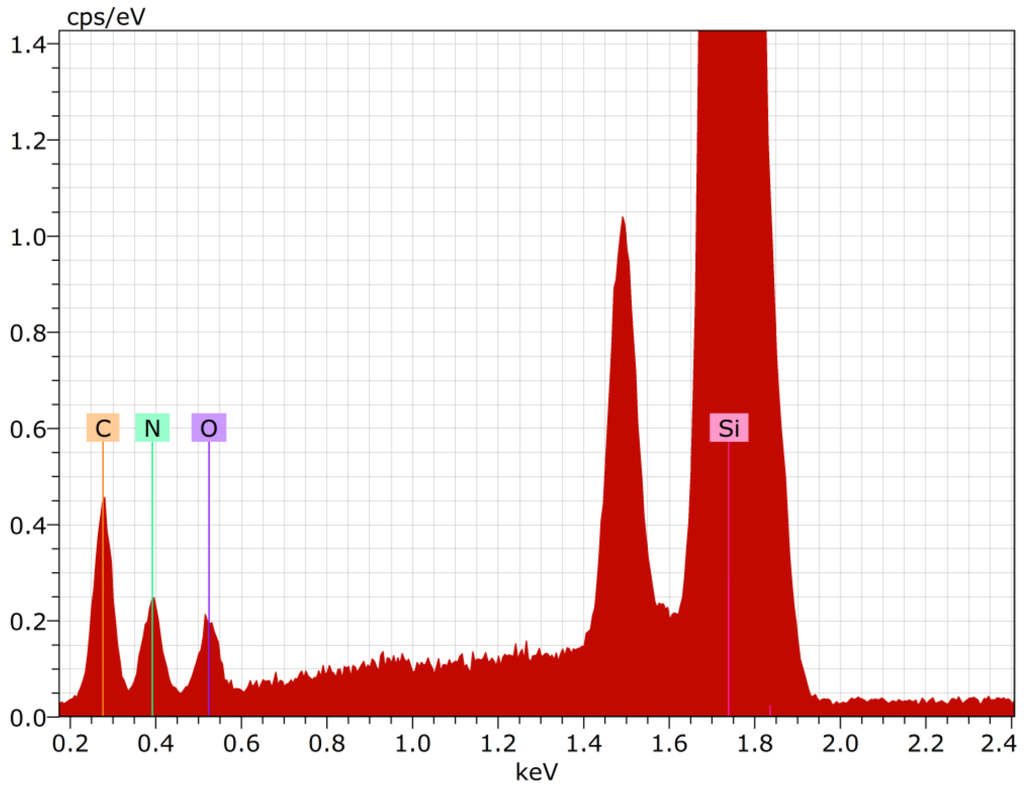

Fig. 61 – EDX of the wall of the Si channel with CNx layer

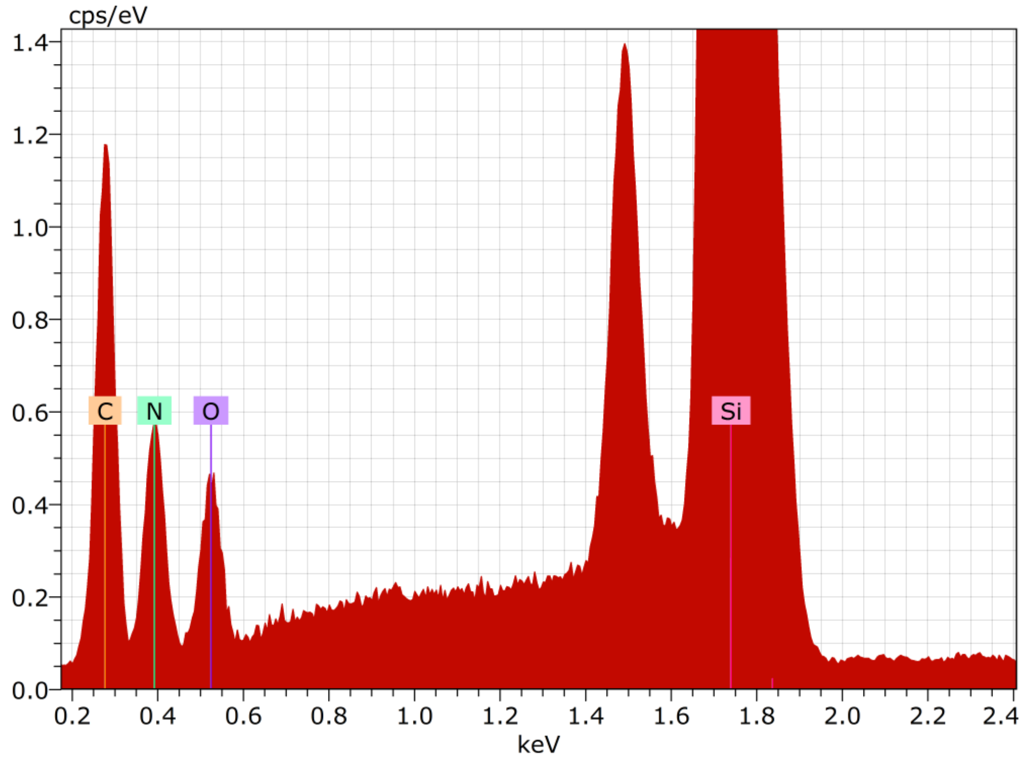

Fig. 62 – EDX of the bottom of the Si channel with CNx layer

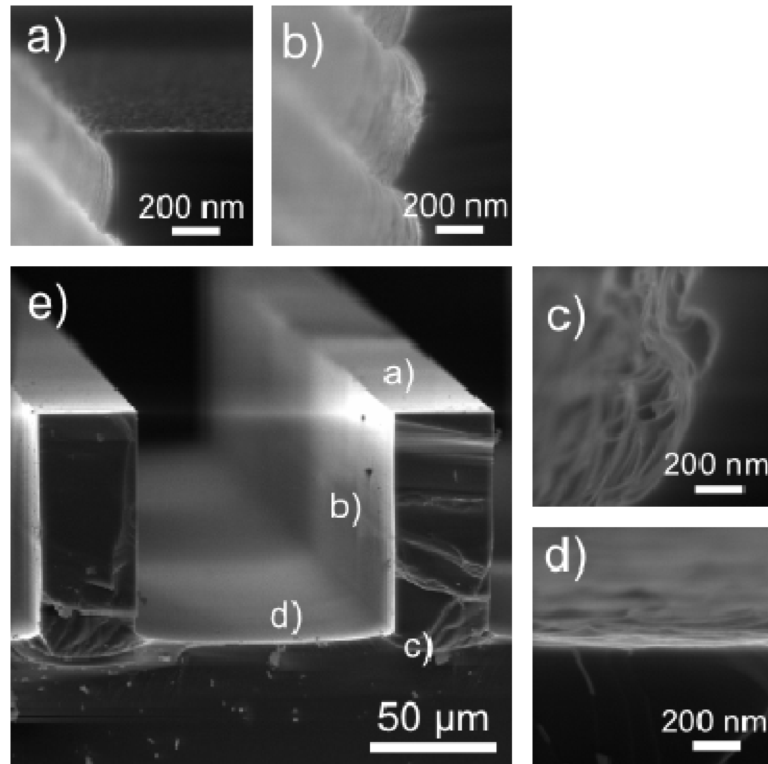

Fig. 63 – Si channel with CNx/ CeO_x layer; a) b), c), d) are details of the Fig. e); a) top of the channel b) wall; c) corner at the bottom; d) bottom

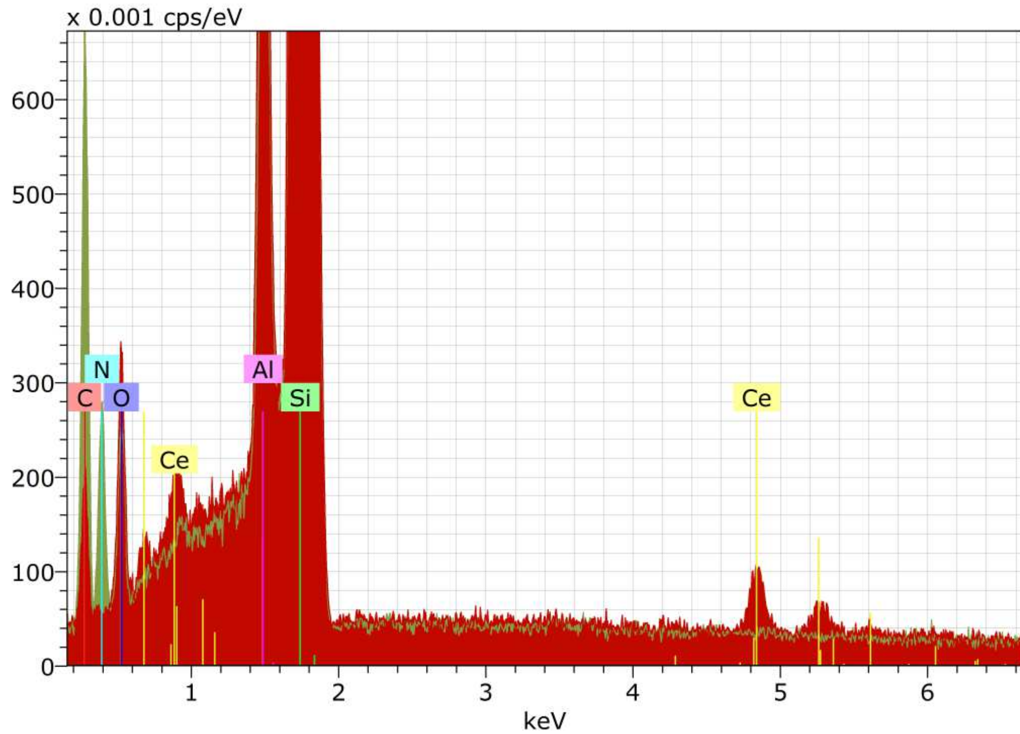

Fig. 64 – EDX of the Si channel with CNx layer (green) and with CNx/ CeO_x Layer (red)

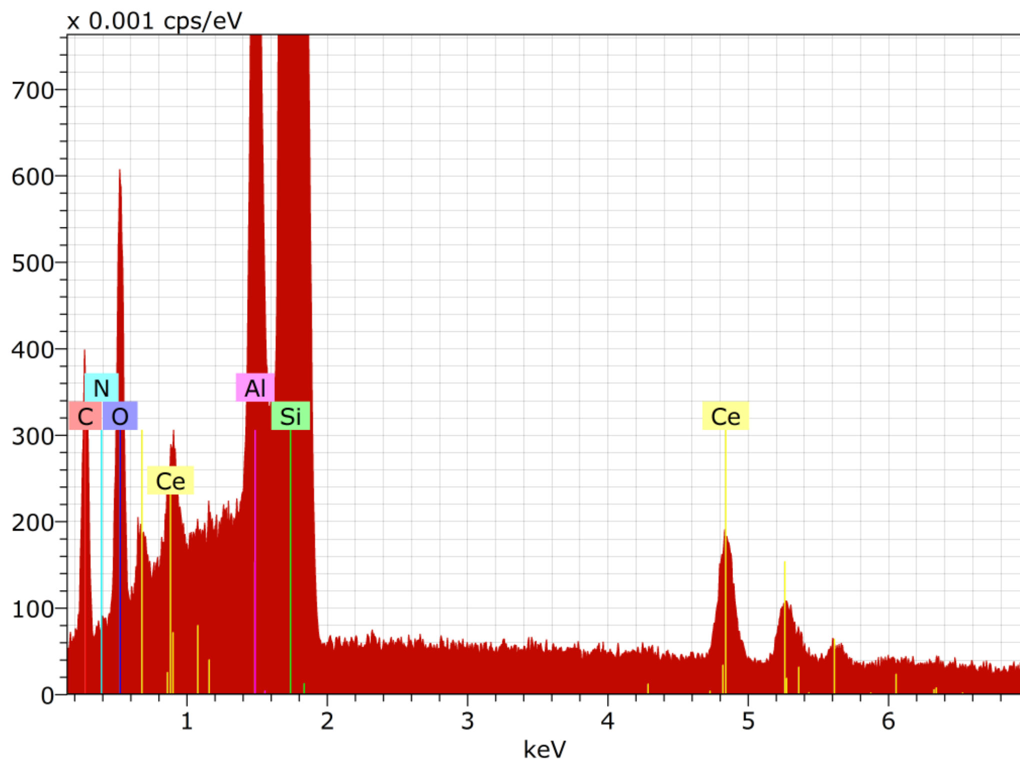

Fig. 65 – EDX of the wall of the Si channel with CNx/ CeO_x layer

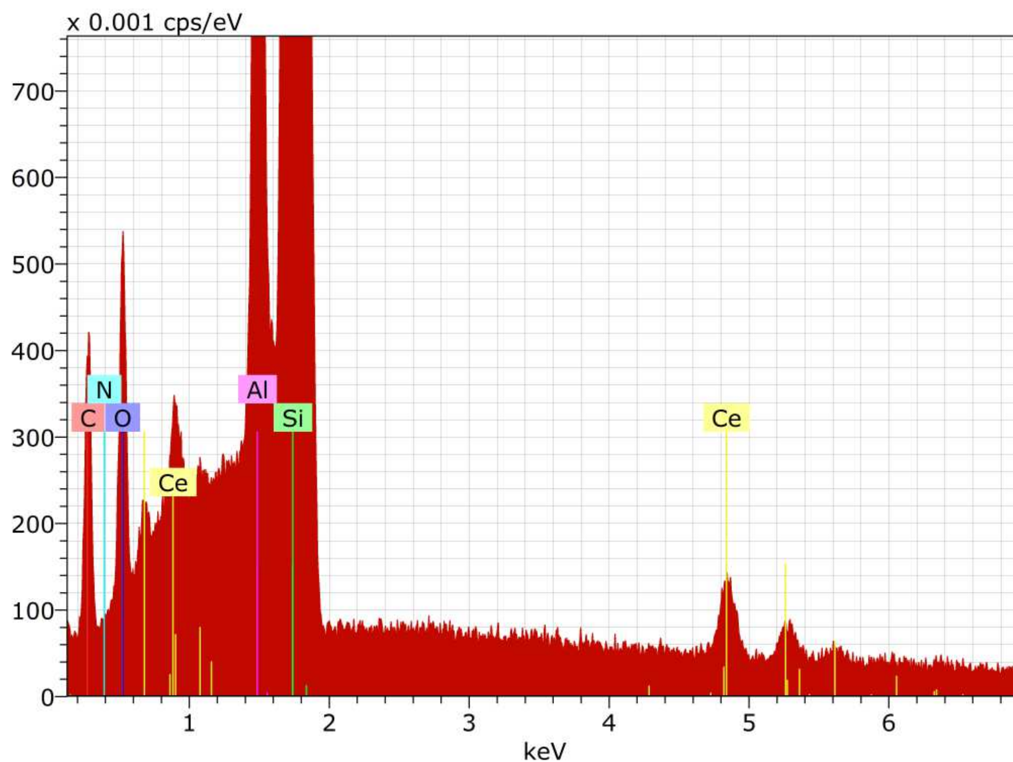

Fig. 66 – EDX of the bottom of the Si channel with CNx/ CeO_x layer

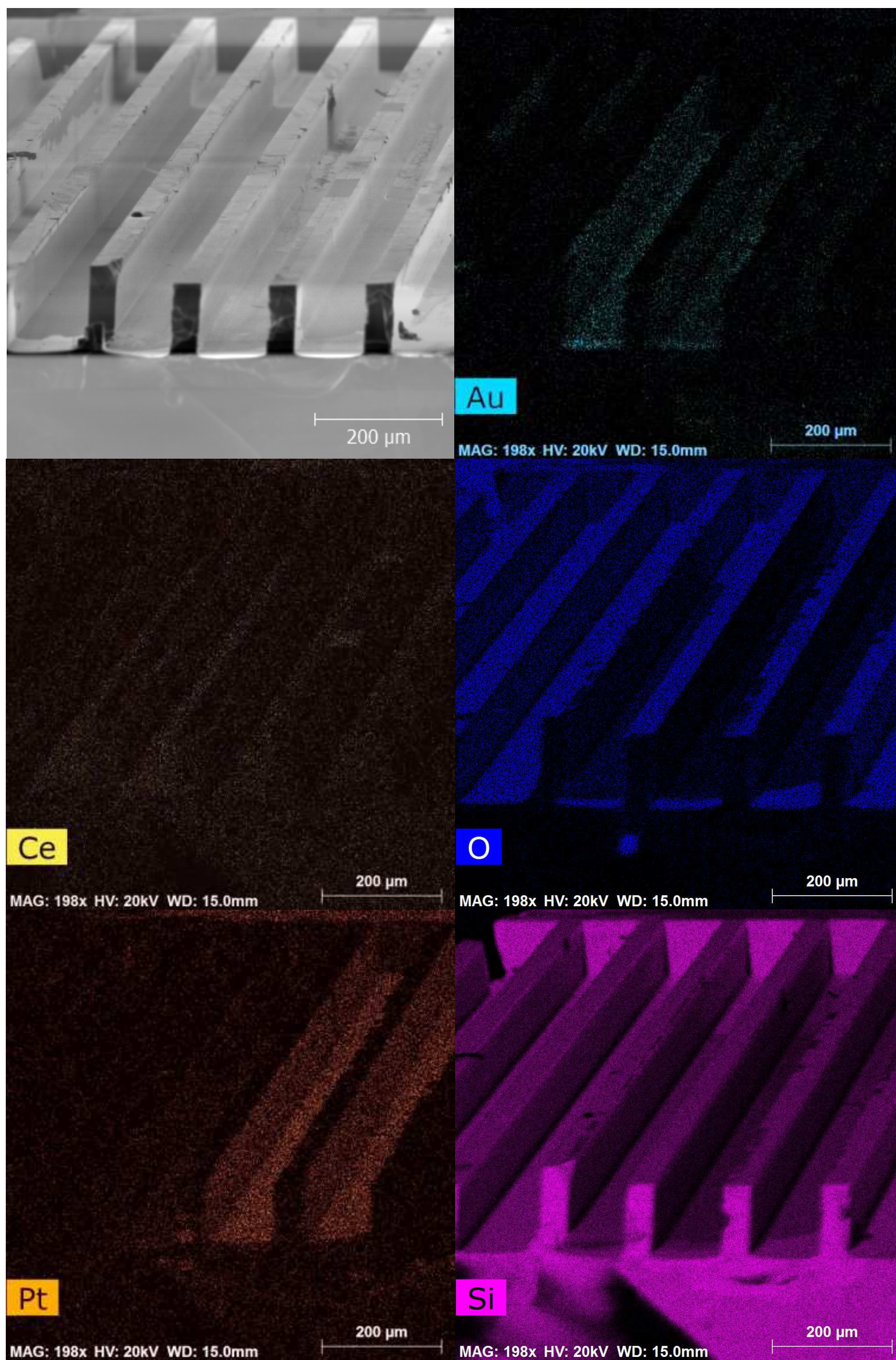

Fig. 67 – EDX of CNx/ CeO_x on Au (the second channel) and Pt on Au (the third channel from the left in) and of CNx/CeO on Si (first from the left) and Pt on Si (first from the right)

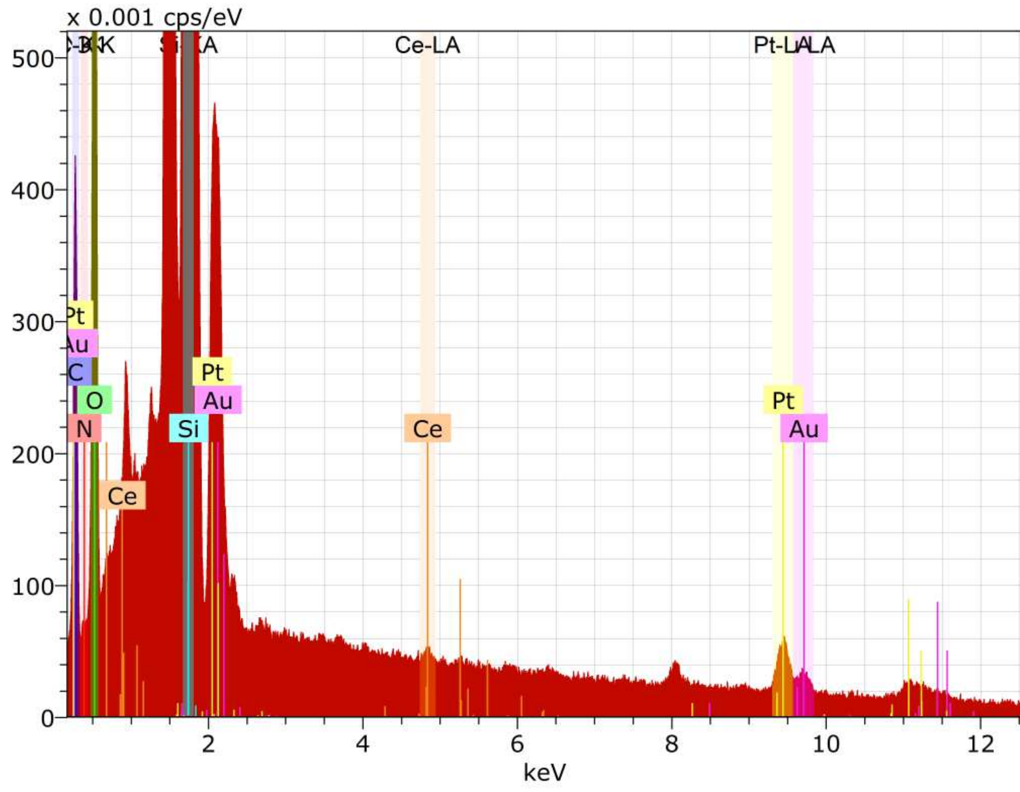

Fig. 68 – EDX of CNx/ CeO_x on Au and Pt on Au

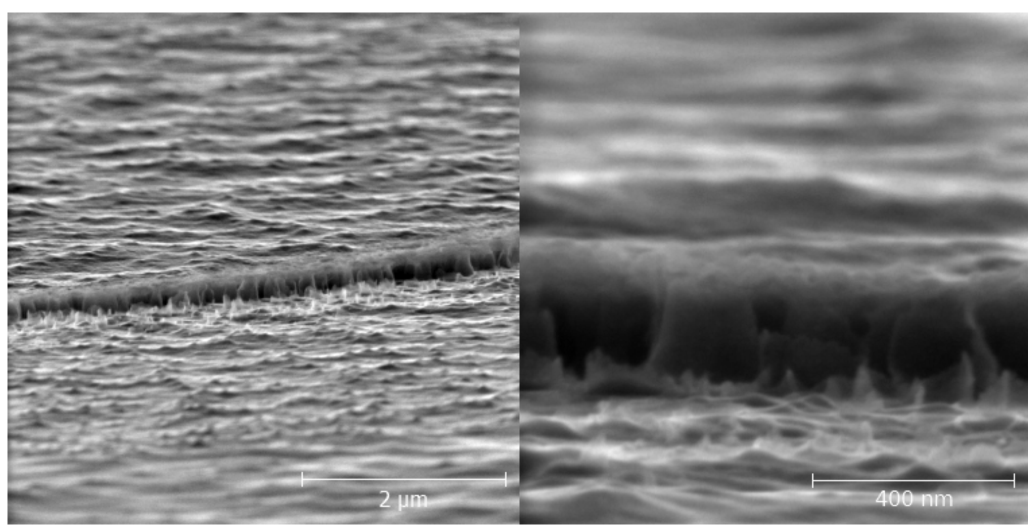

Fig. 69 – Edge of the CNx/ CeO_x layer on Au contact on the bottom of the channel, cross-section view of the channel

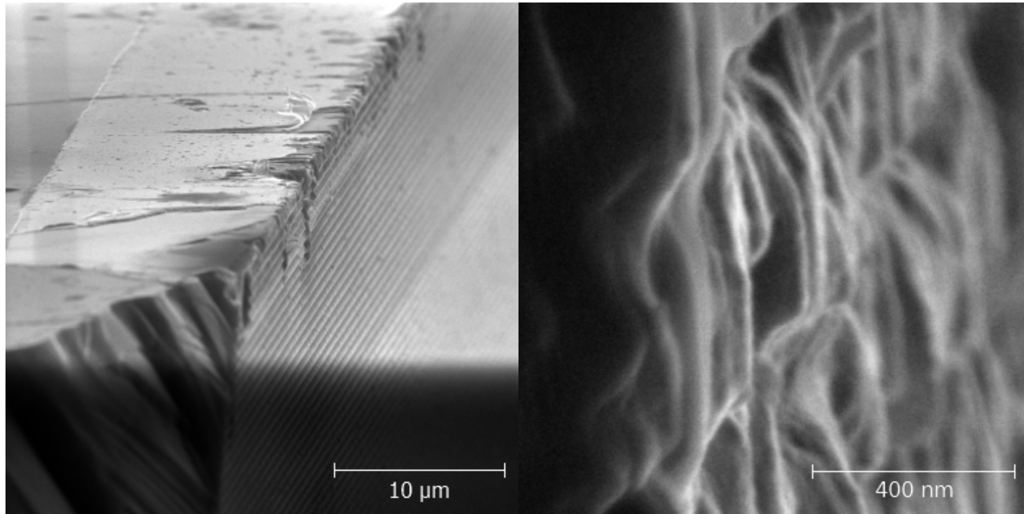

Fig. 70 – CNx/ CeO_x layer on Au contact on the wall of the channel, cross-section view of the channel

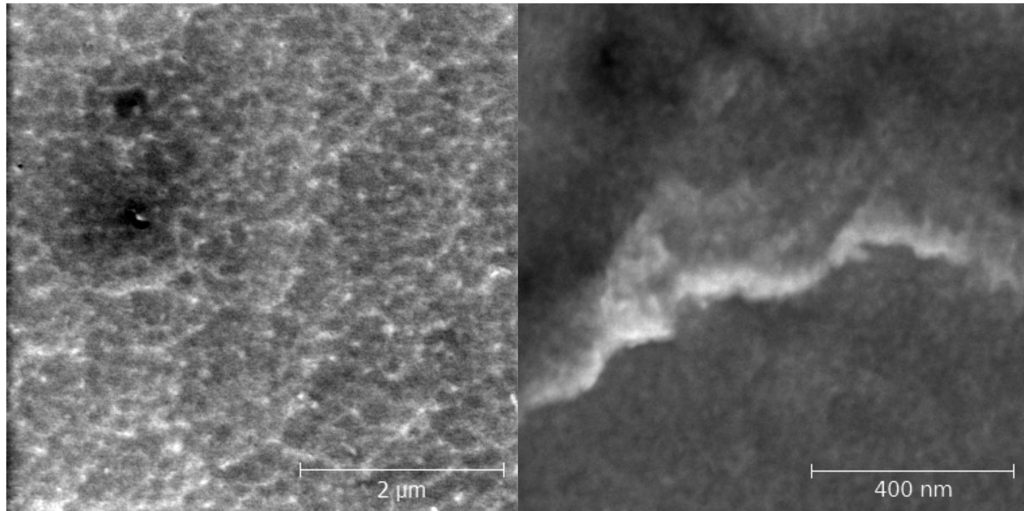

Fig. 71 – CNx/ CeO_x on Au (bottom), top-view

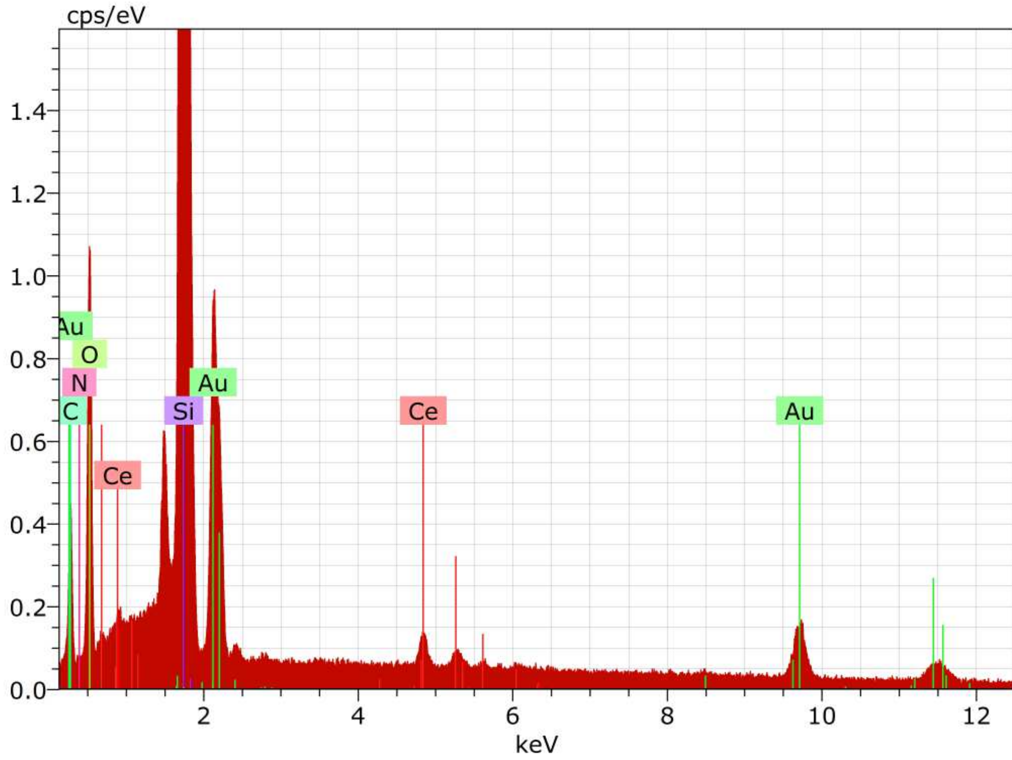

Fig. 72 – EDX of CeO_x on the wall with Au contact underneath

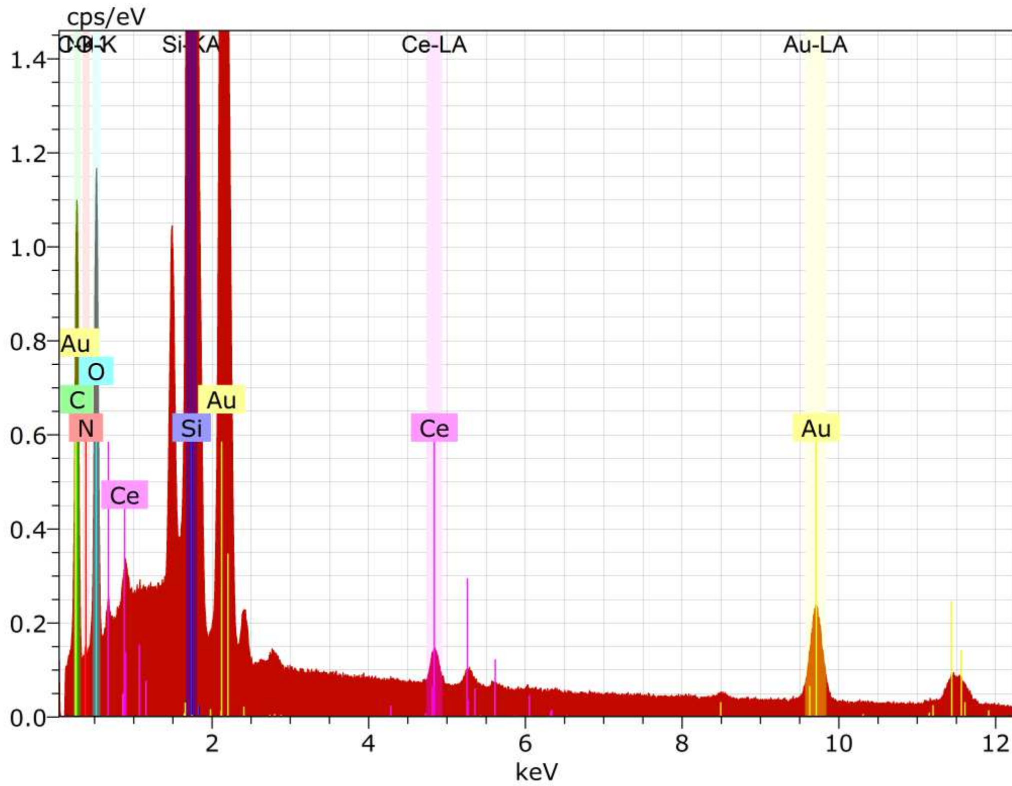

Fig. 73 – EDX of CeO_x on the bottom with Au contact underneath

Au contacts were successfully deposited to the channels (see Figures 52, 53). There can be observed some flaws in the contact. In the corner of the bottom in right channel was discontinuity caused by lift-off of residual resist. The second flaw is missing contact on the left top of the left channel. The reason was probably misplaced matrix during exposition.

Pt layer was deposited perfectly due to completely successful EBL process, (see Figures 54, 56). The presence of Pt layer and Au contacts was verified by EDX in Figures 55, 57.

During examination of CN_x/ CeO_x on clean structured Si, observable deposited layer was only on tops of the channel (comparison of Figures 59 and 59). But EDX confirms presence of the CN_x (Figures 60 - 62). It was found out that etching of CN_x layer during deposition of CeO in oxygen plasma was effective only on the tops of the channels (Figure 63) and higher parts of the walls. The lower parts seemed to be intact (Figure 63). EDX confirmed presence of CeO_x in the whole channel (Figure 64 - 66).

The third EBL process was successfully finished (Figures 67, 69 - 71) and presence of all deposited layers was confirmed by EDX (Figure 67, 68). Morphology of the CN_x/ CeO_x was the same as in case of clean Si and layer on the bottom (Figure 66) did not seem to be even similar to layers from [20]. Layer of CN_x, seems to be still about 200 nm thick but in case of successful etching, the layer thickness should be significantly reduced. A presence of CeO_x on the wall of the channel and on its bottom was also confirmed by EDX (Figures 72, 73).

The observation of final result indicates that Au contacts on the tops of channels are disintegrated, which is probably consequence of worse adhesion on smooth Si surface than on structured Si in channels. Improvement could be achieved by application of adhesive layer (Ti, Cr, etc.).

It is assumed that already deposited catalytic layer is not chemically or physically influenced by next EBL process. It would not have been completely true in case of Pt layer during hot plate after next resists layer spray coating and during resist lift-off. The catalytic properties of Pt layer would not have been completely preserved.

Information gathered from EDX spectroscopy could be affected by shadowing effect. The mutual position of the detector and the sample with high topography could be so inappropriate that emitted X-ray is not capable to reach the detector

through the structure. Despite the maximum effort to right advantageous positioning of the sample, the shadowing effect cannot be completely excluded.

2.5. Another approach to micro-channel fabrication

Some effort was given to try another approach of micro-channels fabrication via FIBL (Fig.).

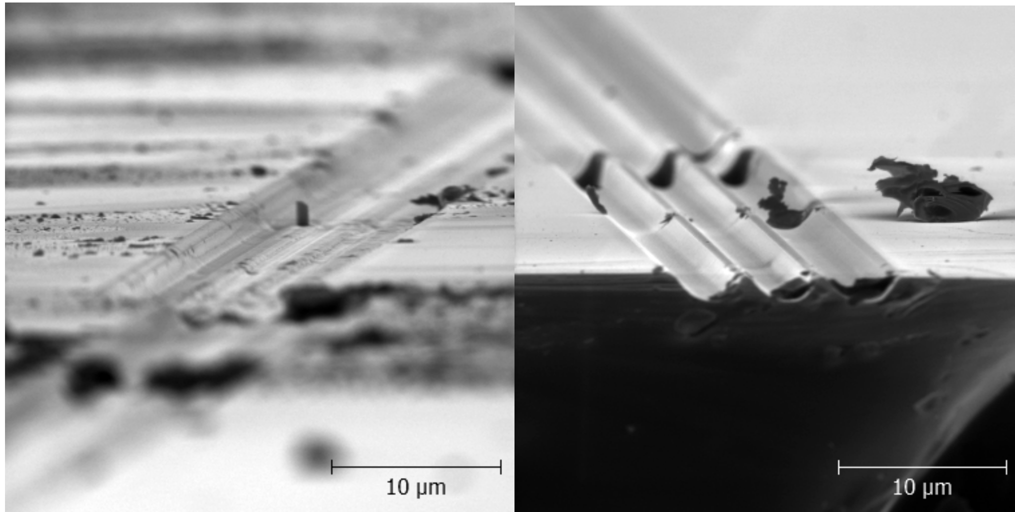

Fig. – Etched channels to Si substrate with FIB; distance between channels 1μm on the left and μm on the right

It was found that for fabrication of 2 μm deep and 2 μm wide separated channels it is necessary to set distance between channels on 2 μm also. It was also observed that in case of channels longer then maximum width of view field the channels are difficult to connect due to drift of the FIB system. However the main disadvantage is extreme time severity in case of fabrication of larger figures in order of tens of μm, which are for planar micro fuel cell required.

3. Conclusion

The main aim of this diploma thesis was modification of every step of the EBL process for 3D Si surface to enable a deposition of active layers to micro-channels of monolithic planar micro fuel cell. This process has been modified and successfully optimezed for 3D Si surface and deposition of active layers was performed.

Optimization of spray coating with spray coating system of our own design was successfully performed. The 120 K 5% resist layer coated at 100 rpm was chosen as the most suitable layer that satisfies the requirements for further experiments.

The initial EBL parameters were established during the EBL testing on the plain surface of Si. With further modifications for 3D surface, these parameters were used for successful EBL process.

The parameters are: exposition dose 500 μC/cm2 for contacts on top of channels and 1000 μc/cm2 for contacts in channels, tilt of the sample 30 degrees and -30 degrees, beam intensity 19, 30 keV, development in IPA:water for 40 s + 20 s ultrasound assisted, lift-off in warm acetone for 2 hours + 20 s ultrasound assisted.

EBL processes with Pt and Au layers were successfully finished. The deposition of CN_x/CeO layer on high topography will probably be the object of further research, testing and optimization.

4. Bibliography

[1] Hoogers, G., 2002. Fuel cell technology handbook,

[2] EG&G Technical Services, I., 2004. Fuel Cell Handbook. Fuel Cell, 7 Edition(November), pp.1–352.

[3] Ahn, S.J. et al., 2006. Co-planar type single chamber solid oxide fuel cell with micro-patterned electrodes. Journal of Electroceramics, 17(2-4), pp.689–693.

[4] Hasran, U.A. et al., 2011. A simple thermal oxidation technique and KOH wet etching process for fuel cell flow field fabrication. International Journal of Hydrogen Energy, 36(8), pp.5136–5142.

[5] Lee, S. ., Chang-Chien, A., Cha, S. ., O'Hayre, R., Park, Y. ., Saito, Y., & Prinz, F. . (2002). Design and fabrication of a micro fuel cell array with "flip-flop" interconnection. Journal of Power Sources, 112(2), 410–418.

[6] Lu, G. Q., Wang, C. Y., Yen, T. J., & Zhang, X. (2004). Development and characterization of a silicon-based micro direct methanol fuel cell. Electrochimica Acta, 49(5), 821–828.

[7] Apblett, C., Ingersoll, D., Atanassov, P., Maricle, D., & Sarangapani, S. (2006). Fabrication and testing of a miniature H2/O2 and MeOH/O2 fuel cell. Journal of Power Sources, 162(1), 255–261.

[8] Park, B.Y. & Madou, M.J., 2006. Design, fabrication, and initial testing of a miniature PEM fuel cell with micro-scale pyrolyzed carbon fluidic plates. Journal of Power Sources, 162(1), pp.369–379.

[9] Zhang, Y. et al., 2007. Development of MEMS-based direct methanol fuel cell with high power density using nanoimprint technology. Electrochemistry Communications, 9(6), pp.1365–1368.

[10] Su, H.N., Liao, S.J. & Xu, L.M., 2009. Design, fabrication and preliminary study of a mini power sourcewith a planar six-cell PEM unitised regenerative fuel cell stack. Fuel Cells, 9(5), pp.522–527.

[11] Lu, Y. & Reddy, R.G., 2010. Performance of micro-PEM fuel cells with different flow fields. Journal of Power Sources, 195(2), pp.503–508.

[12] Motokawa, S. et al., 2004. MEMS-based design and fabrication of a new concept micro direct methanol fuel cell (u-DMFC). Electrochemistry Communications, 6(6), pp.562–565.

[13] Ishizuka, M. et al., 2006. Metallization on three dimensions microstructures using photoresist spray coating for microdirect methanol fuel cell. Japanese Journal of Applied Physics, Part 1: Regular Papers and Short Notes and Review Papers, 45(10 A), pp.7944–7948.

[14] Cohen, J.L. et al., 2005. Fabrication and preliminary testing of a planar membraneless microchannel fuel cell. Journal of Power Sources, 139(1-2), pp.96–105.

[15] Choban, E.R. et al., 2005. Membraneless laminar flow-based micro fuel cells operating in alkaline, acidic, and acidic/alkaline media. Electrochimica Acta, 50(27), pp.5390–5398.)

[16] Phirani, J. & Basu, S., 2008. Analyses of fuel utilization in microfluidic fuel cell. Journal of Power Sources, 175(1), pp.261–265.

[17] XIAO, Z. et al., 2008. Monolithically integrated planar microfuel cell arrays. Sensors and Actuators B: Chemical, 132(2), pp.576–586.

[18] Chen, F., Chang, M.H. & Lin, H.Y., 2008. Analysis of a novel MEMS-based design of micro-direct methanol fuel cell. Journal of Power Sources, 178(1),

pp.125–131.
[19] Khalakhan, I. et al., 2013. Growth of nano-porous Pt-doped cerium oxide thin films on glassy carbon substrate. Ceramics International, 39(4), pp.3765–3769.
[20] Dubau, M. et al., 2014. Preparation of magnetron sputtered thin cerium oxide films with a large surface on silicon substrates using carbonaceous interlayers. ACS Applied Materials and Interfaces, 6(2), pp.1213–1218.
[21] Owen, G. Electron lithography for the fabrication of microelectronic devices. Rep. Prog. Phys., 1985, vol. 48, p. 795-851.
[22] Matějka, F. Praktická elektronová litografie, ÚPT AV ČR, v.v.i. (2012), ISBN 978-80-87441-04-6
Available from <http://www.isibrno.cz/teams/EBL/PraktickaEBL-ED.pdf>
[23] McCord, M.A; Rokos, M.J. *Handbook of Microlithography, Micromachining and Microfabrication, Volume 1: Microlithography* [online]; last revision 2014-04-11; [cit. 28. 7. 2014].
Available from < http://www.cnf.cornell.edu/cnf_spietoc.html>
[24] Reichmanis, E.; Novembre, A.E. Lithographic resist materials chemistry. *Annu. Rev. Mater. Sci.,* 1993, vol. 23, p. 11-43
[25] Hall, B.; et al. Spin coating of thin and ultrathin polymer films. *Polymer. Eng. Sci.*, 1998, vol.38,n. 12, 2039-2045
[26] Weil, A.; Francou, J.M..; Dechenaux, E. Photoresist spin coating mechanism related to polymer solution rheology. *Microelectron. Eng.*, 1987, vol.6, p. 427-43
[27] Lawrence, C.J. The mechanics of spin coating of polymer films. *Physics of Fluids* Oct88, Vol. 31 Issue 10, pp. 2786-2795
[28] MicroChem Corp.; NANO PMMA and Copolymer [online]. c2001, last revision 2014-07-10 [cit. 2014-07-28].
[29] Pham, N.P. et al., 2008. Photoresist coating and patterning for through-silicon via technology. Journal of Micromechanics and Microengineering, 18, p.125008.
[30] Linden, J. et al., 2011. Spray coating of PMMA for pattern transfer via electron beam lithography on surfaces with high topography. Microelectronic Engineering, 88(8), pp.2030–2032.
[31] Van de Kraats, A.; Murali, R. Proximity Effect in E-beam Lithography [online]. c2005; poslední revise 2005-05-24 [cit. 2014-07-15]. Available from <http://nanolithography.gatech.edu/proximity.htm>
[32] Groves, T.R. Theory of beam-induced substrate heating. *J. Vac. Sci. Technol. B*, 1996, vol. 14, no. 6, p. 3083-3844
[33] Tescan; Proximity Effect in Elektron Beam Lithography; c2012 [cit. 2014-07-25]; Available from <http://www.tescan.com/cz/aplikace/technologie/proximity-efekt-v-elektronove-litografii>
[34] Bhushan, B. Springer Handbook of Nanotechnology. Springer, 2007. 1916 p. ISBN 978-3-540-29855-7. Part A, Chapter 7.1, Basic Microfabrication Techniques, p. 199-205
[35] Haviar, S., 2010. Elektronová litografie v řádkovacím elektronovém mikroskopu. , p.82.
[36] MicroChem Corp. dokumentace (PMMA Rezist) [online], last revision 2016-03-06, [cit. 2016-07-28].
Available from <http://www.microchem.com/Prod-PMMA.htm>
[37] Hartney, M.A.; Hess, D. W.; Soane, D. S. Oxygen plasma etching for resist, stripping and multilayer lithography. *J. Vac. Sci. Technol. B*, 1998, vol..7. no. 1., p. 1-13.
[38] Reichmanis, E. Thompson, L. F. Polymer materials for Microlithography. *Ann.*

Rev. Mater. Sci., 1
[39] Egerton R. F., Physical Principles of Electron Microscopy: An Introduction to TEM, SEM, and AEM. Springer, 2007. 196 p. ISBN 978-0387-25800-0.
[40] How Microscopes Work, Picture on: <http://isbbio1.pbworks.com/w/page/9205983/Group%205>
[41] Howland, R.; Benatar, L. A Practical Guide to Scanning Probe Microscopy, (2000) ThermoMicroscopes, c1993-2000
[42] Manuál k SPM technikám, Veeco. [online]. c2014, [cit. 2014-07-28]. Available from www.veeco.com/pdfs/library/SPM_Guide _0829 _05 _166.pdf
[43] Giannuzzi, L.A. & Stevie, F.A., 2005. Introduction to focused ion beams: Instrumentation, theory, techniques and practice. *Introduction to Focused Ion Beams: Instrumentation, Theory, Techniques and Practice*, pp.1–357.
[44] Yao, N., 2007. *Focused ion beam systems: basics and applications*, Available at: http://www.lavoisier.fr/livre/notice.asp?id=OA3WRSA2R66OWM.